Preparation and Characterization of Plasma Electrolytically Oxidized Titanium and its Application in Oxygen Sensing

Inaugural-Dissertation

zur Erlangung des Doktorgrades
der Mathematisch-Naturwissenschaftlichen Fakultät
der Heinrich-Heine-Universität Düsseldorf

vorgelegt von

Bernd Engelkamp
aus Borken (Westfalen)

Düsseldorf, Juni 2021

aus dem Institut für Experimentelle Physik der kondensierten Materie
der Heinrich-Heine-Universität Düsseldorf

Gedruckt mit der Genehmigung der
Mathematisch-Naturwissenschaftlichen Fakultät der
Heinrich-Heine-Universität Düsseldorf

Berichterstatter

1. Prof. Dr. Klaus Dieter Schierbaum

2. Prof. Dr. Mathias Getzlaff

Tag der mündlichen Prüfung: 28. Juli 2021

Preface

This thesis is the result of my work in the department of Materials Science (Prof. Dr. K. Schierbaum) at the Institute of Experimental Condensed Matter Physics. It essentially consists of three **peer-reviewed papers**:

- P.I: B. Engelkamp, M. El Achhab, B. Fischer, Ü. Kökcam-Demir and K. Schierbaum, *Combined Galvanostatic and Potentiostatic Plasma Electrolytic Oxidation of Titanium in Different Concentrations of* H_2SO_4, Metals **2018**, 8(6), 386. doi:10.3390/met8060386
- P.II: B. Engelkamp, B. Fischer, and K. Schierbaum, *Plasma Electrolytic Oxidation of Titanium in* H_2SO_4*-*H_3PO_4 *Mixtures*, Coatings **2020**, 10(2), 116. doi:10.3390/coatings10020116
- P.III: B. Engelkamp, and K. Schierbaum, *Oxygen Sensing of Pt/PEO-*TiO_2 *in Humid Atmospheres at Moderate Temperatures* Sensors **2021**, 21(7), 2558. doi:10.3390/s21072558

Contents

Introduction

The natural oxide layer thickness for titanium (Ti) at room temperature is only about 5 nm [1, 2]. The thickness can be increased by thermal or electrochemical methods. The latter uses anodic potentials to reinforce the oxide formation and increase the thickness of the compact oxide layer up to several 100 nm. Technically, the process is called anodization and is applied in the industrial finishing of several metals. Aluminum, titanium, vanadium, zirconium, niobium, molybdenum, hafnium, tantalum and wolfram form readily stable oxide films at anodic potentials, while other metals can be anodized under specific conditions [3]. Titanium oxide has attracted growing interest for applications in various fields, for instance, aerospace, medicine, oil and automotive industry, military, architecture and jewelry [4]. At latest since a report from Fujishima and Honda about the electrochemical photolysis of water on titanium dioxide surfaces in 1972, anodized titanium is also highly valued for its potential in the energy sector [5]. This broad scope of applications, is due to the versatile customization of the oxide layers by using numerous variations of anodization.

One technique that emerged from anodization is plasma electrolytic oxidation (PEO). It belongs to a branch of electrolytic plasma technologies [6], which all have one thing in common: Characteristic dielectric discharges occur, which induce a plasma with visible light emission. The first description of plasma electrolytic discharges phenomena dates back to 1880 and is assigned to Sluginov [7]. The first technical utilization took already place approximately 110 years ago in the Russian industries of ship building and repairing [8]. Systematic investigation followed by Günterschulze and Betz in the 1930's as an aspect of the development of electrolytic capacitors [9]. But only in the 1960's the practical benefits were exploited by McNeill and Gruss in the USA [10, 11]. In the early 1970's Brown et al. derived a method to form aluminum oxide layers based on electrolytic plasma discharges, which they referred to as Anodic Spark Deposition (ASD) [12]. A few years later, Markov et al. developed a similar method for generating an aluminum oxide layer, which they ultimately called Micro-Arc Oxidation (MAO) [13]. Important work followed in the 80's by the groups of Snezhko and Kurze [6, 14]. In the course of time, various terminologies have been used for what is, essentially, the same technique: Micro-arc oxidation, plasma chemical oxidation, micro-plasma oxidation, anodic oxidation by spark discharges, and anode spark electrolysis are just a few terms which largely represent PEO [6, 14]. In the last three decades, the work focused on the refinement of the produced coatings by adjustments in the process. This is mainly driven by the attraction for many applications and, nowadays, PEO has established itself in a number of niche applications in surface engineering [14, 15].

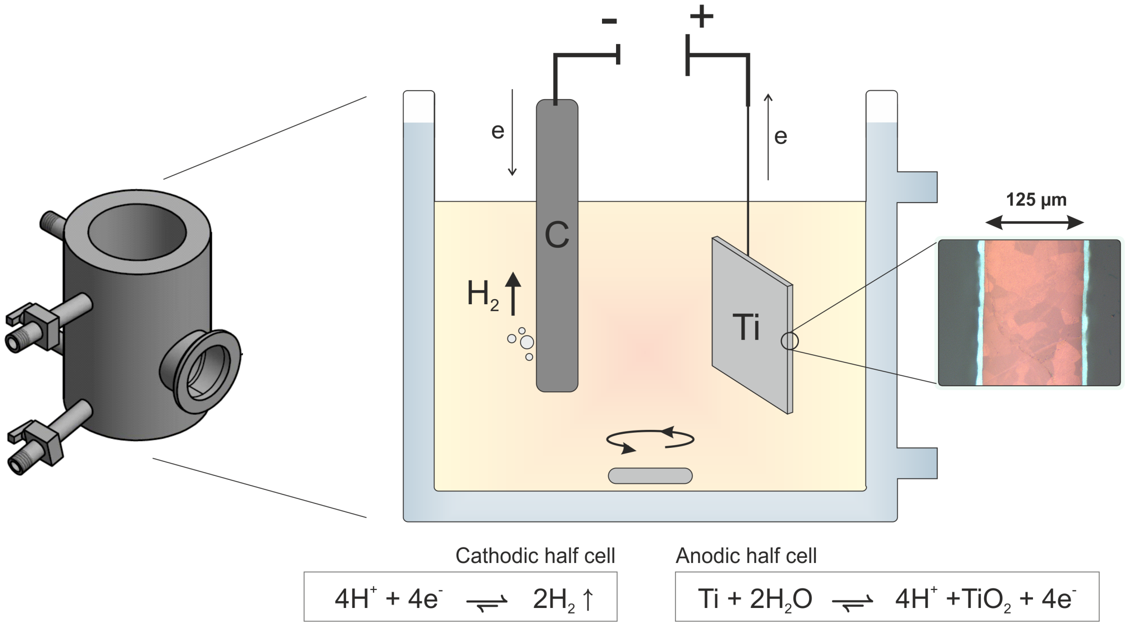

Figure 0.1: A sketch of the employed electrolytic cell for PEO, basically consisting of anode, cathode and electrolyte. The glass vessel exhibits an integrated glass shell for temperature regulation. Some feeds and drains, as well as a quartz window for optical investigations, are indicated in the left sketch. The cathodic and anodic half cell reactions for titanium oxidation are given below. A light microscopy image of the cross section of a plasma electrolytically oxidized titanium foil is shown on the right side.

Despite its commercial use, the understanding of PEO is far from complete. The selected process parameters are often based on purely empirical results. This is partly due to the highly complex nature of PEO. The primary technical setup for PEO of titanium is no more complicated than for the underlying anodization, see the electrochemical cell in Figure 0.1. However, it differs from conventional anodization when the applied potential exceed a distinct value. From then on, dielectric discharges occur and interact with processes of oxide formation and dissolution. In order to describe the entire process, extensive knowledge from various fields (e.g. plasma physics, electro-chemistry, electrical engineering, transport phenomena, heat transfer) is required.

While the objective of conventional anodization is usually a compact oxide layer, PEO is used to obtain a porous or nanotubular TiO_2 layer. The porous morphology of plasma electrolytic oxidized titanium exhibits superior advantages in certain fields of applications, e.g. osseointegration for permanent medical implants or photocatalytic devices [16]. The large surface to volume ratio is also attractive for an application as a sensor material for gas detection. In general, titanium oxide fulfills a number of criteria for being used as a sensor material. First of all, the gas adsorption on TiO_2 is neither too strong nor too weak. This goes along with the second prerequisite; the material needs to be stable at various temperatures. Third, TiO_2 usually belongs to the (n-type) semiconducting metal oxides (SMOX). This means that the charge carrier concentration is at the appropriate level in order to detect changes in electrical material properties on the adsorption of gases. Other prominent SMOX representatives for gas sensing are SnO_2, WO_3, ZnO (n-type) and CuO, Cr_2O_3 (p-type) [17]. Useful advantages of SMOX include the comparatively simple and inexpensive electrochemical fabrication and the potential integration into Micro Electro Mechanical Systems (MEMS), which allows easy embedding into existing structures.

Numerous studies have focused on TiO_2 and its application as a sensor material. It is either exploited for reductive gases like hydrogen (H_2), carbon monoxide (CO), ammonia (NH_3), hydrogen sulfide (H_2S), and volatile organic compounds (VOCs), or for oxidative gases like oxygen (O_2) and nitrogen dioxide (NO_2) [18]. In this work, the focus is on a sensor setup, which includes a Schottky barrier at a metal/TiO_2 interface. The interface exhibit rectifiying properties, which are sensitively influenced by surface adsorption and can therefore be used to determine gas concentrations. Hereby, the use of metals with catalytic activity, e.g., palladium (Pd) and platinum (Pt), promises to improve the performance and enables the operation at low temperatures. Early investigations with Pt/TiO_2 junctions concentrated on the detection of reducing gases. In 1979, Yamamoto et al. were one of the first to use Pt in contact to TiO_2 in order to form a hydrogen-sensitive Schottky diode that operated at room conditions [19]. One year later, Harris presented a hydrogen detector based on a Pt/TiO_2/Ti sandwich structure [20]. The basic idea of hydrogen sensing with Pt/TiO_2 remained popular, so to this day, various ways have been proposed to improve its performance [21–26]. Its commercial relevance for hydrogen sensing is attested by several patent specifications from the last decade [27–29].

In terms of oxidizing gases, oxygen is obviously the most prominent representative, but Pt/TiO_2 junctions are less frequently applied for oxygen sensing. In the early

1990's, Schierbaum and others extensively investigated the interaction of Pt/TiO_2(110) with oxygen [30–33]. A remarkable sensitivity but limited detection range for oxygen was found. Keeping the current constant across the interface, resulted in an almost logarithmic dependence of the voltage on the oxygen partial pressure. This implies that the sensitivity decreases with increasing oxygen concentrations. At high oxygen partial pressures, e.g., in ambient air, the interface is almost saturated and changing the partial pressure has only minor effects on the electrical properties. Nevertheless, results in this thesis indicate that the Pt/TiO_2 interface can be exploited for oxygen sensing under certain conditions.

The present thesis is divided into three chapters. In chapter one, the basic properties of oxygen, platinum and, especially, titanium dioxide will be discussed. Chapter two addresses plasma electrolytic oxidation (PEO) in detail and includes experimental results on the tailoring of titanium dioxide coatings. The third chapter starts to discuss the oxygen and platinum adsorption on TiO_2, before the final experimental investigation focuses on the interaction of the produced Pt/PEO-TiO_2 samples with oxygen.

1 Fundamentals

This section briefly discusses the key elements and compounds in this work to provide a foundation for the remaining chapters.

1.1 Oxygen

Oxygen is the element with the atomic number eight and exhibits the electron configuration [He] $2s^2\,2p^4$ in a neutral state. It is the most electronegative element after fluorine. This fact combined with the electron configuration already indicates a strong tendency for atomic oxygen to form chemical compounds. At standard temperature and pressure, two oxygen atoms readily bind to form molecular oxygen O_2. Above –183 °C, O_2 is a colorless and odorless gas [34]. The gas density is 1.429 g/l (at 0 °C and standard pressure) and therefore around 1.1 times more dense than air at the same conditions [35].

The most stable form of neutral O_2 is a triplet spin configuration, marked by the term symbol $^3\Sigma_g^-$. In this configuration, O_2 has two unpaired valence electrons with the same spin. This fact induces characteristic properties of triplet O_2, such as its paramagnetism. Despite its diradical nature, triplet O_2 is quite stable. This is due to the conservation of spin, when forming new bonds or enter chemical reactions. The vast majority of (organic) compounds have valence electrons with paired spins [36]. For a reaction with these compounds, two radicals with the same spin must be formed, but “these initial radical products are usually high energy reactive intermediates and their formation will be slow” [37]. An energetic transition of the molecule into a singlet state can also result in a reaction, but again the transition energy from the triplet state to the singlet state is quite high (0.98 eV) [38]. Ultimately, the spin conservation in oxygen reactions prevents that many organic compounds just combust in the ambient atmosphere [37].

1.2 Platinum

Platinum (Pt) is a transition metal with the atomic number 78. Its neutral electron configuration is $[\mathrm{Xe}]\,4\mathrm{f}^{1}4\,5\mathrm{d}^{9}\,6\mathrm{s}^{1}$ and induces paramagnetic properties. Platinum is a very versatile material and has a wide scope for utilization. It belongs to the least reactive metals, even at high temperatures it is quite stable. Therefore, it is considered as noble metal. This also justifies its applicability as electrical lead or contact/electrode material. In contrast to this chemical inertness, platinum is also known for its catalytic activity.

In heterogeneous catalysis, the gaseous reactant has to adsorb on the solid surface without forming a compound. The Sabatier principle describes the appropriate bonding strength for a high catalytic activity. Herein, a chemisorption of the reactant is required which must be neither too weak nor too strong. A strong chemisorption means a strong bonding, which commonly goes along with a long surface-residence time [39]. However, for an catalytic process a rapid turnover reaction is commonly desired. Otherwise, the catalytically active sites are temporarily blocked. On the other side, the bonding with the interface should not be too weak, cause the catalytical process involves bond breaking. The bond breaking is assumed to be induced by local low-energy electronic fluctuations with the substrate, which include charge fluctuations, configuration fluctuations, spin fluctuations and term and multiplet fluctuations [39]. In case of Pt, the incomplete filled d band plays a decisive role for its catalytic activity. The 10-fold degeneracy and relatively narrowness of the d-band provide a high density of states, which facilitates electronic fluctuations [40]. In addition, fluctuation-inhibiting effects, such as Coulomb repulsion, are only weakly pronounced [40].

A well-known catalysis on platinum is the oxidation of hydrogen, which is commonly exploited in fuel cells. The corresponding half-cell reaction at a cathode,

$$\frac{1}{2}\,\mathrm{O}_2 + 2\,\mathrm{H}^+ + 2\,\mathrm{e}^- \xrightleftharpoons{\mathrm{Pt}} \mathrm{H}_2\mathrm{O} \qquad (E^0 = 1.23\,\mathrm{V}), \tag{1.1}$$

controls the overall activity of a fuel cell and is also referred to as oxygen reduction reaction (ORR). The ORR is one of the best studied electrochemical reactions and platinum has shown the highest catalytic activity for it among all elements. Fig. 1.1 shows theoretical results from Norskov et al. [41], which are in good agreement with experimental results. Herein, the oxygen reduction activity of different transition metals is plotted versus the corresponding binding energies of oxygen. The resulting volcano plot validates the Sabatier principle and indicates that even higher activities can be achieved with slightly higher binding energies than for Pt, which may be realized by alloying Pt. A mutual key step in the ORR and in oxygen sensing, is the dissociation of molecular oxygen. Therefore, Pt is commonly exploited for improving the performance in oxygen sensing.

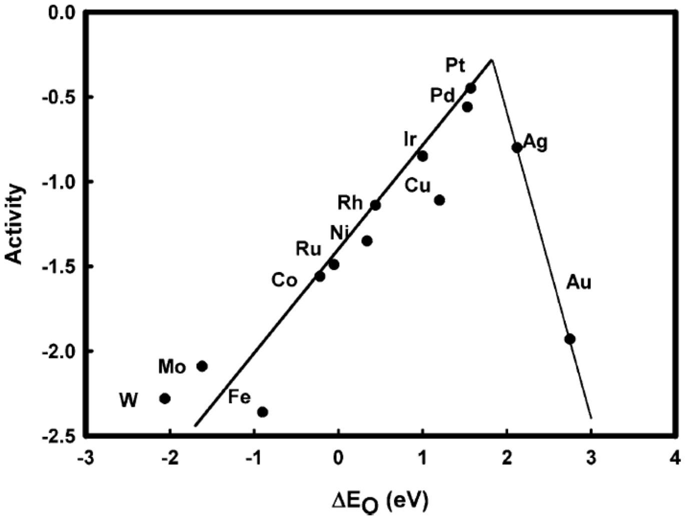

Figure 1.1: Calculated oxygen reduction activity in dependence of the oxygen binding energy ΔE_O for different transition metals. Figure reprinted with permission from [41]. © (2004) American Chemical Society.

In general, the catalytic activity of Pt depends strongly on its surface structure. The activity is promoted by rough, kinked, and stepped surfaces. In addition, the activity is also promoted by point defects, which will increase the sticking probability of adsorbates at room temperature [42]. In combination with the effort to maximize the reactive surface area, nanoparticles of platinum are commonly used. In the present work, platinum was sputter deposited on electrochemical produced TiO_2. A cluster formation is assumed, which is supported by SEM results [43] and several studies, which were using a similar preparation method [44, 45].

1.3 Titanium Dioxide

Titanium is defined in the periodic table by the atomic number 22 and belongs to the transition metals. Its neutral electron configuration is [Ar] $3d^2\,4s^2$. In its ground state, the two d-electron spins are parallel adjusted and induce paramagnetic properties. At standard temperature and pressure, it will crystallize into hexagonal α-Ti. Above approximately 882 °C, it changes to a body-centered cubic lattice, which is referred to as β-Ti [46]. With different alloying elements, either the alpha or the beta phase can be stabilized [47]. The melting temperature is approximately 1668±5 °C [48]. From a technical point of view, the combination of excellent corrosion resistance, high strength-to-weight ratio and good fatigue resistance is of particular interest [49].

However, pure titanium hardly ever occurs in nature. One reason for this, is its strong tendency to form bonds with paramagnetic O_2. At ambient atmosphere or in oxygen containing liquids a native oxide layer up to several nm forms [1]. The oxide layer serves as a protective passive layer and accounts for the before-mentioned excellent corrosion resistance of the titanium substrate. The formation of the oxide layer and technical functionalization is further discussed in chapter 2.

The oxidation states of titanium in common titanium oxides range from +2 to +4, which is due to the two 3d and two 4s valence electrons. The corresponding oxides are TiO (+2), Ti_2O_3 (+3) and TiO_2 (+4). In addition, other stoichiometries occur. The forming of the oxide strongly depends on the pressure, temperature and ratio of oxygen to titanium, which is summarized in the phase diagram in Fig. 1.2. The regions between Ti_2O_3 and TiO_2 also contains Ti_3O_5 and seven discrete phases of the homologous series Ti_nO_{2n-1}, which are sometimes referred to as Magneli phases. At atmospheric pressures only titanium dioxide TiO_2, also known as titania, occurs [50]. For the present work, TiO_2 is most relevant and will be discussed in detail in the following.

Spatial Structure

Titania has at least eight polymorphs [50]. In nature, rutile and anatase occur, while brookite is less frequent. The former is a stable polymorph, while anatase and brookite are metastable. At elevated temperatures both polymorphs will transform constructively and irreversible into the stable rutile form. The conventional unit cells are presented in Fig. 1.3. Characteristic for all polymorphs is the more or less distorted octahedral TiO_6 configuration. Rutile forms a tetragonal lattice ($P4_2/mnm$, a=b=4.584 Å , c=2.953 Å), anatase as well ($I4_1/amd$, a=b=3.782 Å, c=9.502 Å), and brookite crystalizes in a rhomboedrical lattice (Pbca, a=5.436 Å, b=9.166 Å, c=5.135 Å) [51]. Due to its low abundance and difficult synthesis, brookite is not relevant to many studies, including this one.

The initial crystal phase in forming TiO_2 is typically anatase. From a structural point of view, this can be explained by the density of the TiO_6 octahedra. The unit cell

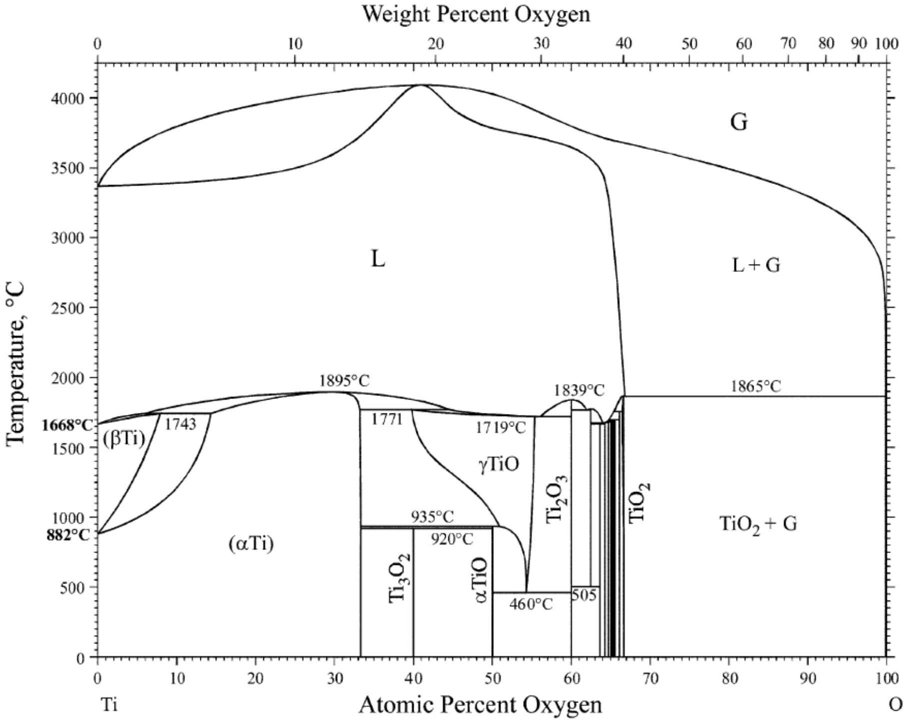

Figure 1.2: The phase diagram of Ti-O. Figure reprinted with permission from [48]. © (2011) Springer Nature.

volume is about 0.0624 nm^3 for rutile and 0.1363 nm^3 for anatase, which also affect both mass densities (rutile with 4250 kg m^{-3} and anatase with 3894 kg m^{-3}) [50]. It is assumed that an arrangement of the TiO_6 octahedra into the anatase order is favored compared to the dense rutile order. From the thermodynamic point of view, the fact is contradictory at first. Bulk anatase has a higher formation enthalpy than rutile ($\Delta H = 2.61$ kJ/mol) and should be formed preferentially [53]. However, for very small particles, the contribution of the surface enthalpy to the total enthalpy dominates. The surface enthalpy of anatase (0.4 ± 0.1 J m^{-2}) was found to be significant smaller than for rutile (2.2 ± 0.2 J m^{-2}) [53]. Thus, the overall enthalpy becomes larger for rutile than for anatase below a certain particle size (estimated to 14 nm) and, therefore, anatase is initially formed in various methods of anodization [54].

This is in contrast to the phase stability of larger titania particles at elevated temperatures. Pure bulk anatase starts to transform into rutile in an irreversible and constructive process (nucleation and growth) above approximately 600 °C. However, the transformation temperature depends on the oxidation method and the experimental conditions. It may range from 400 °C to 1200 °C [50]. The constructive transformation involves bond breaking and the formation of new bonds, which makes the transformation sensitive to the oxidation time. Thus, the transformation can be kinet-

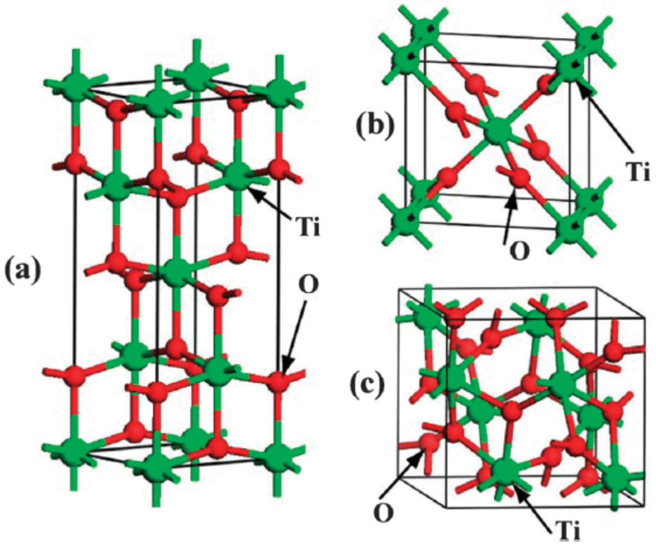

Figure 1.3: The conventional unit cells for TiO_2 (**a**) anatase, (**b**) rutile and (**c**) brookite. Figure reprinted with permission from [52]. © (2011) Springer Nature.

ically inhibited even at high temperatures, when the oxidation time is insufficient.

Electronic Structure

The electronic structure of TiO_2 can be described within the band model. The polymorphs slightly differ in their electronic structure. Fig. 1.4 shows the density of states for rutile, anatase and brookite, determined by a combined density functional theory and many-body perturbation theory study [55]. The vast majority of Ti3d states are unoccupied, since titanium valence electrons are transferred to oxygen in TiO_2. These states form the lowest states in the conduction band. The valence band is mainly derived from O2p states, which partially hybridize with Ti3d states to form σ- or π- type states. The distinct gap around 6 eV in the unoccupied Ti3d states, originates from crystal field splitting. As a consequence of the octahedral coordination of the titanium ions, the corresponding states split into t_{2g} (lower energy range) and e_g states (higher energy range) [33].

The band gap energies for rutile, anatase and brookite are 3.02 eV, 3.23 eV and 3.14 eV, respectively [56]. When regarding the **k**-resolved band structure, it is often reported that anatase shows an indirect band gap with a marginally smaller energy than the direct gap at the Γ point [52, 55].

Titania is well known for its dielectric properties. Rutile single crystals shows static dielectric constants of ϵ_c=170 (along the c-axis) and ϵ_a=86 (along a-axis) at 300 K [57].

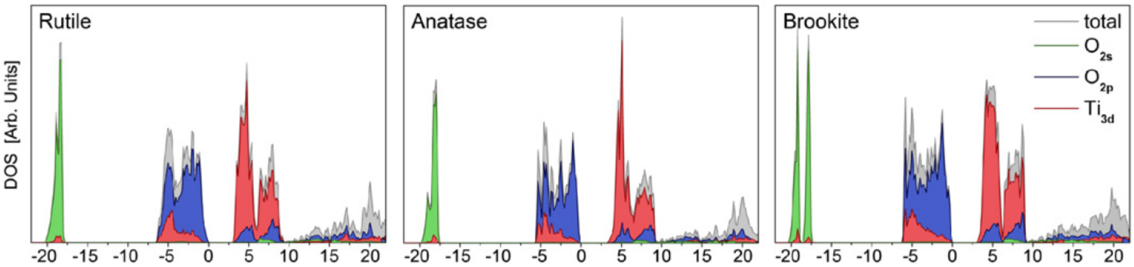

Figure 1.4: The density of states for the TiO_2 polymorphs rutile, anatase and brookite (in eV relative to E_F). The Ti3d, O2s and O2p contributions are considered. Figure reprinted with permission from [55]. © (2012) IOP Publishing, Ltd.

However, the reported dielectric constants for anatase are significantly lower. From thin films, containing a mixture of rutile and anatase, it was evaluated that the mean dielectric constants were 45±3.9 and 127±2.8 for anatase and rutile, respectively [58].

The electronic properties of TiO_2 and other binary transition oxides depend strongly on the defect chemistry in the bulk and on the surface. This issue will be briefly discussed in the following sections.

Defect Chemistry

All polymorphs have a rather large bandgap, which makes TiO_2 an electrical insulator. However, a small deviation from the ideal stoichiometry by intrinsic defects can change its electrical properties significantly. Most prominent is the formation of oxygen vacancies, which results in an oxygen deficit stoichiometry. Oxygen vacancies induce intrinsic donator states in the band gap and ultimately makes TiO_{2-x} a n-type semiconductor. This process involves the excorporation of molecular oxygen, O_2. Using the Kröger-Vink notation the equilibrium can be expressed as

$$\mathrm{O}_\mathrm{O}^{\times} \rightleftharpoons \mathrm{V}_\mathrm{O}^{\bullet\bullet} + 2\,\mathrm{e}' + \frac{1}{2}\,\mathrm{O}_2 \quad , \tag{1.2}$$

where $\mathrm{V}_\mathrm{O}^{\bullet\bullet}$ and $\mathrm{O}_\mathrm{O}^{\times}$ represents a double ionized oxygen vacancy and lattice oxygen, respectively. The electrons become delocalized and may populate certain defect states in the band gap or are thermally excited to the bottom of the conduction band. The delocalization will leave two $\mathrm{Ti}_\mathrm{Ti}^{3+}$-ions in the lattice behind. Using the mass action law for the equilibrium (1.2), an oxygen partial pressure dependence of the concentrations can be estimated. Thus, the electron concentration n is linear to ${p_{O2}}^{-1/6}$, which can be experimentally confirmed by measuring the bulk conductivity [59]. Prerequisite for the approach, is the neutrality condition $[\mathrm{e}'] = 2[\mathrm{V}_\mathrm{O}^{\bullet\bullet}]$ and the assumption that $[\mathrm{O}_\mathrm{O}^\times]$ is constant. Occasionally, singly ionized vacancies are also considered [60].

Using the equilibrium

$$\mathrm{O}_\mathrm{O}^\times \rightleftharpoons \mathrm{V}_\mathrm{O}^{\bullet} + \mathrm{e}' + \frac{1}{2}\,\mathrm{O}_2 \quad , \tag{1.3}$$

it is derived analogously that n is linear to ${p_{\mathrm{O}2}}^{-1/4}$. In general, the degree of defect ionization is assumed to depend on the temperature [61]. It is assumed, that at room temperature the vacancies are fully ionized [62]. Typical donor concentrations are reported to be in the magnitude of 10^{19}–10^{20} cm^{-3} for TiO_2, which was anodically grown at low voltages in 0.5 M $\mathrm{H_2SO_4}$ [63].

Besides oxygen vacancies, other intrinsic point defects occur. The formation of interstitial titanium also generates delocalized electrons. Just as in equation 1.2, molecular oxygen leaves the lattice, according to the equilibria

$$\mathrm{O}_\mathrm{O}^\times + \mathrm{Ti}_\mathrm{Ti}^\times \rightleftharpoons \mathrm{Ti}_\mathrm{i}^{\bullet\bullet\bullet} + 3\,\mathrm{e}' + \frac{1}{2}\,\mathrm{O}_2 \quad , \tag{1.4}$$

$$\mathrm{O}_\mathrm{O}^\times + \mathrm{Ti}_\mathrm{Ti}^\times \rightleftharpoons \mathrm{Ti}_\mathrm{i}^{\bullet\bullet\bullet\bullet} + 4\,\mathrm{e}' + \frac{1}{2}\,\mathrm{O}_2 \quad . \tag{1.5}$$

Thereby, fully ionized titanium interstitials are preferably formed at appropriate conditions, due to the relatively low ionization energies in TiO_2 [64]. In the case of $\mathrm{Ti}_\mathrm{i}^{\bullet\bullet\bullet\bullet}$ and $\mathrm{Ti}_\mathrm{i}^{\bullet\bullet\bullet}$, the electron concentration can be estimated to be linear to ${p_{\mathrm{O}2}}^{-1/5}$ and ${p_{\mathrm{O}2}}^{-1/4}$, respectively.

In general, the energy for the formation of titanium interstitials is higher compared to the energy for the formation of oxygen vacancies. Intuitively, this can be understood in the image of the Born model: Herein, the energy is linear to z^2e^2/r_d, where z is the charge number, e the elementary charge and r_d the radius of the defect. When neglecting the difference in radius between $\mathrm{V}_\mathrm{O}^{\bullet\bullet}$ and $\mathrm{Ti}_\mathrm{i}^{\bullet\bullet\bullet\bullet}$, the energy for the defect formation of $\mathrm{Ti}_\mathrm{i}^{\bullet\bullet\bullet\bullet}$ is four times larger than for $\mathrm{V}_\mathrm{O}^{\bullet\bullet}$ [64]. This is also reflected in results from temperature-controlled conductivity measurements. With increasing temperature, titanium interstitials contribute progressively and eventually start to dominate the conductivity, which is determined by the change in the slope $\partial\sigma/\partial p_{\mathrm{O}2}$. In anatase samples, the transition was observed around 600 °C, while rutile samples show the transition around 900 °C [64, 65]. The lower temperature transition in anatase indicate that the formation of titanium interstitials are more favorable in anatase compared to rutile. This can be rationalized by the lower lattice density of anatase, which facilitates the formation of interstitials.

The previous point defects arise in reducing atmospheres, which is also evident from the oxygen deficit in the stoichiometry TiO_{2-x}. According to Chatelier's principle, the equilibria 1.2–1.5 shift to the nondefect stoichiometry when more molecular oxygen is provided. When oxygen is further provided, it may result in an excess of oxygen in the lattice, which corresponds to the notation TiO_{2+x}. With a different perception, it can also be considered as a deficit of metal atoms, represented by the equivalent notation $Ti_{1-y}O_2$. Either way, an ongoing oxidation at a sufficient temperature is accompanied by the formation of titanium vacancies $V_{Ti}^{''''}$, according to the equilibrium

$$\mathrm{Ti}_{\mathrm{Ti}}^{\times} + \mathrm{O}_2 \rightleftharpoons \mathrm{TiO}_2 + \mathrm{V}_{\mathrm{Ti}}^{''''} + 4\mathrm{h}^{\bullet} \quad , \tag{1.6}$$

where $h^{\bullet}$ denotes an electron hole. The formation of TiO_2 indicates the expansion of the volume in the process. At oxidizing conditions, the major charge carriers are electron holes, which makes the material a p-type semiconductor. By applying the mass action law to the equilibrium (1.6) and assuming that the neutrality condition $2[\mathrm{V}_{\mathrm{Ti}}^{''''}] = [\mathrm{V}_{\mathrm{O}}^{\bullet\bullet}]$ is valid, a dependence of the electron concentration $n \sim {p_{\mathrm{O2}}}^{-1/4}$ or electron holes concentration $p \sim {p_{\mathrm{O2}}}^{1/4}$ can be estimated.

Nowotny et al. [66] summarized the defect concentrations and corresponding conductivity in dependence to the oxygen partial pressure in an isothermal diagram, which is seen in Fig. 1.5. The diagram gives an impression of how the defect concentrations behave at equilibrium conditions at 1073 K. In practice, the observation of the predicted conductivity is complicated due to several factors. One common reason is an inhibited kinetic of defect formation, which occurs especially at lower temperatures. Therefore, the thermodynamic equilibrium is often not reached. In addition, the spatial structure, unintentional dopants, or additional reactive components in the atmosphere may affect the thermodynamic equilibrium and the kinetic of defects.

Overall, the exact description of the neutrality condition has to include all charged defects, according to

$$[\mathrm{V}_{\mathrm{O}}^{\bullet}] + 2[\mathrm{V}_{\mathrm{O}}^{\bullet\bullet}] + 3[\mathrm{Ti}_{\mathrm{i}}^{\bullet\bullet\bullet}] + 4[\mathrm{Ti}_{\mathrm{i}}^{\bullet\bullet\bullet\bullet}] + [\mathrm{D}^{\bullet}] + p = n + [\mathrm{A}^{'}] + 4[\mathrm{V}_{\mathrm{Ti}}^{''''}] \quad . \tag{1.7}$$

Hereby, $[\mathrm{A}^{'}]$ and $[\mathrm{D}^{\bullet}]$ denote the intended or unintended (acceptor- or donator-type) ions.

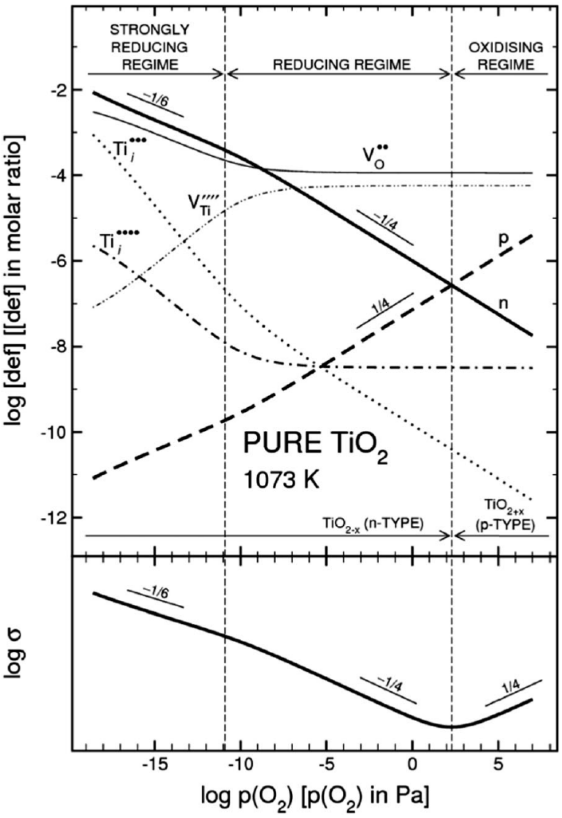

Figure 1.5: Isothermal defect disorder diagram of intrinsic lattice species and the corresponding conductivity of bulk TiO_2 at 1073 K. Figure reprinted with permission from [66]. © (2015) Royal Society of Chemistry.

In the concept of electronic band structure, point defects are primarily prominent due to related states in the band gap. In general, the states are summarized in a defect band E_d, which is situated 0.1 eV below the conduction band minimum and has a maximum density of states at 0.9 eV below the Fermi energy, E_F [67]. An early investigation from Henrich et al. determined the center of the defect band approximately 1 eV below E_F [68]. The authors contributed the DOS to surface oxygen vacancies. This interpretation still forms the common conception today and was confirmed in numerous studies. For instance, a combined UPS and STM study on $TiO_2(110)$ showed that the population of the band gap state increases directly with the density of bridging vacancy sites, V_br [69]. The experimental results are shown in Fig. 1.6a. However, the limitation on oxygen vacancies was controversial and the concept was extended in the progress of research.

Water adsorbs dissociatively at surface vacancy sites, leaving bridging hydroxyl groups, OH_br, behind. Outgoing from this finding, different studies indicate that these OH groups can also contribute to the defect band. For instance, a combined UPS and DFT study on slightly reduced $TiO_2(110)$ indicate a linear increasing relationship between OH coverage and the band gap intensity [70], which is illustrated in Fig. 1.6b. Based on STM and PES results, Wendt et al. objected that titanium interstitials Ti_{int} in the subsurface significantly affect the defect band intensity [71]. Other studies have also been able to confirm a contribution of Ti_{int} to the DOS, however, in most studies the contributions by Ti_{int} are small in comparison to the contribution of V_{br} [72]. Summarized, the defect states can be caused by V_{br}, OH_{br} and Ti_{int}. However, the relative contribution of the species strongly depends on the experimental conditions. For a detailed overview of the electronic band structure of TiO_2, see the report of Yin et al. [72].

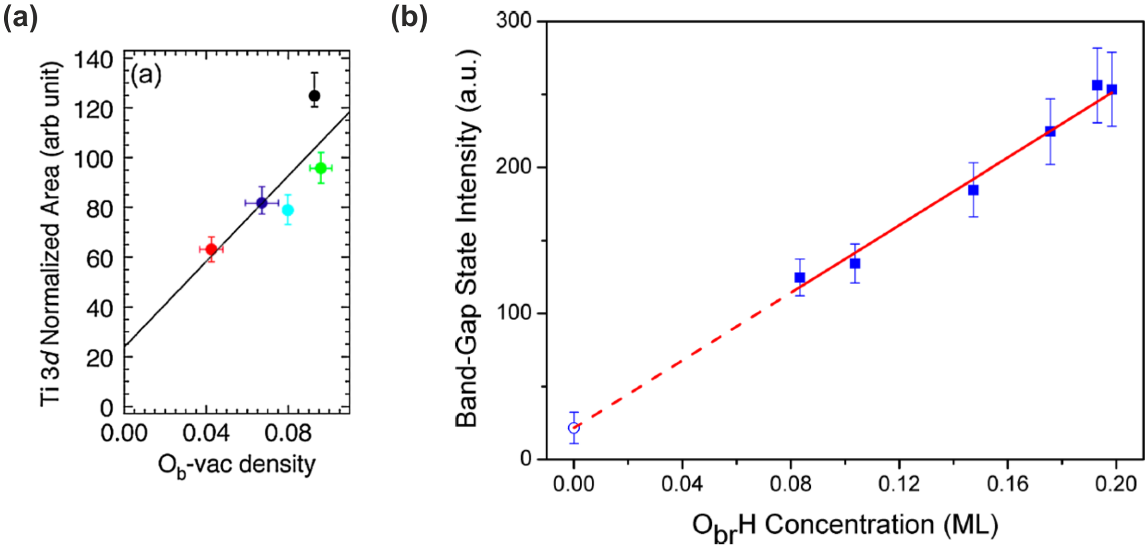

Figure 1.6: Normalized integrated intensities of the band-gap state on rutile $TiO_2(110)$, derived from UPS measurements. (**a**) The intensity as a function of surface bridging oxygen vacancies, V_{br}, which were determined by STM [69]. Figure reprinted with permission from [69]. © (2010) American Physical Society. (**b**) The intensity plotted versus the OH_{br} concentration [70]. Figure reprinted with permission from [70]. © (2013) American Chemical Society.

Relevant Surfaces

In surface science of metal oxides, TiO_2 is one of the most investigated materials. Accordingly, the number of studies is quite large. The focus in the following section will be on the two most relevant representatives from anatase and especially rutile. However, they are only briefly described due to the limiting transferability to polycrystalline samples. For a detailed overview of the surface science on TiO_2, the reviews from U. Diebold [51] or, with a focus on photocatalysis, from M. Henderson [73] is recommended.

When the orientation of the crystal surfaces is analyzed, it is frequently found that the R(110)-surface (rutile) and the A(101)-surface (anatase) are more abundant compared to other surfaces. The preferred formation of these surfaces can be rationalized by their surface energies: For rutile, the (110) surface and for anatase, the (101) has the least surface energy and, therefore, are thermodynamically favored [74, 75]. This is one reason why a basic understanding of both surfaces is relevant for many preparation methods and technological applications.

The A(101) surface has received more attention in the last two decades due to its possible role in energy and environmental technology. A recent study showed its potential by forming a titanium-terminated A(101) sample with a decreased band gap energy below 2 eV [76]. Even though other surfaces, i.e. the (001)-surface, might be superior to the (101) surface in terms of reactivity [77].
In general, the R(110) surface is by far the most studied TiO_2 surface and is often used as a model system. This is due for several reasons. First of all, it is the most stable surface orientation and is most common in different preparation methods. Therefore, it is well-suited for reversible solid-gas interaction. Second, it can be well characterized, due to the ability to control its defect density [51]. In addition, ultraviolet photoemission spectra show, that the surface has no appreciable density of surface states in the bulk band gap [78]. Therefore, the states induced by intrinsic or extrinsic point defects become more important and easier to access in experiments.

At standard conditions the defect free R(110)-surface terminates with a (1×1) reconstruction. Under reducing conditions, i.e., in ultra-high vacuum and at elevated temperatures, a (1×2) symmetry also occurs. For A(101), the (1×1) termination is stable [75]. In comparison to R(110), the A(110)-surface has a stronger tendency to form step edges. This induces fourfold coordinated titanium atoms at the edges, which are more reactive to gas interactions [79].

Fig. 1.7a shows a ball model of the A(101)-surface (top) and R(110)-surface (bottom) [80]. Both surfaces have sixfold coordinated titanium atoms, Ti_{6c}, and fivefold coordinated titanium atoms, Ti_{5c}. In contrast to Ti_{6c}, Ti_{5c} is coordinatively unsaturated with one dangling bond. The density of Ti_{5c} is quite similar for A(101) and R(110) with 5.16×10^{14} sites/cm^2 and 5.20×10^{14} sites/cm^2, respectively [75]. There are also two kinds of oxygen sites: Threefold coordinated oxygen, O_{3c} and twofold oxygen, O_{2c}. The R(110)-surface has a main surface plane, in which O_{3c} is located. In contrast to O_{3c}, O_{2c} are slightly isolated from the main plane. It is also referred to as bridging oxygen, O_{br}. Due to its location and coordinative undersaturation, bridging oxygen is considered to be of special importance. For example, during dissociative water adsorption at the non-defect surfaces. Figure 1.7b shows schematically, how water molecules bond initially with their oxygen end at undercoordinated Ti_{5c} sites on the R(110)-surface (top) or A(101)-surface (bottom). Subsequently, water may dissociate by transferring a hydrogen atom to the adjacent O_{br} atom and leaving behind two individual hydroxyl groups. A recent study clarifies that the energy difference between the dissociated and the intact configuration on TiO_2 is very small. With this small preference to the intact configuration, already a change in temperature may be sufficient to promote dissociation.

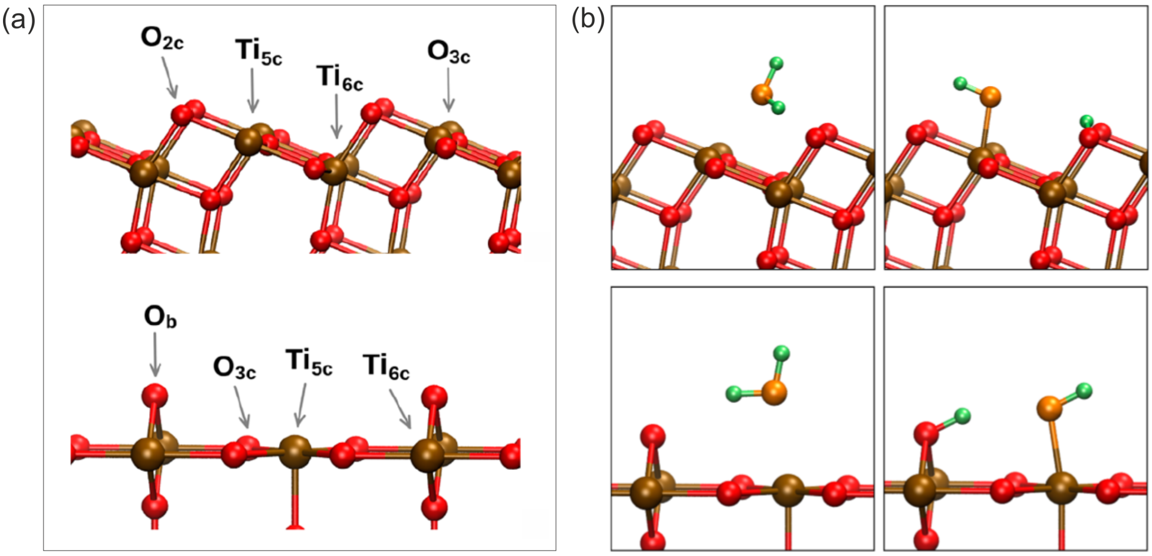

Figure 1.7: (**a**) Ball model of the rutile TiO_2(110)-surface (top) and anatase TiO_2(101)-surface (bottom) with characteristic surface sites. (**b**) Illustrated water dissociation on both surfaces. Figures reprinted with permission from [80]. © (2017) American Chemical Society.

Overall, surface defects are known to crucially control associative or dissociative adsorption processes. Especially, surface oxygen vacancies V_O, which form preferentially at bridging oxygen sites, play a decisive role [51]. Typical values for oxygen vacancy concentrations on R(110) samples range from 2–8% ML [81]. Surface oxygen vacancies are commonly formed by annealing (in vacuum), electron bombardment or UV irradiation. For instance, the annealing of a R(110)-crystal in UHV at 850 K for 10 min typically results in a bridging oxygen vacancy population on the surface of about 8% (approximately 4×10^{13} sites/cm^2) [82]. In comparison to R(110), A(101) does not show a strong tendency for losing O_{2c} upon annealing in ultrahigh vacuum [75]. In general, the density of vacancies appears to be much lower, although step edges are more common and therefore undercoordinated oxygen should favor vacancy formation [51]. Results from a STM study indicate that defects on anatase reside predominantly on the subsurface and form linear chains, which might explain the lower density observed in several experiments [83]. With a perspective on gas interaction, it is assumed that subsurface defects are less reactive than surface oxygen vacancies. The authors from the STM study also emphasize that the exclusive focus on oxygen vacancies (Schottky defects) falls short and should be extended with the consideration of other point defects, i.e. titanium interstitials and titanium vacancies [83]. Even though the oxygen deficit is often a good indicator for macroscopic parameters as the electrical conductivity, for a profound understanding of surface interactions, a combination of point defects should be considered [60].

2 PEO-TiO_2

2.1 Oxide Formation

2.1.1 In Equilibrium

Titanium belongs to a group of metals which are not stable even in neutral solution, which is reflected by the very negative standard electrode potential (E^0 = -1.63 V) for the equilibrium reaction

$$\mathrm{Ti}^{2+} + 2\,\mathrm{e}^- \rightleftharpoons \mathrm{Ti} \quad . \tag{2.1}$$

However, instead of metal solvation, a passivating oxide layer is formed in oxygen containing solutions. For instance, TiO_2 is formed in neutral water. The chemical reaction proceeds in steps, where hydration states and lower oxidation states occur as intermediates. A plausible sequence of reaction steps [84] are

$$\begin{aligned}
\mathrm{Ti} + \mathrm{H_2O} &\rightleftharpoons \mathrm{Ti(H_2O)_{ad}} \\
\mathrm{Ti(H_2O)_{ad}} &\rightleftharpoons \mathrm{Ti(OH^-)_{ad}} + \mathrm{H^+} \\
\mathrm{Ti(OH^-)_{ad}} &\rightleftharpoons \mathrm{(TiOH)_{ad}} + \mathrm{e^-} \\
\mathrm{(TiOH)_{ad}} &\rightleftharpoons \mathrm{(TiOH)^+_{ad}} + \mathrm{e^-} \\
\mathrm{(TiOH)^+_{ad}} &\rightleftharpoons \mathrm{(TiOH)^{2+}_{ad}} + \mathrm{e^-} \\
\mathrm{H_2O} + \mathrm{(TiOH)^{2+}_{ad}} &\rightleftharpoons \{\,\mathrm{Ti(OH)_2}\,\}^{2+}_{\mathrm{ad}} + \mathrm{H^+} + \mathrm{e^-} \\
\{\,\mathrm{Ti(OH)_2}\,\}^{2+}_{\mathrm{ad}} &\rightleftharpoons \mathrm{TiO_2} + 2\,\mathrm{H^+} \quad .
\end{aligned}$$

Simplified, the net reaction is

$$\mathrm{Ti} + 2\,\mathrm{H_2O} \rightleftharpoons 4\,\mathrm{H^+} + \mathrm{TiO_2} + 4\,\mathrm{e^-} \quad . \tag{2.2}$$

In general, the equilibrium potential E for an oxidation or reduction reaction,

$$\mathrm{Red} \rightleftharpoons \mathrm{Ox} + z\mathrm{e}^- \quad , \tag{2.3}$$

can be calculated by the Nernst equation

$$E = E^0 - \frac{kT}{ze} \ln \frac{a_{\mathrm{Red}}}{a_{\mathrm{Ox}}} \tag{2.4}$$

with a_{Ox} and a_{Red} being the activities for reduced and oxidized reactants. All other terms are in accordance with the convention. The activity dependency in the Nernst equation leads to a pH dependency for the reaction (2.2). The equilibrium of titania in water at different levels of pH can be summarized in a Pourbaix diagram, which is shown in Fig. 2.1 (a). Hereby, the dashed lines indicate the region of stable water. For $E \geq 0\,\mathrm{V}$, TiO_2 is stable in a wide range of pH values. In concentrated acids with $\mathrm{pH} < 0$, TiO_2 is reduced and dissolves. The stability of titania in concentrated acid media can be increased by applying anodic potentials.

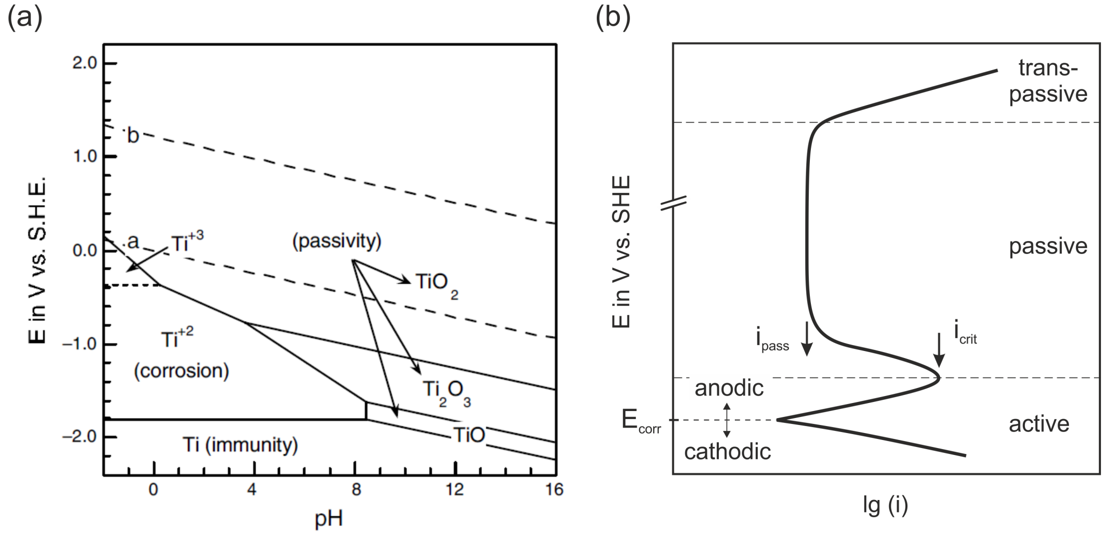

Figure 2.1: (a) Pourbaix diagram for titanium in water at 25 °C. Figure reprinted with permission from [85]. © (2010) Springer Nature. **(b)** Schematic polarization curve for titanium in water (pH=7).

2.1.2 Kinetics with Applied Potential

A Pourbaix diagram is a valuable tool in the preliminary assessment of the thermodynamic stability of a metal in a liquid solution. However, the convenient visualization often simplifies the complex reality [85, 86]. It is usually limited to reactions involving the pure metal and O, OH^- and H_2O without considering solvation [87]. Other dissolved reactants in the aqueous solution or products may also have an impact on the equilibrium. Furthermore, it does not respect the limited solubility of a species, which strongly depends on the pH-value [86]. However, the major drawback is the omission of equilibrium kinetics. In a number of applications, the system is far from thermodynamic equilibrium. The kinetics can be derived from the charges transferred per time, i.e., the current. The logarithmic current density plotted against the applied potential is often referred to as polarization curve. Fig. 2.1 (b) shows a schematic polarization curve. At the corrosion potential E_{corr} or open circuit potential (E_{OCP}) the dissolution and formation currents chancel each other out. Deviations to E_{corr} lead to a rapid increase in current, which is commonly described by the Butler-Volmer equation, which respects a limitation of the charge transfer at heterogeneous interfaces. At sufficiently high overvoltage, the contribution of the reverse reaction at the interface can be neglected and the polarization curve in the vicinity of E_{corr} can be extrapolated by the resulting Tafel equation. With higher anodic potentials the transition from active to passive is indicated by a critical current, i_{crit}. Due to the oxide formation, a passive layer forms and only a small current i_{pass} passes. At even higher anodic potentials, the transpassive region is reached, which involves decomposition, further oxidation, oxygen evolution, electrolyte decomposition or a combination of those [87].

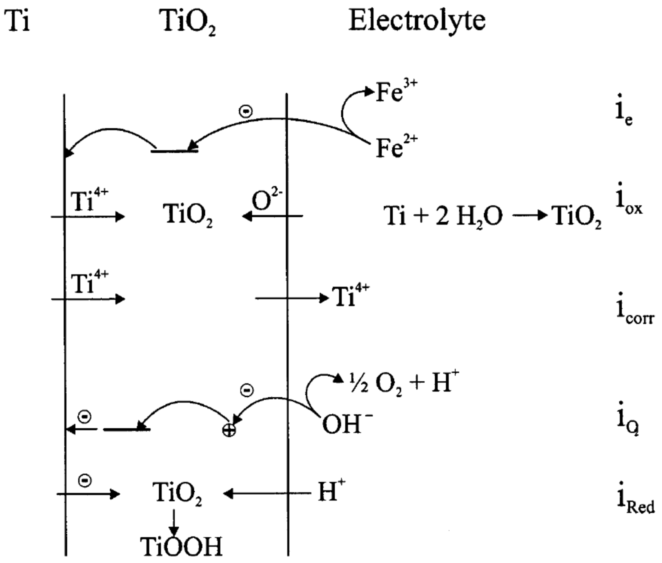

Figure 2.2: Exemplified processes at the Ti/TiO$_2$/electrolyte interface with indicated contributions to the total current. Figure reprinted with permission from [1]. © (2000) Elsevier.

In the passive region the total current is mainly limited by the charge transfer processes in the solid and at the interfaces. A theoretical approach distinguishes the total current density into different contributions [1]. The most important processes are schematically visualized in Fig. 2.2:

- i_{e} describes the electronic charge transport.
- i_{ox} presents the transfer and diffusion of oxygen anions inwards and titanium cations outwards, ultimately leading to oxide formation.
- i_{corr} refers to the transfer of titanium cations into the electrolyte.
- i_{O_2} indicates the anodic oxygen evolution for sufficiently high potentials.
- i_{red} represents reduction reactions.

In addition, a partial current i_{C} can be consumed for capacitive charging. The reduction reactions on TiO$_2$, represented by the current i_{red}, are essentially blocked in anodic polarization. The electronic current i_{e} is relatively low, because the electrical conductivity in TiO$_2$ is small compared to the ionic conductivity. When i_{ox} prevails over anodic corrosion i_{corr}, the oxide layer growths. The growth rate of the oxide layer can be deduced from the individual current contributions to the net current.

2.1.3 Growth Rate

The growth rate $\mathrm{d}L/\mathrm{d}t$ of the oxide layer is according to Faradays law proportional to i_{ox},

$$\frac{\mathrm{d}d}{\mathrm{d}t} = \frac{M}{\rho_{\mathrm{ox}} z F} \cdot i_{\mathrm{ox}}. \tag{2.5}$$

The factor of proportionality contains the molecular weight M, the molecular density of the oxide layer ρ_{ox} and the charge to form one mol oxide zF. The complete discussion of the growth rate considers a closed current circuit, essentially consisting of an anode (for example Ti), cathode, connected power source and an electrolyte. Each element and its interface represents a resistance. Focusing on one electrode, the most relevant reaction steps are

- the ionic transport of reactants in the electrolyte,
- the charge transfer at electrodes, including
  - (partial) removal of solvate shell,
  - double layer migration,
  - charge transfer reaction at solid-liquid phase boundary,
  - diffusion in lattice,
- the transport of products away from the electrode and
- the electronic transport in bulk electrodes.

The overall reaction rate is often dominated by a single reaction step. Typically, this rate-determining step occurs in the charge transfer process in or at the electrode. With an appropriate selection of the cathode, the rate-determining step can be narrowed down to one at the passivated anode. In the most basic approach, it is assumed that the field supported ionic diffusion in the oxide lattice is rate-determining. A first description was made in 1934 by Güntherschultze and Betz and was refined by Verwey in 1935 [9, 88]: Ordinarily the diffusion in an immobile lattice is a thermally activated hopping process of particles from one potential minimum to an adjacent potential minimum. At sufficiently high fields ($F > 10^6\,\mathrm{V/cm}$) and moderate temperatures, the concentration gradient-induced migration can be neglected and the activation energy for the hopping process is lowered by the electrical field F, which ultimately leads to the current density

$$i = i_0 \exp\left(\beta F\right). \tag{2.6}$$

The parameters i_0 (primary ionic current) and β (field factor) contain, among others, the density of the ionic species, the activation energy for hopping, the attempt frequency and the jump distance of ions [3, 89]. Due to the focus on high fields, the model is often referred to as a high-field model. It has been constantly developed over the years. Mott and Cabrera considered that the rate-limiting step is the injection of cations from the metal into the oxide [90]. The different approach leads ultimately to a similar exponential relation. The approach promoted the idea that only mobile metal cations contribute to oxide formation [3]. This was reasonable since the volume of oxygen ions is much bigger compared to metal cations. However, marker experiments show that the cation transfer number in TiO$_2$ is around 0.4 and approaches 0.5 for higher currents [3, 91]. Even though an unknown quantity of metal cations will dissolute and do not contribute to oxidation, the precise high field model should be modified to

$$i = i_{0,a} \exp\left(\beta_a F\right) + i_{0,c} \exp\left(\beta_c F\right) \tag{2.7}$$

with anion and cation contribution [3].

If the oxide is homogeneous, the field strength can be replaced by

$$F = \frac{\Delta E}{d(t)} \tag{2.8}$$

with the applied potential ΔE. For the sake of simplicity, only one ionic current contribution is considered, leading to

$$i = i_0 \exp\left(\beta \frac{\Delta E}{d(t)}\right). \tag{2.9}$$

This results in a complex differential equation for the growth rate from equation (2.5),

$$\frac{\mathrm{d}d}{\mathrm{d}t} = \frac{M}{\rho_o x z F} \cdot i_0 \exp\left(\beta \frac{\Delta E}{d(t)}\right). \tag{2.10}$$

The self-inhibiting character of the oxidation is apparent: An increasing thickness will exponentially decrease the growth rate (at a constant potential). The equation cannot be solved in a closed form [92]. However, an approximation gives

$$\frac{d_1}{d(t)} = A - B \ln(t), \tag{2.11}$$

with A and B being constants. This approximation is valid for $d(t) \ll d_1$ with $d1$ being typically about $10^{-8}\,\mathrm{m}$ up to $10^{-7}\,\mathrm{m}$ [90, 92]. So, for higher thicknesses a numerical approach might be necessary.

On a real titanium surface there will always be inhomogeneities (e.g., scratches, dislocations), which represent low resistance sites. If the charge transfer is concentrated at these sites, the true local current densities may drastically deviate from the apparent current densities [1]. Therefore, an inhomogeneous oxide thickness would be expected. However, if the current is predominantly constructive, the oxide layer at these points growths and the local currents diminish. The process repeats itself until a homogeneous dielectric oxide layer is formed with local thickness deviations of only a few percent.

2.1.4 Operation Mode

The most widely used DC operation modes to force oxide growth in an electrochemical cell are potentiostatic (constant current) and galvanostatic (constant potential) control. Fig. 2.3 illustrates the transients of the current density i, the applied potential E and the film thickness d along the processes.

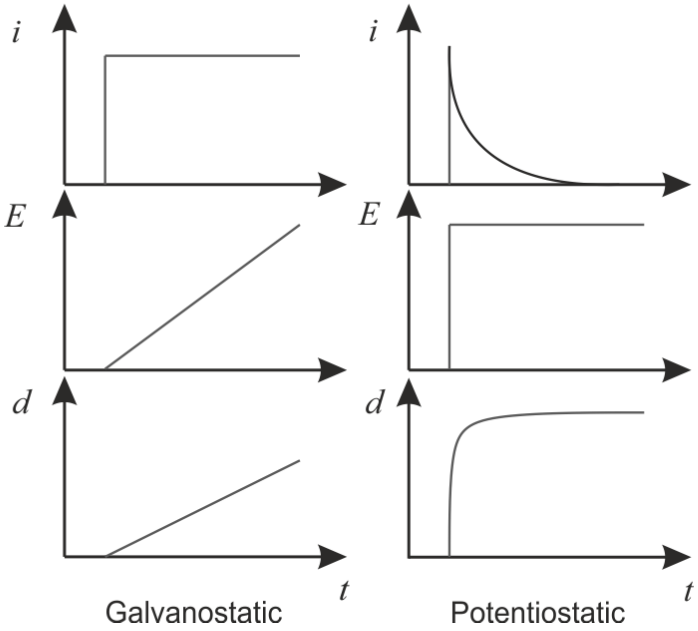

Figure 2.3: Schematic representation of the current density i, the applied potential E and the film thickness d during anodization, distinguished between potentiostatic and galvanostatic control.

With potentiostatic control, the current density starts with a maximum value immediately upon voltage application. According to (2.10), the thickness drastically increase in the first stage and changes only slightly after that. Current densities above $100\,\mathrm{Acm}^{-1}$ are conceivable and, thus, the oxide film is formed mostly in few milliseconds [3]. If the process continues, an aging of the oxide layer occur.

In contrast, under galvanostatic control the current density is kept constant. When the constructive current contribution i_{ox} is constant and no structural transformation in the oxide occur, the growth rate is constant according to (2.5). To obtain a constant growth rate, the field has to be constant as well. From this, it can be concluded that the thickness of the oxide layer is linear to the applied potential (relative to the necessary potential for oxidation),

$$d \sim k\Delta E \quad . \tag{2.12}$$

The coefficient k is sometimes referred to as formation coefficient or anodizing ratio. It can be determined by $k = \mathrm{d}d/\mathrm{d}E$ [1]. For TiO$_2$, results suggest that the formation coefficient k slightly increases with the temperature [3]. This is not surprising since the underlying mobility of ions increase with the temperature. In the case of potentiostatic control, a similar linearity to the applied voltage as in (2.12) can be observed if the anodization duration is kept constant [3].

2.2 Plasma Electrolytic Oxidation

So far, it has been assumed that the growth rate in a galvanostatic anodization is constant and thus the thickness is only limited by the maximum voltage. Prerequisite was the constant constructive ion current i_{ox}. However, at higher voltages the current contributions to the net current may change. The effect becomes apparent when the voltage transient deviates from the initial slope k, see the diagram in Figure 2.4a. One reason, is the increasing current contribution for anodic oxygen generation (above a certain potential, indicated with the line b in Fig. 2.1). Besides, the electronic current contribution may drastically increases at a higher voltage, often referred to as breakdown voltage U_{B}. Above U_{B}, the oxide lattice cannot withstand the local high field strength. As a result, so-called *dielectric breakdowns* occur. Dielectric breakdowns are characteristic for PEO and can range from inconspicuous repassivation to explosive dissolution or vaporization of the anodic surface [1]. They can be easily noticed during operation by irregular current peaks, visible sparks, potential fluctuations and audible noise [1]. Visible sparks origin from plasma states during dielectric breakdowns, which led to the term plasma electrolytic oxidation (PEO) for the technical process.

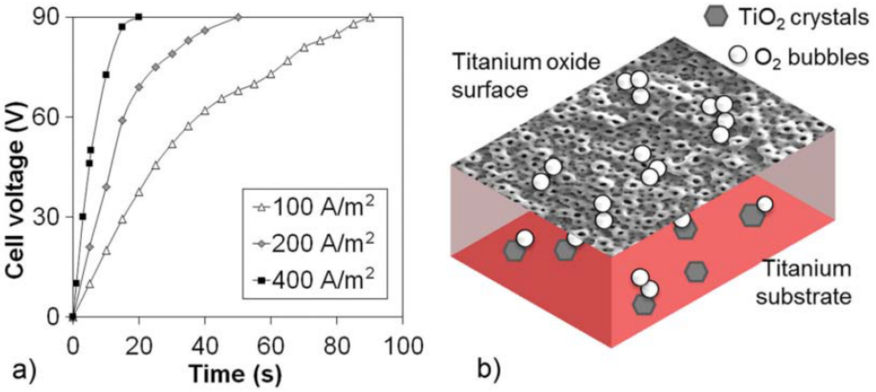

Figure 2.4: (**a**) Early cell voltage transients in a galvanostatic PEO process of titanium in 0.5M H$_2$SO$_4$ with different current densities. (**b**) Titanium oxide surface after PEO with characteristic sinkholes and indicated TiO$_2$ crystals. Experimental details can be found in [93]. Figure reprinted with permission from [4]. © (2014) Taylor Francis.

2.2.1 Dielectric Breakdowns

The term breakdown also applies for local destruction of the passive film by the attack of halide ions (localized corrosion) or by massive hydrogen evolution (layer lift-off) [87]. Dielectric breakdowns resemble a short circuit of a dielectric layer. In a PEO process, the dielectric breakdowns substantially shape the oxide layer. While the effects of dielectric breakdowns are often easy to observe, it can be difficult to determine their origin.

It is assumed that inhomogeneities in the bulk or at the interface electrolyte/oxide represent local flaws in the passive film and therefore serve as nucleation points for dielectric breakdowns [87, 89]. Possible flaws can be impurities in the local composition, defects (e.g., grain boundaries, dislocations, inclusions) or localized stress states [4, 89]. When the applied potential reaches a critical value, the local field strength at these sites is sufficient to induce an electron avalanche process [94]. The corresponding voltage is referred to as breakdown voltage U_B. The very initial step of the avalanche effect is either an ionic or electronic injection. Ikonopisov promoted the avalanche model and proposed that electrons are injected to the oxide conduction band from electrochemical reactions at the oxide/electrolyte interface [3, 94]. Albella et. al supported the avalanche model as well, but concluded from systematic studies with different concentrations of electrolyte that the electrolyte species incorporate at first and only then electrons are injected [95].
The primary electrons accelerate in the field and their energy must be higher than $3/2E_\mathrm{G}$ for breaking down the oxide, where E_G represents the band gap [96]. The electron energy is sufficient for ionizing the atoms, which will lead to new electrons. When the density of free electrons reaches a critical value, a discharge channel of plasma between electrolyte and substrate is formed. In the center of the channel, the material is partially ionized and almost completely atomized. In the electrical field, cations move outwards, and anions move inwards towards the anode. However, compared to the electrons the remaining ions are almost immobile and practically create a stationary charge, which decelerates electrons [96]. The charge exchange is mainly due to electrons and represents high current values in the experiment. Local temperatures in the channel can reach up to 10^3–$10^4\,\mathrm{K}$ and are accompanied with high pressures up to $10^2\,\mathrm{MPa}$ [97]. The temperature drops towards the channel walls and changes in the course of the discharge. The conditions in the channel induce a quick melting of material at the walls and explosion-like ejection of its vapors. Thus, the channel expands spatially. Light emission notably occurs and originate from optical transitions of electrons in the plasma, but are only a minor side effect in terms of energy consumption [98]. Analysis of light emissions reveal essential features of the process and are discussed in the section 2.2.2.

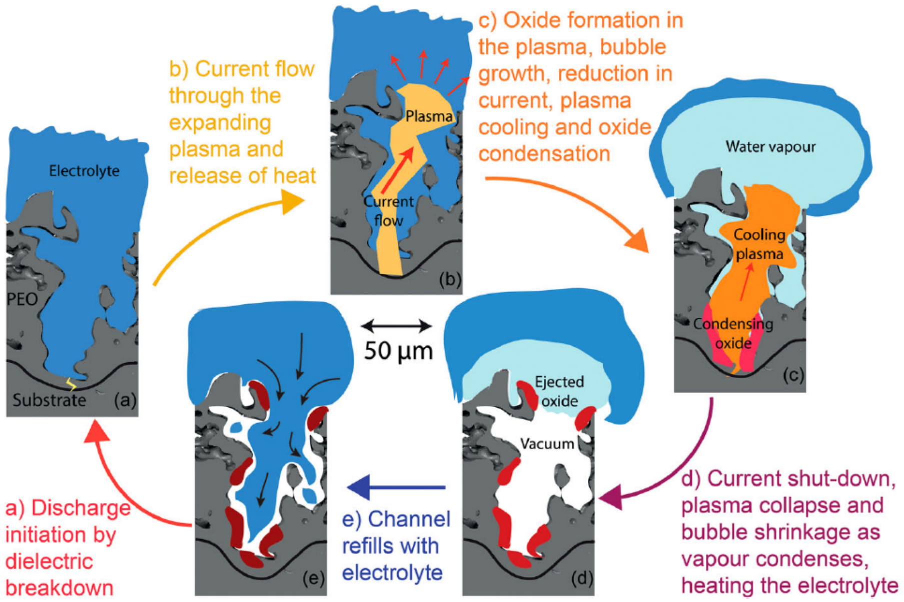

Figure 2.5: The lifetime of an individual discharge in a PEO process is presented in schematic sections through a pore. Figure reprinted under the terms of the Creative Commons CC BY license from [16].

Termination

The lifetime of an individual discharge is self-limited, illustrated in Fig. 2.5. Otherwise, only a few plasma channels would be sufficient for charge compensation, so that no further channels would be formed. The origin for the termination is assumed to be the thermal expansion of the channel, which leads to a reduced density of particles. In the beginning of expansion, the reduced density can be compensated by adjacent particles evaporating from the walls of the channel [96]. When the expansion continues, the density decreases, and the conductivity of the channel diminishes. Simultaneously, the temperature decreases. The thermal mass from the substrate enables a rapid cooling of the plasma at the bottom of the channel [99]. Starting from the bottom and the walls of the channel, the particles in the extinguishing plasma are able to form metal oxide. Since the oxide formation is exothermic, the reaction slows the cooling [96]. This is the main reason, why the discharge lifetime is at least two orders of magnitude higher compared with the ordinary electron avalanche [100]. When the plasma continues to cool down, the oxide condenses, settles down at the walls or is ejected from the channel. Parallel, gases at the top of the channel accumulate and form a growing ‚bubble‘, mainly consisting of water vapor and oxygen. The ‚bubble‘ is sometimes referred to as vapor-gas phase in pores (VGPP) [100]. The reduced conductivity in the gas phase will shut down the plasma rather abruptly [16, 98]. Finally, the bubble shrinkages as vapor escapes or condense. Subsequently, the remaining cavity in the discharge channel fills with the electrolyte. When the channel is completely filled, it can be reused for discharges.
The deep pore and relatively small layer of oxide at the bottom of the extinguished channel, presents a rather small resistance and is a favored nucleation point for new

discharges. However, the time for refilling the channel with electrolyte can be considered as incubation time, in which no discharges in the channel take place. The incubation time for a new discharge in a pore were determined to 0.1–1 ms [16]. In the course of the process, the incubation time tends to increase [101]. The reason for this can be assigned to the increasing oxide thickness, which means that the electrolyte takes longer to fill the channel. The filled channel can provide a preferred injection point for a new discharge.

Cascades

An important feature of PEO is that these discharges typically occur in prolonged sequences, also referred to as cascades. The total size of a cascade is estimated to be in the order of 100–1000 individual discharges [16, 102]. Individual discharges are complicated to distinguish. Recent studies with real-time imaging (see section 2.2.2) indicate a lifetime of an individual discharge in the order of 300µs, while cascades can last up to a second or more [16]. Cascades occur in a spatially limited area or slowly move along the surface. An analysis of a cascade during a PEO of titanium (55 mA/cm^2, 12.9 mol/l H_2SO_4, recorded at 70 C/cm^2) determined the propagation rate to approximately 1.6 mm^2/s [103]. One reason for the slow movement of cascades is assumed to be the high temperature induction of individual discharges. When the original plasma extinguishes, the remaining high temperature promote the formation of a new plasma channel in adjacent regions. As a result, cascades are slowly moving along the surface, which is visually accessible.

Oxide Reformation

Dielectric breakdowns are partially destructive, which is apparent at the surface by formed sinkholes, exemplified in Fig. 2.4b. In contrast, the destructive effect on the substrate are not immediately apparent. Strong discharges progressively consume the substrate, which is evaporated into plasma. Thus, the interface moves progressively downwards relative to the initial titanium surface [16, 104]. When the plasma extinguishes, evaporated substrate partially react with oxygen. The oxide may condense on the bottom or the walls of the channel. It is also partially ejected from the channel and deposits on the oxide surface like a volcanic crater. Subsequently, the oxide solidify. Therefore, the total thickness of the porous coating increases. The conversion character and the growth of the porous layer during PEO is schematically shown in Fig. 2.6. Especially in late stages of PEO, a physical loss of oxide or substrate material is possible due to strong cascades. The amount of substrate material in the electrolyte can be determined by subsequent solution analysis [105]. In addition, the high pressures can cause cracks in the coating, which can be identified on the surface by various analysis techniques [99].

In conventional anodization the maximum voltage is a simple indicator for the coating thickness. However, in PEO a porous coating is formed. The charge exchange is mainly accomplished by discharges, which reoccur preferentially at the bottom

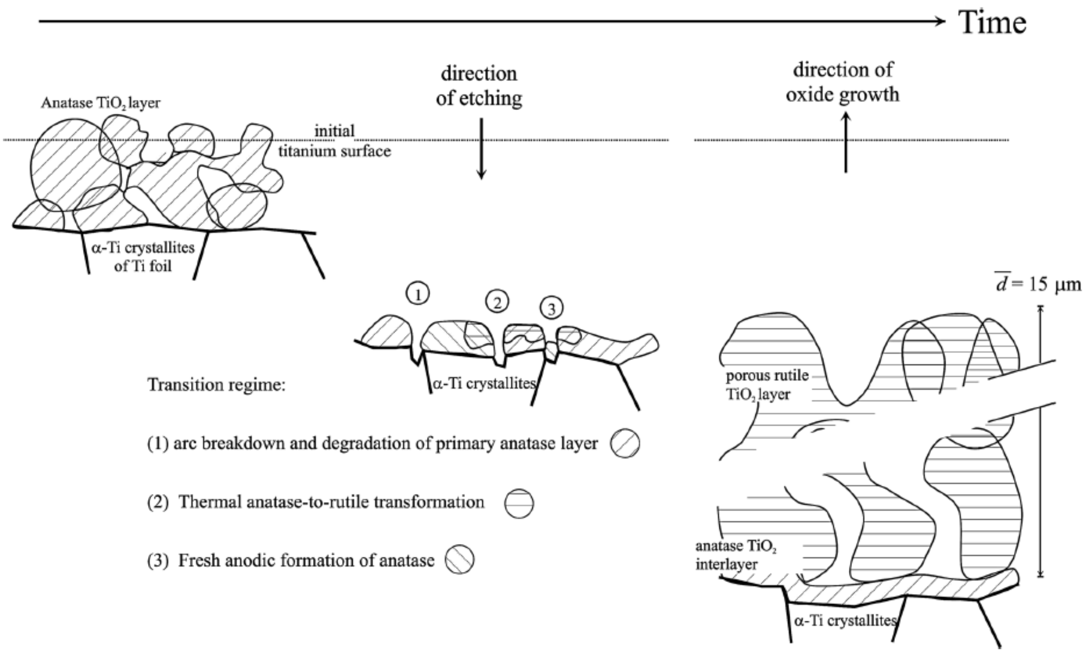

Figure 2.6: Schematic illustration of the oxide forming during PEO in etching media. Emphasized is the characteristic phase development and distribution, with anatase in a compact layer near the substrate and rutile dominating in the upper porous layer. Figure reprinted with permission from [104]. © (2014) Springer Nature.

of pores (see step (a) in Fig. 2.5). Therefore, the maximum voltage indicates the thickness (or to be more precise, the resistance) at the bottom of the pores. Experimental results show that the voltage required to maintain the constant current during galvanostatic PEO, increases with the time. It can be concluded that the compact thin layer adjacent to the bottoms of the pores, growth in the process. Hereby, a change in the oxide conductivity due to any change in morphology is neglected. Numerous studies confirm the existence of a compact layer and its growth during PEO of titanium [106–109]. Further studies used impedance data and equivalent circuit models to confirm its dominating contribution to the overall resistance of the coating [110, 111].

When considering the growth of the oxide, it should be noted that the conventional oxide growth by ion migration also promotes the oxide formation during PEO. Its contribution will decrease in the process with the increasing number of dielectric discharges but does not completely vanishes. This aspect will be dealt with in the second publication of this thesis (see section P.II).

Crystallization and Phase Transformation

The titanium substrate for PEO is often amorphous or contains a polycrystalline fraction of the hexagonal α-Ti phase. At moderate temperatures, the initial oxide film on titanium is amorphous [112]. In the course of the PEO process, crystallization and phase transitions occur. Hereby, the substrate, the temperature and the electrolyte have a major impact on the morphology. The growth of the TiO$_2$ crystallites starts early in the process, e.g., in the stage of conventional anodization [112]. First, isolated TiO$_2$ crystallites with an average size of a few nm evolve in the amorphous oxide [3]. The initial crystalline phase is generally anatase. This can be rationalized by the less-constrained molecular ordered anatase structure in comparison to rutile (see section 1.3). Although some studies report the presence of rutile before the occurrence of breakdowns, it is generally accepted that the anatase/rutile transformation is largely controlled by breakdowns [3]. Hanaor and Sorrell summarized typical transformation temperatures in air for bulk anatase to rutile to 400–1200 °C [50]. When compared with typical temperatures during dielectric breakdowns, it is evident that the temperature during PEO is sufficient for the irreversible phase transformation from anatase to rutile. Therefore, a high number of discharges results in a dominant fraction of rutile. Friedemann et al. reported a rutile crystallinity of approximately 95% after PEO of titanium (in 1.5 mol/l sulphuric acid with and voltages up to 220 V) [113].

Despite the dominating rutile fraction in PEO produced TiO$_2$ coatings, several investigations indicate that the compact layer consists mainly of nanocrystalline anatase [104, 106, 109]. For once, this can be due to the constant contribution of conventional anodic growth at the bottom of the pores, which favors the formation of anatase. However, the transformation to rutile seems also to be inhibited in the compact layer. This can be understood, when respecting the high thermal mass of the substrate, which means that the temperature in the immediate vicinity of the substrate equalize rapidly. Therefore, the phase transformation is kinetically inhibited. A typical layer composition and their crystalline TiO$_2$ phases are summarized in Fig. 2.6. The phase composition of PEO produced TiO$_2$ coatings is further discussed and quantified with the distinction of the compact and porous layer in the publications P.I and P.II.

Electrolyte

The most important process parameters in PEO are the substrate material, the parameters for the electrical supply and the composition of the electrolyte. Compared to the former, the influence of the electrolyte is less well understood. Many of the findings in this area are empirical ones, and the complexity of the PEO process makes it difficult to draw consistent conclusions.

The electrolyte acts primarily as an ionic conductor, which provides charge carriers for the anodic reaction. In conventional anodization and PEO, acid and alkaline electrolytes are commonly used. The demands on an electrolyte may vary in both cases. In conventional anodization, the growth is controlled by lattice diffusion, while in PEO the oxide growth takes place when the plasma collapse and cools down [16]. With the focus on PEO, the influence of the electrolyte on breakdowns will be primarily discussed in the following.

The beginning of dielectric breakdowns indicate the transition from conventional anodization to PEO. In terms of the applied potential, it is often defined by the breakdown voltage U_B (sometimes also referred to as ignition voltage). U_B can also be used as a good indicator of how readily breakdowns occur. Naturally, U_B depends on the substrate material and approximately correlates with the band gap of the oxide [94, 96]. From empirical results U_B was related to the electrolyte conductivity κ,

$$U_\mathrm{B} = a_\mathrm{B} + b_\mathrm{B} \log{(1/\kappa)}, \tag{2.13}$$

where a_B and b_B are constant values for a given metal and electrolyte composition [94, 114]. It is assumed that an increased conductivity facilitates electrolytic electron donation and subsequent injection into the oxide conduction band.

Since the conductivity and the concentration of the electrolyte are closely related, a concentration dependency is found as well. In general, the conductivity of aqueous electrolytes increases with the concentration up to a certain value. Above it, the conductivity decreases due to inter-ionic interactions. Therefore, discharges should start later as the concentration continues to increase above the certain value. If this tendency is transferred to the overall process, less impact of discharges can be expected. However, results from the first publication in this thesis P.I indicate, that the impact of discharges during PEO of titanium in sulphuric acid do not decrease (above the certain concentration). Another deviation to the conductivity relation in equation 2.13, is reported by Simchen et al. [115]. They showed that the change in electrolyte conductivity between 30–210 mS/cm^2 has no relevant influence on the breakdown voltage. These results suggests that a mere consideration of conductivity is not sufficient for a comprehensive description.

A more fundamental approach focuses on the electron injection ability of an electrolyte. Herein, the nature and the concentration of anions at the oxide surface are essential for initiating dielectric breakdowns [111, 115]. Both parameters are highly difficult to determine. The nature of the anions can imply basic properties as the molecular charge or the ionic size. To understand the dependence on the concentration, the concept of the electrical double layer in Fig. 2.7 can be used. An electrical double layer at the interface is assumed to impede electron injection. From studies on conventional oxidation, it is assumed that the spatial width of the double layer decrease with the anion concentration and therefore decrease the forming voltage [116]. In principle, this should also affect the electron injection ability for initiating dielectric breakdowns.

The electron injection ability goes along with another macroscopic effect in electrolytes: The electrolyte's activity to dissolve the anodic oxide material is closely related to the electron transfer ability [116]. The dissolution can also create inhomogeneities, which present preferred nucleation points for dielectric discharges. Indications for this can be found in the first and second publications of this thesis (see section P.I and P.II).

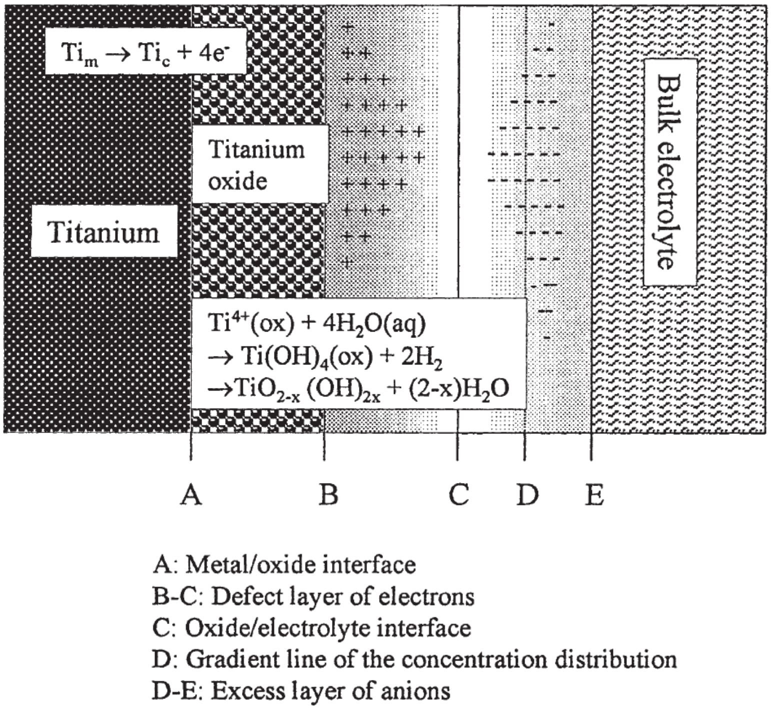

Figure 2.7: A sketch of the electrical double layer at the titanium oxide/electrolyte interface. Figure reprinted with permission from [116]. (2001) © Elsevier.

2.2.2 Insights into PEO

To provide a more detailed picture of the PEO process, results from a variety of investigation methods are presented in the following section. The focus is on titanium, although few results come from studies on aluminum. In general, the investigation of PEO can be performed during or after the process. Both options are often combined and complement each other to provide a complete picture. Table 2.1 lists several common methods. In the following, we take a closer look at some methods, which can be performed during PEO. Methods for the analysis of titanium samples after PEO are presented and discussed in detail in the studies P.I and P.II.

During PEO	After PEO
Optical Emission Spectroscopy (OES)	**Scanning Electron microscopy**
Electrical Monitoring	(In-situ) Impedance Spectroscopy
Acoustic Emission Analysis	**(Confocal) Raman Spectroscopy**
Real-time imaging	Glow Discharge OES
	Energy-Dispersive X-ray Spectroscopy
	X-ray Diffraction
	X-ray Spectroscopy

Table 2.1: A selection of common methods to study the oxide formation in PEO, differentiated into measurements performed during and after PEO. Techniques written in bold letters were used in the present work.

Electrical Monitoring

Voltage-time diagrams are a convenient way to receive fundamental information about the galvanostatic PEO process. Fig. 2.8 (a) shows typical voltage transients for different current densities from PEO of titanium. The final voltage is between 120–130 V. A plot of the voltage against the transferred charge density can be used to compare different current densities. The right diagram in Fig. 2.8 (a) indicate, that the variation in the current density has a minor impact on the voltage when referred to the charge density instead of the time. In fact, SEM images in Fig. 2.8 indicate that the surface structure of each sample is very similar, as long as the transferred charge density is comparable. The crystallographic ratios between anatase and rutile (determined by XRD analysis, exactly as in [108]) are also very similar (68±5% anatase) and therefore reinforce the assumption that the oxide formation under the given conditions is independent of small deviations in the current density.

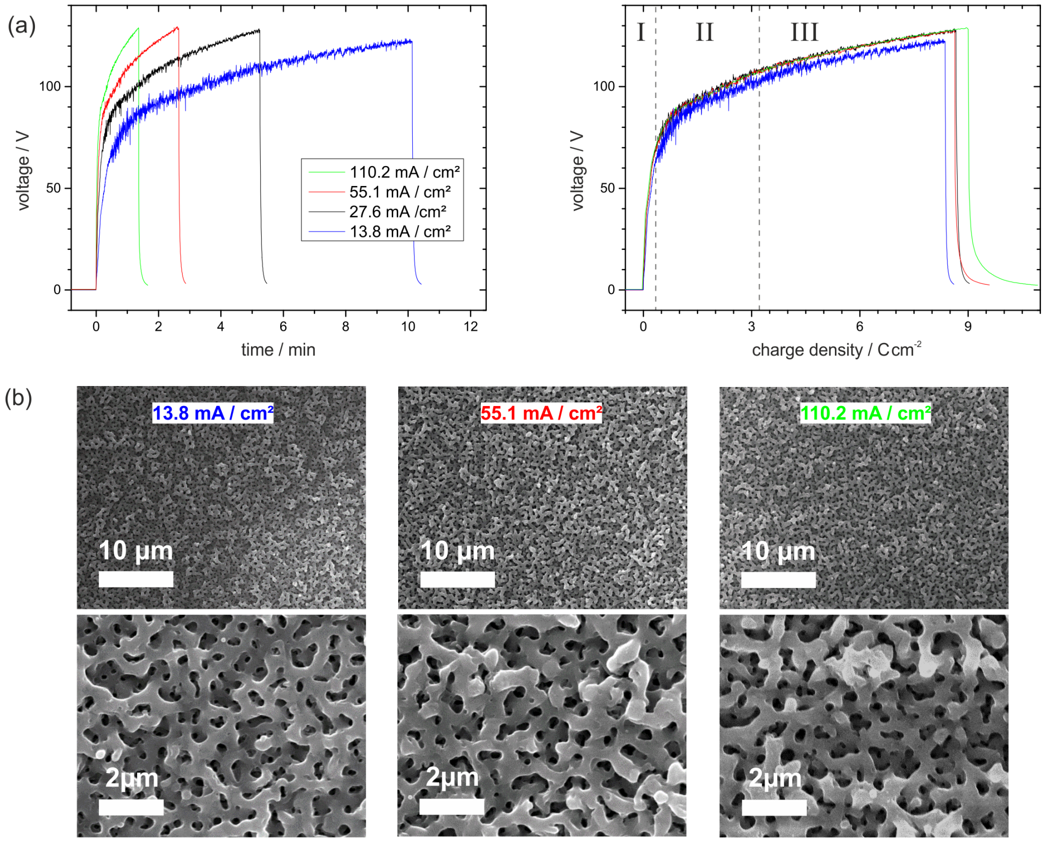

Figure 2.8: (**a**) On the left side, recorded voltage transients of an galvanostatic PEO process with different current densities are shown. On the right side, the voltage signal was plotted versus the charge density and demonstrates the low impact of the difference in current densities on the curves. In addition, characteristic stages of the PEO process are indicated. (**b**) Scanning electron microscopy images of the corresponding surfaces after a charge transfer of approximately 9 C/cm^{-2} show no significant differences in the surface morphology (secondary electron imaging mode; for experimental details see [99]).

The voltage curves are often divided into three (or even four stages) [97, 110, 117, 118]. The first stage represents a conventional anodizing process. Therefore, the formation coefficient k is constant. The second stage arise just above the breakdown voltage U_B. The beginning can be roughly estimated by an inflection point in the curve. In this stage, a large number of small dielectric breakdowns occur. The formation coefficient k changes drastically. After the second stage, the voltage curve reaches a constant slope, which is the third stage in the process. The transition is less pronounced compared to the former transition. In the third stage, cascades become larger, more intense and their color changes progressively from white to yellow. The cascades are sometimes called microdischarges and, in accordance with this, the stage is also known as microarc stage [110, 119]. The fourth stage is often defined by a constant cell voltage and is not shown within the plot in Fig. 2.8 (a). The discharges are even stronger compared to stage three, which can be recognized by the increasing voltage fluctuations [118]. If the process continues, sequences of detrimental discharges occur more frequently and their distribution on the surface becomes increasingly inhomogeneous. Due to the partial destruction of the coating, the voltage drops abruptly [14]. This critical event should be avoided in order to maintain an intact passivation layer. In practice, the precise assignment of individual stages is challenging. Especially since a small change in the process parameters can produce a significant change for the oxide formation and, as a consequence, for the voltage-time diagrams.

Real-time Imaging

As mentioned before, individual discharges and cascades change in the course of the process. The change can be optically inspected by real-time images. In this way, Matykina et al. determined the size and lifetime of microdischarges from stage four to 70–380 µm and 35–800 ms [120]. Hereby, the PEO of titanium was performed in orthophosphate at 20 mA/cm^2. Furthermore, it was reported that the average lifetime of microdischarges increase in the course of the process [120]. However, the frame interval of 40 ms induce a high uncertainty of 35 ms. Therefore, it is assumed that individual discharges could not be resolved.
A recent study from Troughton et al. investigated the PEO of a small area aluminum sample (AA2014; Al $>$ 93%) by combined high speed electrical monitoring and video photography [102]. The frame interval was about 5.1 µs. The individual discharge lifetimes were approximately 300 µs and the individual currents around 100 mA. A comparison study between Al, Mg, Ti and Ta indicate that the lifetimes of individual discharges on Ti and Ta are even less in comparison with Al and Mg [16]. The authors assume, that "electron flow through the oxide layer was taking place more readily with Ti and Ta, inhibiting the development of high electric fields across the oxide and hence of large, well-defined discharges" [16].

Several studies with real-time imaging revealed that during PEO the size of cascades becomes larger during the process, while the number of cascades is reduced [121]. This was confirmed during PEO of titanium in sodium metasilicate at 200 mA/cm^2 by Stojadinovic et al. [122]. This tendency for larger and longer microdischarges in later stages of PEO, could also be qualitatively confirmed in our own real-time imaging studies on PEO of titanium in different concentrations of sulphuric acid at 55 mA/cm^2 [103]. Some of the results are shown in Fig. 2.9.

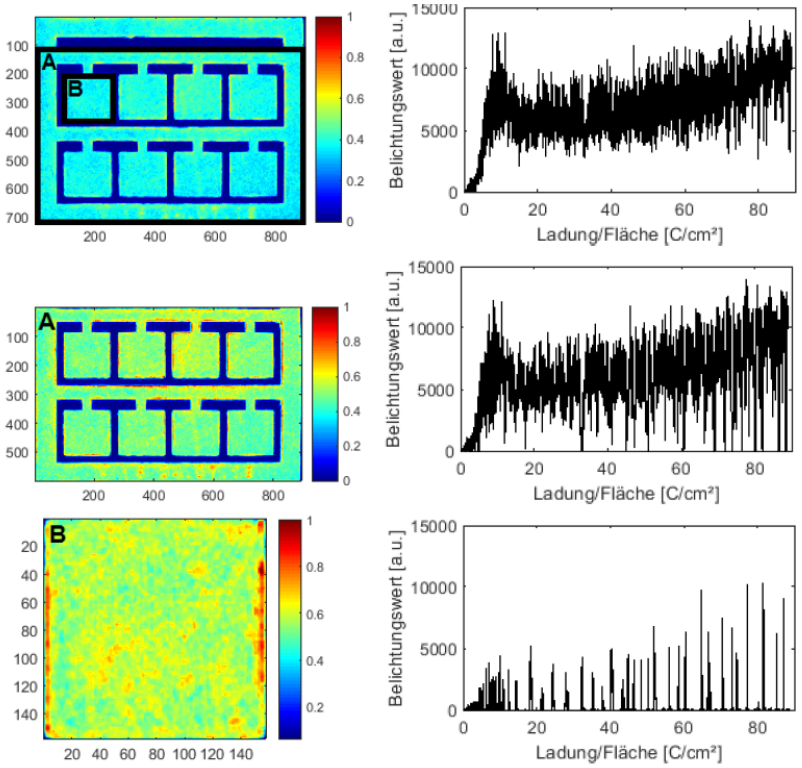

Figure 2.9: (**a**) Spatial distribution of time-integrated discharges in a relative color scale during a PEO of titanium in 12.9 mol/l at 55 mA/cm^2. The final charge density was around 89 C/cm^2. (**b**) Integrated luminescence intensity over the corresponding areas in relation to the charge density during the PEO process. Figure reprinted with permission from [103].

The right column in Fig. 2.9 shows the integrated emission intensity over the corresponding sample area, indicated in the left column. A tendency for an increasing light emission during PEO is apparent. The spatial distribution of discharges on the area is visualized with the colored sample areas on the left. Especially, on the small image section (B) with 3×3 mm^2 a slight non-homogeneity of the discharge distribution can be determined. Similar results were obtained in an AC PEO of aluminum (AA2214; Al $>$ 93%) in an electrolytic solution of KOH and Na_2SiO_3 diluted in water [123, 124]. Hereby, the growth rate and the roughness were found to be higher at the edges than at the center of the samples. In this context, a recent study also investigated the n-type semiconductor properties of PEO aluminum (AA1060; Al $>$ 99.6%). The Schottky-Mott analysis revealed that the carrier density at the edge of the specimen is lower compared to the central region [125]. This edge effect is assigned to an unevenly distributed electrical field strength and applies regardless of the substrate material (although the degree of impact may vary). Simulations revealed that the field strength at the specimen edge region is nearly two times higher than at at the specimen center [125]. Thus, the geometry of the sample is crucial for the homogeneity of the coating. Likewise, the distance and geometry of the counter electrode are relevant parameters and can be adjusted to achieve the desired homogeneity [123].

Overall, with the results of real-time imaging, the life cycle in Fig. 2.5 can be quantified in time and space. However, the intensity and origin of the discharges cannot be determined.

Optical Emission Spectroscopy

A powerful in situ technique to study the nature of discharges during PEO is the optical emission spectroscopy (OES). By analyzing the spectral distribution of discharges, characteristic electron transitions are revealed. The intensities can be used to estimate the temperature and the electron density in the plasma. In this way, Dunleavy et al. investigated PEO of an aluminum alloy (AA6082; Al $> 95\%$) and estimated the temperature in the core of the plasma channel to approximately $16,000 \pm 3,500\,\mathrm{K}$, while the corresponding electron density was about $N_e \approx 5 \times 10^{17}\,\mathrm{cm}^{-3}$ [126]. Outside the core, the temperatures (T ≈ 3,000–4,000 K) and the density ($N_e \approx 10^{15}\,\mathrm{cm}^{-3}$) is significantly lower [126]. Another spectroscopic study from Hussein et al. on a commercially pure aluminum alloy (AA1100; Al $> 99\%$) recorded the temperature along an galvanostatic PEO process, shown in Fig. 2.10 (a) [117]. For a current density of $0.15\,\mathrm{A/cm^2}$, the temperature ranges from 4,500±450 K to 10,000±1,000 K. The higher value was attributed to sporadic strong discharges, while the lower value is found at the beginning of the process and then settles at a mean value of ≈ 4,800 K. According to Hussein et al. [117] and earlier reports by Yerokhin et al. [121] three types of discharges can be distinguished, summarized in Fig. 2.10 (b):

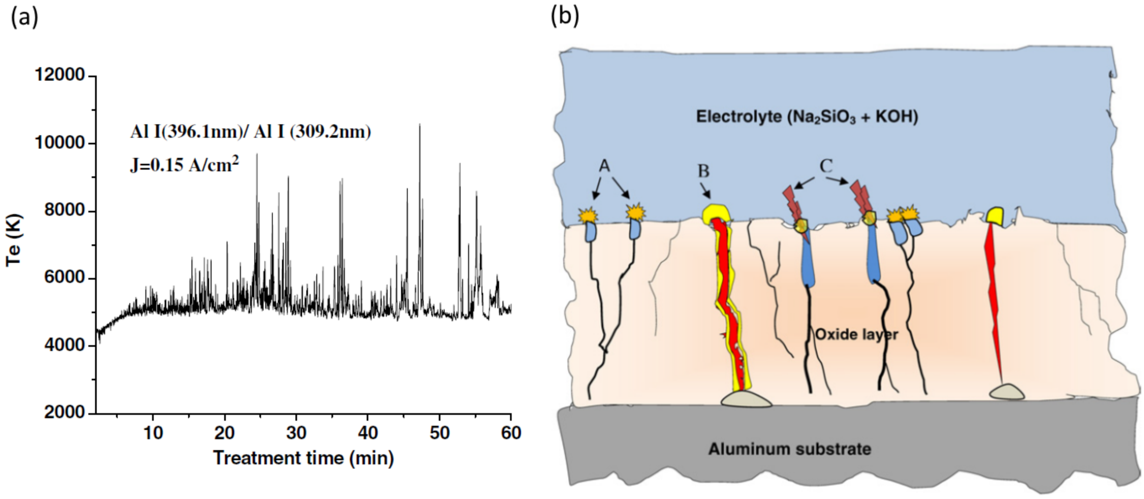

Figure 2.10: (**a**) Plasma temperature in dependence of the process time during PEO of aluminum in a solution of Na_2SiO_3 plus KOH (pH=12). The temperature was derived from the intensity ratio of Al (396.1 nm) and Al (309.2 nm), which were determined by OES. (**b**) Illustration of three different discharges on oxidized aluminum. Figures reprinted with permission from [117]. © (2010) IOS Publishing.

Discharges occur at the metal/oxide interface (type B) and at the oxide/electrolyte interface at either in relatively small holes near the surface (type A) or in micropores at the bottom of the oxide layer (type C). The latter two origin in gas discharges, which are initiated by dielectric breakdowns. They are relatively weak and form the baseline of the temperature transient in Fig. 2.10 (a). The discharge type B represents the dielectric breakdown in a strong electric field. This type of discharge induces the high temperature peaks and is substantially involved in the reforming of the oxide layer. The contribution of electrode and electrolyte elements to the optical emission spectrum is used to distinguish between discharge type B and type A or C. The high temperatures of type B discharges lead to the vaporization of aluminum and magnesium as anode material, which can be derived by the intensity of the characteristic emission lines in the spectrum [97]. The evaporation of aluminum (T_m=933 K) and magnesium (T_m=1941 K) is observed regardless of the applied electrolyte. For metals with higher melting point T_m, e.g., titanium (T_m=1941 K) and tantalum (T_m=3290 K), the evaporation is less pronounced and depends sensitively on the type of electrolyte [97, 122]. Stojadinovic et al. characterized the PEO of titanium (in sodium metasilicate, 10 g/ l $Na_2SiO_3 \cdot 5\,H_2O$, at 200 mA/cm^2) using real time imaging and optical emission spectroscopy [122]. According to their results, the electron density ranges from $3.5 \times 10^{15}\,\mathrm{cm}^{-3}$ to $4.5 \times 10^{16}\,\mathrm{cm}^{-3}$ and the electron plasma temperature is about 3,700±500 K, which is estimated from the line intensity ratios of Ti emissions.

In the course of this work, OES during galvanostatic PEO of titanium with 7 M or 12.9 M H_2SO_4 were performed. A high performance fiber optic cooled spectrometer (SILVER-Nova, StellarNet Inc., Tampa, FL, USA) with an applied fiber optic of 1,400 µm net diameter (7×200 µm core fibers, BFL200HS02, Thorlabs Inc., Newton, NJ, USA) has been used to obtain OES spectra. However, different experimental configurations always led to continuous spectra without characteristic emission lines. It is assumed that dissipative scattering in the highly concentrated electrolyte leads to a strong broadening of discrete emissions. Due to the strong etching in the medium and the high voltages applied during PEO, the distance of the fiber and the sample cannot be reduced freely. Thus, an valuable OES during the PEO of titanium in H_2SO_4 is only conceivable in reduced electrolyte concentrations.

P.I Combined Galvanostatic and Potentiostatic Plasma Electrolytic Oxidation of Titanium in Different Concentrations of H_2SO_4

Publication Reference

[108]:

B. Engelkamp, M. El Achhab, B. Fischer, Ü. Kökcam-Demir and K. Schierbaum, *Combined Galvanostatic and Potentiostatic Plasma Electrolytic Oxidation of Titanium in Different Concentrations of H_2SO_4*, Metals **2018**, 8(6), 386.
doi:10.3390/met8060386

Copyright statement

Author Contributions

B.E., M.E., K.S. and B.F. conceived and designed the experiments; B.E. and B.F. performed the experiments; B.E. analyzed the data; B.E., M.E., K.S., B.F. and Ü.K.-D. contributed reagents/materials/analysis tools; B.E. wrote the paper.

metals

Article

Combined Galvanostatic and Potentiostatic Plasma Electrolytic Oxidation of Titanium in Different Concentrations of H_2SO_4

Bernd Engelkamp [1,*], **Mhamed El Achhab** [1], **Björn Fischer** [2], **Ülkü Kökçam-Demir** [3] and **Klaus Schierbaum** [1]

[1] Abteilung für Materialwissenschaft, Institut für Experimentelle Physik der kondensierten Materie, Heinrich-Heine-Universität Düsseldorf, Universitätsstraße 1, 40225 Düsseldorf, Germany; mhamed.elachhab@hhu.de (M.E.A); klaus.schierbaum@hhu.de (K.S.)
[2] Institut für Pharmazeutische Technologie und Biopharmazie, Heinrich-Heine-Universität Düsseldorf, Universitätsstraße 1, 40225 Düsseldorf, Germany; bjoern.fischer@hhu.de
[3] Abteilung für Bioanorganische Chemie, Institut für Anorganische Chemie und Strukturchemie I, Heinrich-Heine-Universität Düsseldorf, Universitätsstraße 1, 40225 Düsseldorf, Germany; uelkue.koekcam@hhu.de
* Correspondence: bernd.engelkamp@hhu.de; Tel.: +49-211-81-15256

Received: 29 April 2018; Accepted: 21 May 2018; Published: 26 May 2018

Abstract: We report on plasma electrolytic oxidation of titanium, employing a technique with combined potentiostatic and galvanostatic control. The effect of different H_2SO_4 electrolyte concentrations on the titanium oxide formation was studied sytematically. The titanium oxide consisted of two distinguishable layers. The upper layer is porous, up to few micrometers thick and primarily rutile, while the interlayer is compact, comparatively thin and is associated to anatase formation. The electrolyte concentration changed substantially layer thickness, porosity and phase composition, as deduced from scanning electron microscopy, X-ray diffraction and Raman spectroscopy.

Keywords: titanium dioxide; plasma electrolytic oxidation (PEO)

---

1. Introduction

Microstructured oxide layers on titanium, produced by plasma electrolytic oxidation (PEO), are of great interest for various applications, including bioengineering, architecture, photovoltaic and sensing technology [1,2]. In gas sensors, PEO films on titanium exhibit a number of interesting properties. For example, after coating them with graphite or graphite/catalysts mixtures, various gases can be detected at room temperature with high sensitivity [3–6]. Galvanostatic, potentiostatic and potentiodynamic operating modes are commonly applied [7] and have been compared with respect to surface morphology, phase composition and electrical properties [8]. Sulphuric acid is frequently used and yields porous oxide layer of certain thickness under PEO conditions [9–13]. Furthermore, previous studies also confirm the growth of a compact interlayer at the metal substrate which is thin compared to the porous layer [8,14,15]. Growth models for lightweight metals have been proposed which explain the relevant structure-determining processes and correlate them with the key influence factors, including electrolyte composition, electrical process parameters, process temperature, oxidation time and additives [16,17]. In most studies, a low electrolyte concentration is used which is often below 2 M. Our process employed an exceptionally high concentration of sulphuric acid of 12.9 M as well as a combination of galvanostatic and potentiostatic PEO. This leads to a remarkable good adhesion, well controlled microstructure and phase composition [18]. In this study, we present the special PEO operation mode and discuss the impact of different H_2SO_4 electrolyte concentrations on the resulting oxide layers. To determine the microstructure of the surfaces and cross-sections, we used scanning electron microscopy (SEM). The phase composition was investigated quantitatively with two different techniques, i.e., X-ray diffraction (XRD) and Raman spectroscopy.

2. Materials and Methods

Samples (surface area approx. 1990 mm^2) were cutted from titanium foil (thermally annealed, 99.6% purity; 125 µm thickness) by means of a laser (PowerLine F30, ROFIN-SINAR Laser GmbH, Hamburg, Germany). It is cleaned ultrasonically in acetone and in deionized water, each for approximately 15 min.

The electrolytic cell consists of a glass vessel with integrated glass shell, which enables temperature regulation of the electrolyte by pumping cold water through the shell. The water temperature is kept constant at 15 °C with a recirculating cooler (FL1201, JULABO GmbH, Seelbach, Germany). The reaction chamber is filled with 150 mL H_2SO_4. The concentration varied from 0.5 M up to 12.9 M (which corresponds to 3 wt. % up to 75 wt. % H_2SO_4, respectively). A magnetic stirrer is utilized to prevent spatial temperature differences in the electrolyte and also to reduce disturbing gas accumulations on the electrode surfaces. The electrolytic system was completed by the titanium sample as anode and a graphite rod as cathode (area of immersion 3180 ± 120 cm^2) at a distance of 23 ± 4 mm. The current in the cell was permanently limited to $I_{\mathrm{max}} = 200\mathrm{mA}$. The voltage V was gradually increased in defined time intervals up to 145 V by a highly stable current power supply (FUG MCP 350-350). The voltage steps were achieved by adjusting the voltage limitation V_{lim}. This means, when I_{max} is reached, V is automatically regulated to a value smaller than or equal to V_{lim}. Voltage and current were adjusted and recorded in 250 ms intervals using an in-house developed LabVIEW program. After treatment the sample was rinsed in deionized water and dried in air.

The microstructure of the oxide layer has been investigated by field emission scanning electron microscopy (Merlin FE-SEM, Zeiss Microscopy GmbH, Jena, Germany). Surface images of secondary electrons were done with 5 kV excitation and at a tilt angle of 38°. Cross-sections were prepared by argon ion milling (Cross Section Polisher SM-09010, JEOL Ltd., Tokyo, Japan). For cross-section images, backscattered electrons were collected with 10 kV at 0° tilt angle. The phase composition was determined by X-ray diffraction (XRD). Diffraction data were collected on a Bruker D2 Phaser diffractometer with Cu-Kα radiation (λ = 1.54184 Å, 30 kV, 10 mA) in Bragg-Brentano geometry and LYNXEYE 1D-detector. XRD patterns were measured with a flat silicon, low background rotating sample holder (5.0 min^{-1}) in 10 min duration between $20° < 2\theta < 45°$ with a scan speed of 1 s/step and a step size of approximately 0.05° per step.

Raman spectra were collected by using a self-built Raman microscope. Samples were excited with a solid-state Nd:YVO_4 laser (Newport Corp., Irvine, CA, USA, Millennia Pro 2 s, wavelength of 532 nm). A Nikon Instruments 100× microscope objective (Nikon, Tokyo, Japan) was used to focus the laser excitation light, delivering in the sample plane a power of 3.2 mW. The spot size was about 2–3 µm in diameter. The Raman scattered light was collected by the objective and was then diffracted by a monochromator (Kaiser Optical Systems, HoloSpec, Ann Arbor, MI, USA, slit width of 50 µm) equipped with a CCD camera Newton DU920P-BV (Andor Technology Ltd., Belfast, UK). The average spectral resolution of the Raman system was approximately 6.5 cm^{-1}. Raman spectra were obtained by single acquisition of 0.5 s at 100 different sample positions from 260–2480 cm^{-1}.

3. Results

3.1. Current, Voltage and Temperature During PEO

Voltage, current and electrolyte temperature transients for the PEO process with 1 M and 12.9 M H_2SO_4 concentration are represented in Figure 1, respectively. In comparison with El Achhab et al. [18] the process was further refined by increasing the number of voltage steps and the times per step.

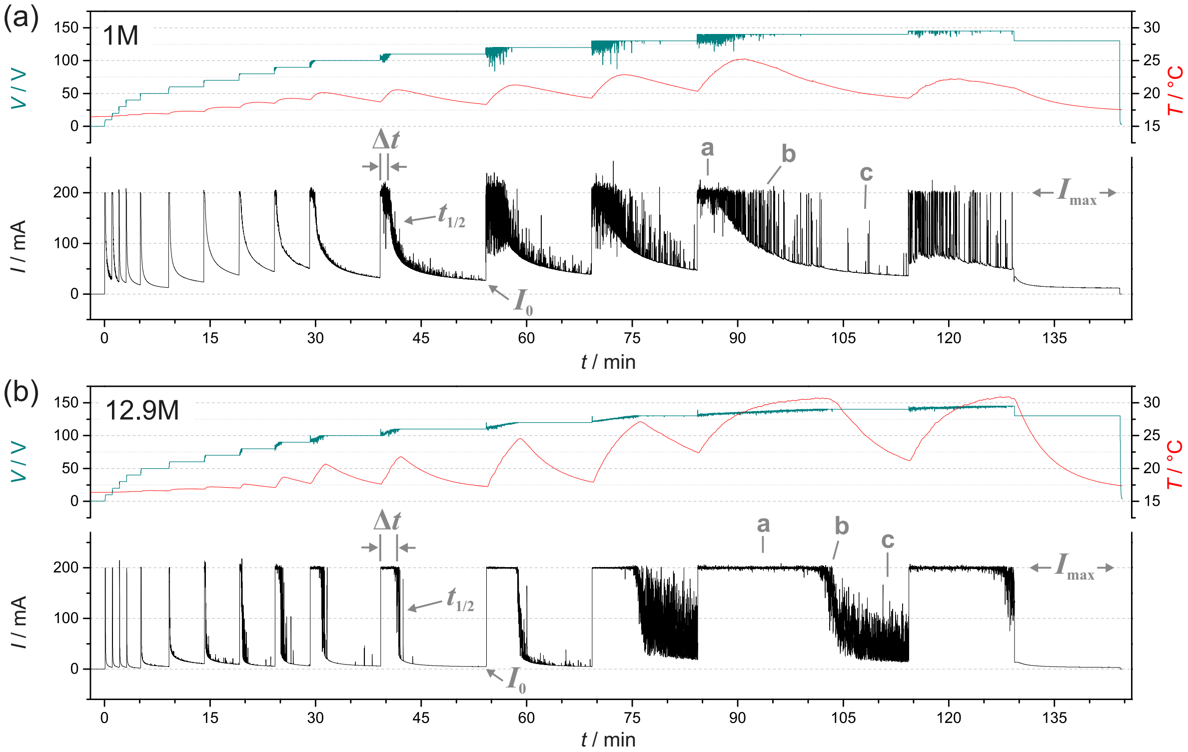

Figure 1. Voltage, current and temperature transients during the PEO process in (**a**) 1 M and (**b**) 12.9 M H_2SO_4 electrolyte concentration. Further explanation is given in the text.

In the beginning of the process, the electrolytic oxidation occurs under potentiostatic control, as confirmed by the exponential decrease of the current immediately after each voltage step. Strong oxide growth occurs only for several seconds and decreases rapidly. Oxide occurs preferentially at surface inhomogeneities, accompanied by the oxidation of the entire surface during the sufficiently long period. This procedure leads to a controlled oxide growth with a good stability and adhesion of the oxide layer to the substrate. In the regime of higher voltages, the current does not drop immediately after a voltage step. Here galvanostatic oxidation at I_{max} = 200 mA takes place during a period Δt. The current limitation of I_{max} prevents from electrically induced etching. The highest growth rate is expected in this period. After Δt the current decreases exponentially. The decay, described by the half-life $t_{1/2}$, represents the growth rate under potentiostatic conditions. The current I_0 in the end of an interval is determined by the insulating properties of the oxide and is a good indicator for the oxide layer after each voltage step and finally after the entire process.

Distinct peaks in the current transient originate from electrical breakdowns. At higher voltages, breakdowns are accompanied by visible light emission, originating from plasma discharges. Such light emissions have been studied by other groups. It is known that spectra of the emitted light change during the PEO process, due to the specific nature of the discharges [19]. Under galvanostatic control (i.e., at I_{max}), strong discharges can be visually observed. In these periods (for example period a in Figure 1) dielectric breakdowns affect the entire oxide layer and substrate. Discharges induce plasma conditions and, due to escaping gases, create a micropore structure. Neighboring regions are affected and further discharges are leading to a cascade. They move avalanche-like across the surface for a short duration of time. After Δt discharges occur less common and less intense (for example period b in Figure 1), due to the increased oxide layer thickness and its improved insulating properties. The oxide growth approaches always a limitation and finally only single discharges occur (for example period c in Figure 1). The corresponding peaks in the current transient are well below 200 mA and are caused by comparably weak discharges. We believe that they correspond to gas discharges, which occur in micropores, as previously investigated for PEO of aluminium [19].

The increase of the electrolyte temperature is a consequence of the electrical power dissipation into heat, especially during the time intervals Δt (i.e., at I_{max}). It was experimentally found that the stability and adhesion of the oxide is significantly reduced if the cooling is omitted. This seems to be in line with previous results on light metals, for which a high-temperature process promotes dissolution of the oxide layer [17]. Hence, the control of the electrolyte temperature by cooling is a prerequisite to yield high-quality oxide layers in our PEO process.

3.2. Microstructure

The visual appearance of the PEO samples is of light grey color, which is usually the case for porous titanium oxide. The comparison of all samples produced with different H_2SO_4 electrolyte concentrations suggests that the oxide thickness increases with the concentration.

Figure 2 presents the SEM images of the surfaces produced with 0.5 M, 1 M, 3 M, 7 M and 12.9 M H_2SO_4. All images confirm a porous structure of the oxide films. For 0.5 M, the pore size seems rather small and uniform. With increasing concentrations the pores enlarge and, simultaneously, the surface becomes rougher. The maximum roughness is found for 12.9 M.

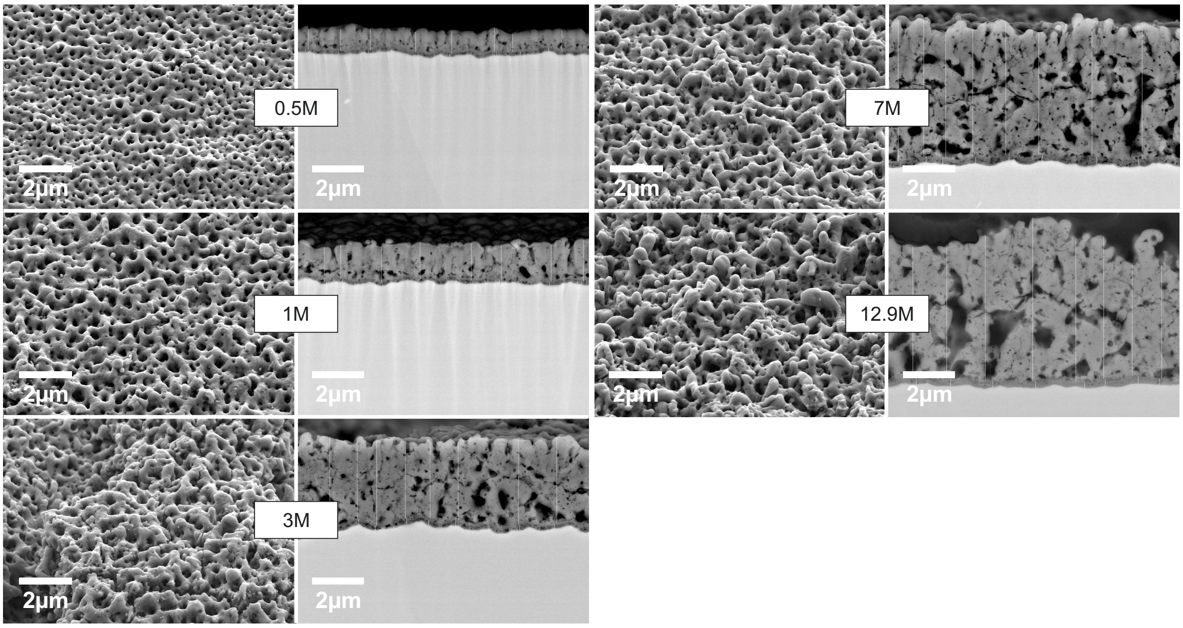

Figure 2. Scanning electron microscope surface and cross-section images from samples prepared with PEO in 0.5 M, 1 M, 3 M, 7 M and 12.9 M electrolyte concenctration of sulphuric acid.

To determine the thickness of the oxide layer, cross-sections of the samples were prepared and were imaged with SEM. They are shown in Figure 2. The oxide layer can be distinguished into two layers of different thickness and porosity, in accordance to other studies [8,14,15]. The titanium substrate is coated with a relative compact oxide interlayer. Table 1 summarizes the thicknesses of the porous and compact layers of the samples as well as the mean pore sizes. These data were determined at randomly selected sites of each SEM images.

Table 1. Pore size, thickness of the porous layer and thickness of the compact layer derived from SEM investigation.

	0.5 M	**1 M**	**3 M**	**7 M**	**12.9 M**
Pore size/µm	0.20 ± 0.09	0.25 ± 0.07	0.29 ± 0.08	0.35 ± 0.06	0.38 ± 0.07
Thickness porous layer/µm	0.79 ± 0.06	1.39 ± 0.09	3.18 ± 0.20	5.14 ± 0.20	5.21 ± 0.62
Thickness compact layer/µm	0.13 ± 0.03	0.12 ± 0.03	0.22 ± 0.04	0.25 ± 0.03	0.25 ± 0.03

3.3. Crystal Structure

3.3.1. X-ray Diffraction

XRD scans for samples prepared with 0.5 M, 1 M, 3 M, 7 M and 12.9 M are displayed from 24.5° to 42.5° in Figure 3. All marked reflections are assigned by ICDD card numbers 00-001-1198 (hexagonal α-Ti), 01-089-4920 (TiO_2 rutile) and 01-073-1764 (TiO_2 anatase). Reflections derived from brookite are not observed. Because of the increasing thickness of the oxide layer (as found in the SEM images), the reflection intensities derived from α-Ti, for example Ti(002), decrease with the concentration of H_2SO_4. At the same time, the intensities of the rutile-derived reflections, i.e., R(110), R(101), R(200) and R(111), increase strongly. In contrast the A(101) and A(004) reflections, that belong to anatase, behave differently. Here the reflections of the 0.5 M sample are significantly larger than for the samples which were prepared in higher concentrated H_2SO_4.

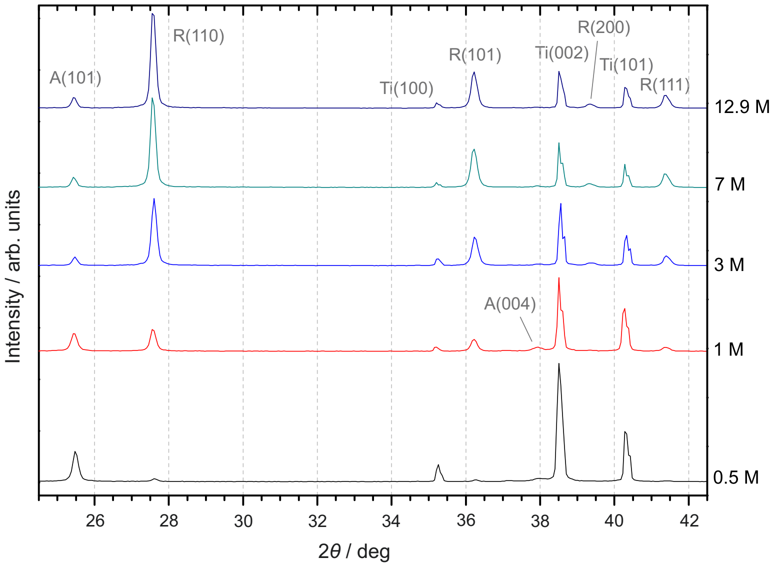

Figure 3. X-ray diffractograms from 24.5° to 42.5° (2θ) of samples produced with different H_2SO_4 concentrations. Labeled reflections are assigned to α-Ti, TiO_2 rutile and TiO_2 anatase. Most prominent features of the TiO_2 crystallographic phases are the (101) reflection for anatase ($2\theta = 25.46°$) and the (110) reflection for rutile ($2\theta = 27.59°$).

Several researchers have calculated x_R [12,20,21], the weight fraction of rutile, by comparing the intensities of the most prominent reflections of anatase and rutile, i.e., A(101) and R(110). We determined x_R according to

$$x_R = 1 - x_A = \frac{1}{1 + K\frac{I_A}{I_R}} \quad (1)$$

with K = 0.68 for $x_R \geq 0.8$ and K = 0.79 for $x_R < 0.8$ as first suggested by Spurr and Myers [20]. From our data the peak areas $I_A(101)$ and $I_R(110)$ were determined by deconvolution, using two Voigt functions and a linear background. The coefficient of determination (R^2) was $\geq$0.997.

3.3.2. Raman Spectroscopy

Recently, Raman spectroscopy is considered to be an alternative technique to determine rutile and anatase fractions in mixtures [21,22]. Here it is used in additional to XRD. In Figure 4 averaged Raman spectra from samples prepared with 0.5 M, 1 M, 3 M and 12.9 M are presented. Raman-active modes derived from anatase are centered around 395 cm^{-1} (B_{1g}), 515 cm^{-1} (B_{1g} and A_{1g}) and 637 cm^{-1} (E_g). two active modes frome the rutile phase around 442 cm^{-1} (E_g) and 605 cm^{-1} (A_{1g}) are identified [23,24].

The deconvolution in Figure 4 was done with OriginPro 9.0 (OriginLab Corp., Northampton, MA, USA). A linear background from 300–780 cm^{-1} was substracted. According to the origin of the Raman modes, we assumed a mainly Lorentian shape with a constant Gaussian contribution (due to instrumental effects), resulting in a Voigt profile. The total FWHM was limited to 50 cm^{-1} and the Gaussian width was kept constant at 5 cm^{-1}.

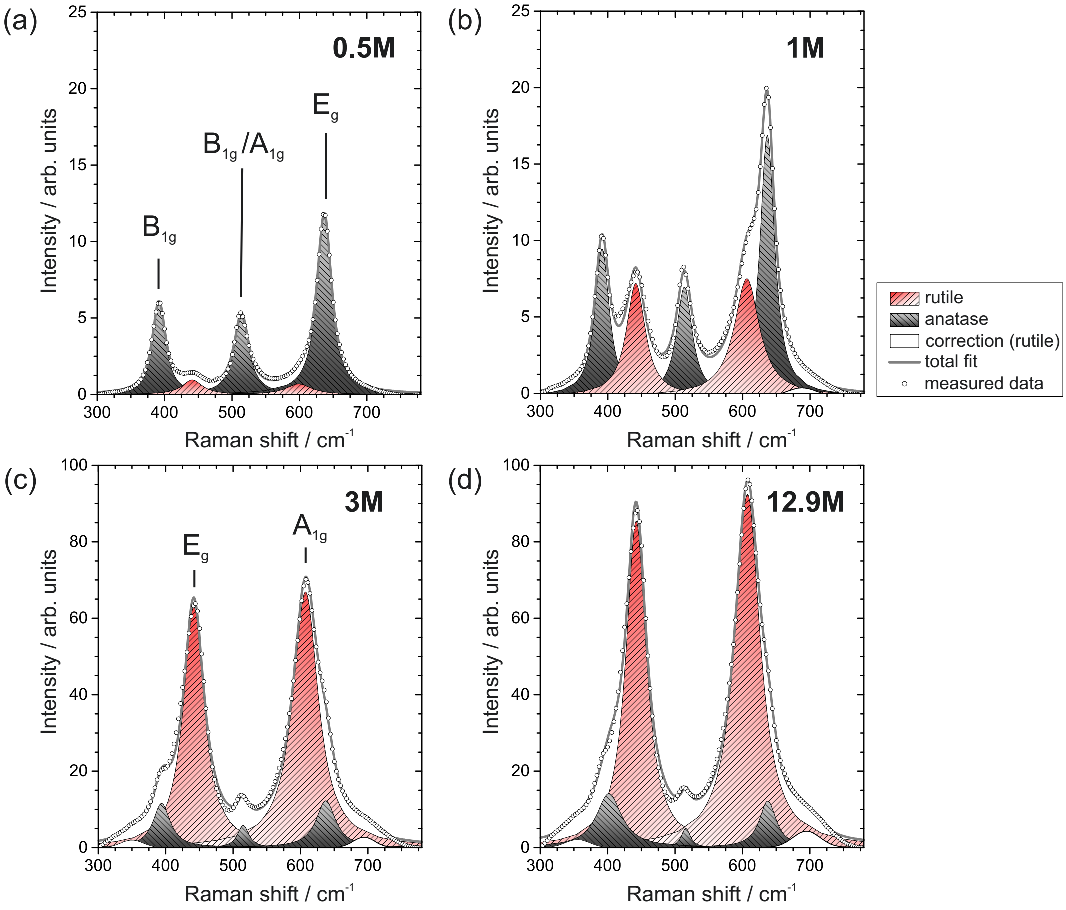

Figure 4. Raman spectra for TiO_2 samples from 300–780 cm^{-1} produced in (**a**) 0.5 M, (**b**) 1 M, (**c**) 3 M and (**d**) 12.9 M H_2SO_4. Data points are averaged from 100 single acquisitions along a line. Deconvolution were done with a linear background and voigt profiles. Raman active modes are labeled for anatase in (**a**) and for rutile in (**c**).

The evaluation shows that the mixed Raman spectra of rutile and anatase in the region 300–780 cm^{-1} are composed of more than five Raman active modes. The intensity around 515 cm^{-1} is derived from two single modes, B_{1g} and A_{1g}, of the anatase phase, but cannot be separated in the fitting procedure. Besides the first-order Raman modes, numerous combination modes contribute to the total spectra [24]. It can be assumed, that contributions of combination modes are mainly induced by the rutile phase. To take into account these combination modes, two corrections, in terms of two additional Voigt profiles, around 330–360 cm^{-1} and around 680–700 cm^{-1} were added. The final fit obtained a coefficient of determination (R^2) $\geq$0.994.

Zanatta et al. [21] suggested a method to estimate the concentration of rutile in TiO_2 and found

$$x_R = \frac{A_R}{A_A + A_R}, \tag{2}$$

with A_A and A_R, representing the total areas of anatase and rutile deconvolutions, respectively. Here the areas of the correction profiles contribute to the total area of rutile.

4. Discussion

We start the discussion of our results with a brief overview of the oxide growth model of the PEO process, previously suggested by El Achhab et al. [18]. It explains qualitatively the formation of the two well distinguishable oxide layers, i.e., the porous and the compact layer that were found in the SEM images of the samples' cross-sections. In the initial phase of our PEO process (i.e., for an applied voltage less than 90 V for 1 M and less than 70 V for 12.9 M H_2SO_4), potentiostatic conditions prevail and anodic oxidation controls the oxide growth on top of the titanium substrate. Ostwald's step rule suggests the formation of the less stable crystallite (in our case anatase) in a non-equilibrium situation for entropy reasons [25]. Therefore, we believe, that small nuclei of anatase are favored over rutile formation on the bare titanium surface. They coalesce and continuously grow until a first anatase layer covers the titanium. Each subsequent voltage step induces anatase growth and increases the thickness step-wisely at the surface of the titanium substrate. The growth can be associated with the current decay, seen in the transients of I (compare Figure 1). The evaluation of the decay yields a characteristic half life $t_{1/2}$ which varies with the electrolyte concentration.

After the initial phase (i.e., at voltages above 90 V for 1 M and 70 V for 12.9 M), the discharges occur and drastically affect the growth. In this regime of the PEO process, the applied voltage exceeds, immediately after a voltage step, the breakdown voltage V_B of the oxide layer. The I and V transients reveal galvanostatic conditions (i.e., in the period Δt, compare Figure 1). The nature of single discharges and their impact have been explained by several researchers for other systems [19,26] and is assumed to be analogous for TiO_2. These strong discharges degrade the passivation layer of anatase. It is locally destroyed and the bare titanium substrate can be chemically attacked by sulphuric acid. At these sites temporary dissolution occurs. An additional effect results from the plasma which is formed during these discharges and is accompanied by a local temperature rise. The high temperature causes melting, gas evolution and formation of channels in the oxide. Around the discharge channels the temperature is sufficiently high to induce an irreversible transformation of anatase to rutile. In a certain distance from the channel, the transformation temperature is not reached and no conversion of the anatase takes place. Due to the local removal of the passivating layer, the potential barrier breaks down and the discharges at these sites stop. The remaining oxide layer cools rapidly down and further transition of anatase to rutile is inhibited. Simultaneously, the continuous anodic oxidation of titanium to anatase heals the passivation layer and the dissolution gradually stops.

Galvanostatic conditions after a voltage step last, however, only for a short time (i.e., Δt) since the passivating property of the oxide layer increases. After Δt, the PEO process is again under potentiostatic control and the frequency as well as the intensity of discharges decrease over the course of time. The anodic growth of anatase dominates until the next voltage step is applied. Finally, the PEO process is completed when the last voltage step was conducted. Its value equals 130 V and is lower than the preceding value of 145 V.

Our results of SEM, XRD and Raman spectroscopy are summarized in Figure 5. The total layer thickness, derived from the SEM images of cross-sections from selected samples, can be separated into a porous (white column) and compact part (grey column). Both thicknesses increase with increasing H_2SO_4 electrolyte concentration, but the porous layer is always thicker. We found that the strongest effect in the thickness increase is below an electrolyte concentration of around 7 M. Evidently, higher concentrations lead to only marginally higher layer thicknesses. Compared to the porous layer, the compact oxide interlayer is relatively thin. Its thickness equals 0.12 μm for 1 M and increases weakly up to 0.25 μm for 12.9 M.

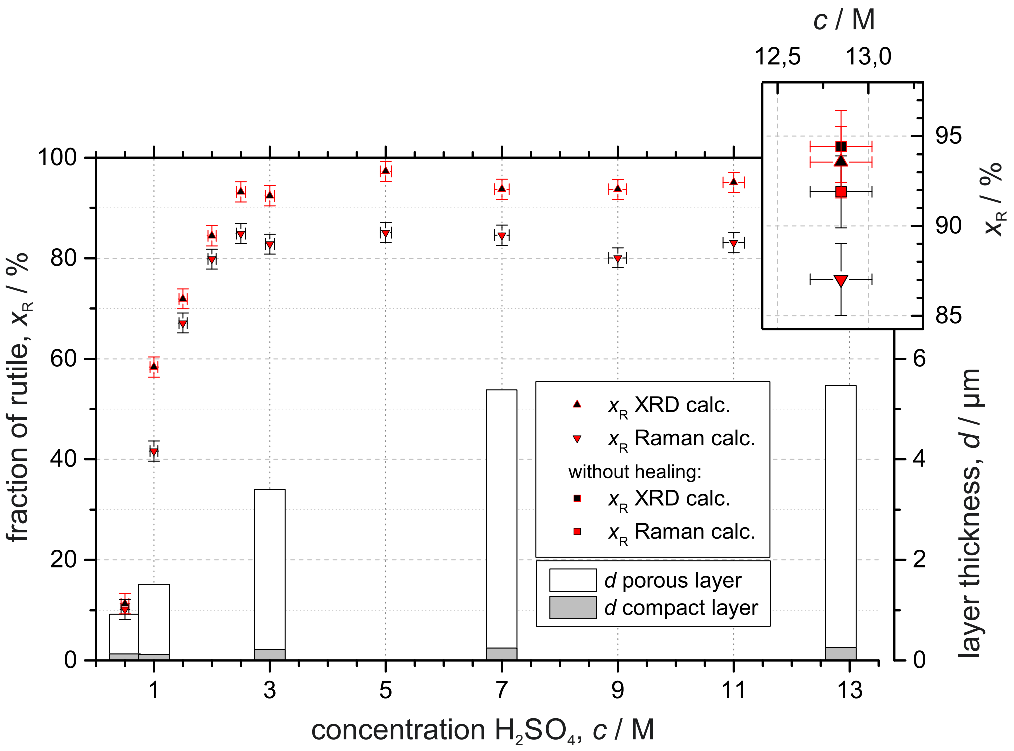

Figure 5. Experimentally derived weight fraction between TiO_2 crystal phases rutile and anatase in different samples as a function of H_2SO_4 concentration. The fraction is presented with the estimated uncertainty of each sample and is determined from data acquired with XRD and Raman spectroscopy. The columns represent the thickness of the porous and compact oxide layer, as determined by SEM investigation on selected samples.

We found a substantial change of the phase composition between electrolyte concentrations of 0.5 M and 3 M. In samples produced with 0.5 M, anatase dominates and has a fraction of more than 80%. For concentrations above 3 M, the rutile contribution exceeds and has a fraction of over 80%. Since the thickness of the porous layer increases at the same time, we assume that the porous layer is composed mainly of rutile. Both Raman spectroscopy and XRD data (compare Figure 5) indicate an increase of the rutile fraction x_R. However, it is evident that XRD-derived values of x_R are significantly larger than Raman-derived values (with one exception for 0.5 M). The Equation (1) was derived from XRD analysis of polycrystalline powders. Since the PEO process does not likely produce a random orientation of crystallites the evaluation of XRD data may exhibit a systematic error. Several effects have been discussed in the literature to explain such overestimation of x_R fractions from XRD data [21,22]. In our case, non-isotropic growth of the crystallites can also favor certain orientations which may cause larger peak intensities of the corresponding X-ray reflections.

With the help of the oxide growth model, given above, one can rationalize the observed concentration-dependence of thickness, microstructure and phase composition. The thickness of the compact layer, formed as the result of anodic oxidation, is controlled by the corresponding growth rate. The experiment shows that the values of the half life $t_{1/2}$, associated with anodic oxidation, decrease with rising electrolyte concentration. Half life times depend slightly on the initial value of each voltage step and may scatter significantly, due to the current spikes at higher voltages, that adversely affect their accurate determination. Quantitative values of $t_{1/2}$ are given here only for the voltage step 110 V (indicated in Figure 1), which are about 113 ± 20 s for 1 M and 10 ± 5 s for 12.9 M, respectively. In between, they decline monotonously with increasing concentration. It is also found that the values of I_0 are smaller in higher concentrations, which confirms thicker anatase layers. At the same time, the sum of Δt periods, in which the transformation of anatase to rutile takes place, becomes larger between 0.5 M to 12.9 M. We conclude that the effect of both anatase formation and anatase-to-rutile conversion is more pronounced at high concentrations of H_2SO_4. As a result, the total layer thickness increases strongly while the compact layer gets only slightly thicker for rising concentration.

The formation of the porous layer is mainly determined by the number and intensity of discharges that occur above the breakdown voltage V_B. Previous research has shown that V_B depends on the ion conductivity of the electrolyte, which is a function of the electrolyte concentration [13,27]. In accordance with the theory, V_B is smaller in 12.9 M than in 1 M (compare, e.g., the I transients for 12.9 M and 1 M in Figure 1). Correspondingly, discharges appear already around 70 V in 12.9 M while they appear around 90 V in 1 M. Besides the lower breakdown voltage V_B, the period of galvanostatic control Δt (i.e., $I = I_{max}$), in which strong discharges predominate, rise with electrolyte concentration. Another concentration-dependent effect arises from the etching of the oxide layer in the sulfuric acid. Since concentrated sulfuric acid reacts stronger than diluted one with respect to its dissolving property, one may assume that the increasing surface density of sites, locally etched by the acid, promote discharges. The combined action of these effects consequently enhances the pore sizes and roughness, at increasing concentrations of H_2SO_4. Since discharges also promote the transformation from anatase to rutile, the rutile fraction becomes larger and saturates at 3 M.

The last voltage step of our process is 130 V and is considerably lower than the previous voltage with 145 V. At this voltage, no discharges occur and anodic oxidation produces anatase at the titanium substrate. If the last voltage step is omitted in the PEO process the rutile fraction becomes slightly larger for a preparation in 12.9 M, as indicated in Figure 5. This observation is in line with our growth model of the oxide layer on titanium.

5. Conclusions

We refined a PEO process for titanium, which benefits from the combination of galvanostatic and potentiostatic oxidation. The effect of varying H_2SO_4 concentrations was investigated from 0.5 M up to 12.9 M. Thickness, porosity and phase composition change drastically. SEM investigations showed that the resulting oxide layer can be distinguished by a thin interlayer at the titanium substrate and a thick porous layer on-top of the interlayer. The former mainly consists of anatase, while the porous structure, greatly influenced by the impact of plasma discharges, reveals a large rutile content. The weight fractions of both modifications have been quantitatively determined by analyzing XRD and Raman spectroscopy data. Based on the experimental results, we gain further insight into the growth mechanism of our PEO-process. It was found that the H_2SO_4 electrolyte concentration can be used to control the number and intensity of discharges, as well as the anodic oxidation growth rate. Furthermore, it was shown that the concentration also alters the periods of galvanostatic and potentiostatic conditions. Hence, besides the influence of the electrolyte concentration, we believe that the structure of the plasma-electrochemically produced oxide layer can be adjusted by tuning the periods of galvanostatic and potentiostatic control.

Author Contributions: B.E., M.E., K.S. and B.F. conceived and designed the experiments; B.E. and B.F. performed the experiments; B.E. analyzed the data; B.E., M.E., K.S., B.F. and Ü.K.-D. contributed reagents/materials/analysis tools; B.E. wrote the paper.

Acknowledgments: This research was supported by Bundesministerium für Wirtschaft und Energie (BMWi) under project no. ZF4185502ZG6. We gratefully thank Egbert Wessel (Forschungszentrum Jülich, IEK-2, 52425 Jülich) for the SEM measurements. Fruitful discussions with Engin Ciftyürek are gratefully acknowledged.

Conflicts of Interest: The authors declare no conflict of interest.

References

1. Diamanti, M.V.; Ormellese, M.; Pedeferri, M. Application-wise nanostructuring of anodic films on titanium: A review. *J. Exp. Nanosci.* **2015**, *10*, 1285–1308. [CrossRef]

2. Diamanti, M.V.; Del Curto, B.; Pedeferri, M. Anodic oxidation of titanium: From technical aspects to biomedical applications. *J. Appl. Biomater. Biomech.* **2011**, *9*. [CrossRef] [PubMed]
3. Schierbaum, K.; El Achhab, M. Generation of an electromotive force by hydrogen-to-water oxidation with Pt-coated oxidized titanium foils. *Phys. Status Solidi* **2011**, *208*, 2796–2802. [CrossRef]
4. Karpov, E.G.; Hashemian, M.A.; Dasari, S.K. Chemistry-Driven Signal Transduction in a Mesoporous Pt/TiO_2 System. *J. Phys. Chem. C* **2013**, *117*, 15632–15638. [CrossRef]
5. Cakabay, Ö.; El Achhab, M.; Schierbaum, K. Thermal properties of solid-state Pt/TiO_2/Ti emf cells studied by microcalorimetry. *Appl. Phys. A* **2015**, *118*, 1127–1132. [CrossRef]
6. El Achhab, M.; Schierbaum, K. Gas sensors based on plasma-electrochemically oxidized titanium foils. *J. Sensors Sensor Syst.* **2016**, *5*, 273–281. [CrossRef]
7. Vanhumbeeck, J.F.; Proost, J. Current understanding of Ti anodisation: Functional, morphological, chemical and mechanical aspects. *Corros. Rev.* **2009**, *27*, 117–204. [CrossRef]
8. Quintero, D.; Galvis, O.; Calderón, J.; Castaño, J.; Echeverría, F. Effect of electrochemical parameters on the formation of anodic films on commercially pure titanium by plasma electrolytic oxidation. *Surf. Coat. Technol.* **2014**, *258*, 1223–1231. [CrossRef]
9. Sul, Y.T.; Johansson, C.B.; Jeong, Y.; Albrektsson, T. The electrochemical oxide growth behaviour on titanium in acid and alkaline electrolytes. *Med. Eng. Phys.* **2001**, *23*, 329–346. [CrossRef]
10. Yang, B.; Uchida, M.; Kim, H.M.; Zhang, X.; Kokubo, T. Preparation of bioactive titanium metal via anodic oxidation treatment. *Biomaterials* **2004**, *25*, 1003–1010. [CrossRef]
11. Diamanti, M.V.; Pedeferri, M.P. Effect of anodic oxidation parameters on the titanium oxides formation. *Corros. Sci.* **2007**, *49*, 939–948. [CrossRef]
12. Masahashi, N.; Mizukoshi, Y.; Semboshi, S.; Ohtsu, N. Enhanced photocatalytic activity of rutile TiO_2 prepared by anodic oxidation in a high concentration sulfuric acid electrolyte. *Appl. Catal. B Environ.* **2009**, *90*, 255–261. [CrossRef]
13. Friedemann, A.; Gesing, T.; Plagemann, P. Electrochemical rutile and anatase formation on (PEO) surfaces. *Surf. Coat. Technol.* **2017**, *315*, 139–149. [CrossRef]
14. Fadl-Allah, S.A.; El-Sherief, R.M.; Badawy, W.A. Electrochemical formation and characterization of porous titania (TiO_2) films on Ti. *J. Appl. Electrochem.* **2008**, *38*, 1459. [CrossRef]
15. Sun, C.; Hui, R.; Qu, W.; Yick, S.; Sun, C.; Qian, W. Effects of processing parameters on microstructures of TiO_2 coatings formed on titanium by plasma electrolytic oxidation. *J. Mater. Sci.* **2010**, *45*, 6235–6241. [CrossRef]
16. Yerokhin, A.; Nie, X.; Leyland, A.; Matthews, A.; Dowey, S. Plasma electrolysis for surface engineering. *Surf. Coat. Technol.* **1999**, *122*, 73–93. [CrossRef]
17. Li, Q.; Liang, J.; Wang, Q. Plasma Electrolytic Oxidation Coatings on Lightweight Metals. In *Modern Surface Engineering Treatments*; Aliofkhazraei, M., Ed.; InTech: Rijeka, Croatia, 2013; Chapter 4.
18. El Achhab, M.; Erbe, A.; Koschek, G.; Hamouich, R.; Schierbaum, K. A microstructural study of the structure of plasma electrolytically oxidized titanium foils. *Appl. Phys. A* **2014**, *116*, 2039–2044. [CrossRef]
19. Hussein, R.O.; Nie, X.; Northwood, D.O.; Yerokhin, A.; Matthews, A. Spectroscopic study of electrolytic plasma and discharging behaviour during the plasma electrolytic oxidation (PEO) process. *J. Phys. D Appl. Phys.* **2010**, *43*, 105203. [CrossRef]
20. Spurr, R.A.; Myers, H. Quantitative analysis of anatase-rutile mixtures with an X-ray diffractometer. *Anal. Chem.* **1957**, *29*, 760–762. [CrossRef]
21. Zanatta, A. A fast-reliable methodology to estimate the concentration of rutile or anatase phases of TiO_2. *AIP Adv.* **2017**, *7*, 075201. [CrossRef]
22. Hanaor, D.A.H.; Sorrell, C.C. Review of the anatase to rutile phase transformation. *J. Mater. Sci.* **2011**, *46*, 855–874. [CrossRef]
23. Balachandran, U.; Eror, N.G. Raman spectra of titanium dioxide. *J. Solid State Chem.* **1982**, *42*, 276–282. [CrossRef]
24. Frank, O.; Zukalova, M.; Laskova, B.; Kürti, J.; Koltai, J.; Kavan, L. Raman spectra of titanium dioxide (anatase, rutile) with identified oxygen isotopes (16, 17, 18). *Phys. Chem. Chem. Phys.* **2012**, *14*, 14567–14572. [CrossRef] [PubMed]
25. Van Santen, R.A. The Ostwald step rule. *J. Phys. Chem.* **1984**, *88*, 5768–5769. [CrossRef]

26. Klapkiv, M.D.; Nykyforchyn, H.M.; Posuvailo, V.M. Spectral analysis of an electrolytic plasma in the process of synthesis of aluminum oxide. *Mater. Sci.* **1995**, *30*, 333–343. [CrossRef]
27. Albella, J.; Montero, I.; Martinez-Duart, J. A theory of avalanche breakdown during anodic oxidation. *Electrochimica Acta* **1987**, *32*, 255–258. [CrossRef]

P.II Plasma Electrolytic Oxidation of Titanium in H_2SO_4-H_3PO_4 Mixtures

Publication Reference

[99]:

B. Engelkamp, B. Fischer, and K. Schierbaum, *Plasma Electrolytic Oxidation of Titanium in H_2SO_4-H_3PO_4 Mixtures*, Coatings **2020**, 10(2), 116.
doi:10.3390/coatings10020116

Copyright statement

Author Contributions

B.F. designed, conceived, and performed the confocal Raman microscopy; B.E. designed, conceived, and performed the other experiments; B.E. validated and analyzed the results; K.S. supervised the project; B.E. wrote the paper.

coatings

MDPI

Article

Plasma Electrolytic Oxidation of Titanium in H_2SO_4–H_3PO_4 Mixtures

Bernd Engelkamp [1,*], Björn Fischer [2] and Klaus Schierbaum [1]

[1] Abteilung für Materialwissenschaft, Institut für Experimentelle Physik der kondensierten Materie, Heinrich-Heine-Universität Düsseldorf, Universitätsstraße 1, 40225 Düsseldorf, Germany; klaus.schierbaum@hhu.de

[2] Raman Spectroscopic Services, FISCHER GmbH, Necklenbroicher Str. 22, 40667 Meerbusch, Germany; fischer@ramanservice.de

* Correspondence: bernd.engelkamp@hhu.de; Tel.: +49-211-81-15256

Received: 19 December 2019; Accepted: 28 January 2020; Published: 30 January 2020

Abstract: Oxide layers on titanium foils were produced by galvanostatically controlled plasma electrolytic oxidation in 12.9 M sulfuric acid with small amounts of phosphoric acid added up to a 3% mole fraction. In pure sulfuric acid, the oxide layer is distinctly modified by plasma discharges. As the time of the process increases, rough surfaces with typical circular pores evolve. The predominant crystal phase of the titanium dioxide material is rutile. With the addition of phosphoric acid, discharge effects become less pronounced, and the predominant crystal phase changes to anatase. Furthermore, the oxide layer thickness and mass gain both increase. Already small amounts of phosphoric acid induce these effects. Our findings suggest that anions of phosphoric acid preferentially adsorb to the anodic area and suppress plasma discharges, and conventional anodization is promoted. The process was systematically investigated at different stages, and voltage and oxide formation efficiency were determined. Oxide surfaces and their cross-sections were studied by scanning electron microscopy and energy-dispersive X-ray spectroscopy. The phase composition was determined by X-ray diffraction and confocal Raman microscopy.

Keywords: titanium dioxide; plasma electrolytic oxidation; anatase and rutile

---

1. Introduction

The oxide layer of metals such as titanium can be tailored for specific applications. The most common technique used to artificially grow a passive layer is anodic oxidation, in which moderate voltages promote a denser and thicker oxide layer compared with the naturally formed oxide. With the increasing scope of applications, new demands on materials have evolved. To meet these needs, researchers have developed new techniques from classical anodic oxidation. One derived technique is plasma electrolytic oxidation (PEO), in which the applied voltage exceeds a critical point and causes the initial oxide layer to reform by characteristic breakdowns, which often induce plasma conditions. The complex interplay between chemical, electrochemical, and thermodynamic reactions creates unique oxide layers and enables versatile changes in these layers by slightly changing the process parameters. Therefore, PEO-treated titanium can be used for a variety of applications, such as biomedical prostheses, automotive components, and photocatalytic devices [1].

Furthermore, PEO-treated titanium has recently been used as a gas sensor material at room temperature for various gases [2]. In this case, H_2SO_4 at an exceptionally high concentration of 12.9 M is used as an electrolyte and leads to a characteristic porous oxide structure with a layer thickness of approximately 5.5 μm. The morphology and thickness suggest a high surface-to-bulk ratio, which is beneficial for gas sensor technology. In general, breakdowns during PEO promote the formation of crystalline titanium dioxide phases, namely, anatase and the high-temperature phase rutile [3–5]. Both phases differ in significant properties (e.g., band-gap energy and electron–hole recombination rate) for potential application as a gas sensor material [6]. When investigating the effect of the crystal phase composition on the gas–oxide interaction, the ability to systematically control the rutile to anatase fraction is desirable. In 12.9 M H_2SO_4, the dominant crystal phase in the oxide is rutile, while the anatase fraction dominates in lower concentrations [7]. However, lower concentrations adversely affect the oxide layer by decreasing its thickness and porosity.

In recent studies on PEO for medical applications, electrolytes with phosphoric acid (H_3PO_4) have been frequently used, and oxide layers of comparable porosity and thickness can be formed [8–10]. Anatase is the dominant phase in these layers, and rutile is almost non-existent. When used as an electrolyte, phosphoric acid not only affects the phase composition but also drastically changes the outcome of the PEO process. The combination of both electrolytes provides an interesting approach to tailoring the properties of the oxide scale. Since the ratio of the two compounds in the mixture is critical for obtaining specific properties, we explored the effect of small amounts of H_3PO_4 in concentrated H_2SO_4.

Our PEO experiment is based on a galvanostatic DC operation mode. The resulting constant current offers a simple method of treating and evaluating samples for a systematic PEO study. For instance, it can be split into several contributions and classified into ionic and electronic currents [8,11]. The ionic current reflects the migration of ions in the oxide layer and is the driving force in conventional anodic oxidation. The electronic current is mainly induced by breakdowns. In the course of the PEO process, a transition from ionic to electronic current can be observed.

Starting with concentrated sulfuric acid (12.9 M) as an electrolyte, we investigated the impact of adding H_3PO_4 at molar fractions of 1% and 3%. Before and after PEO, the samples were analyzed for weight gain with a microbalance. Scanning electron microscopy and X-ray diffraction were used to systematically study oxide surfaces and cross sections at different stages of the process. We derived information about the phase distribution in the oxide layer from confocal Raman microscopy of cross sections, and elemental composition was investigated by energy-dispersive X-ray spectroscopy.

2. Materials and Methods

Samples (surface area of approx. 3.634 cm^2) were cut from titanium foil (thermally annealed, 99.6% purity; 125 μm thickness) by means of a laser (PowerLine F30, ROFIN-SINAR Laser GmbH, Hamburg, Germany). The samples were cleaned ultrasonically for approximately 10 min in acetone and 10 min in deionized water. The electrolytic cell consisted of a glass vessel with an integrated glass shell, which enabled the temperature regulation of the electrolyte by pumping cold thermal fluid through the shell. The thermal fluid temperature was kept constant at 15 °C with a recirculating cooler (FL1201, JULABO GmbH, Seelbach, Germany). The reaction chamber was filled with 114 ± 5 mL of the electrolyte. The electrolyte was based on 12.9 M H_2SO_4 (75 wt%). It was enriched with 25 wt% H_3PO_4, which resulted in molar fractions of $n(H_3PO_4)/n(H_2SO_4)$ = 0%, 1%, and 3%. Specifically, the last two fractions corresponded to $c_{1\%}(H_3PO_4) = 0.1$ M plus $c_{1\%}(H_2SO_4) = 12.3$ M and $c_{3\%}(H_3PO_4) = 0.3$ M plus $c_{3\%}(H_2SO_4) = 11.4$ M. A magnetic stirrer prevented spatial temperature differences in the electrolyte and reduced the disturbance of gas accumulations on the electrode surfaces. The electrolytic system was completed by the titanium sample as the anode and a graphite rod as the cathode (area of immersion of 7.38 ± 0.6 cm^2) at a distance of 23 ± 4 mm.

A constant current density of 55 $\mathrm{mA/cm}^2$ was applied by using a highly stable current power supply (FUG MCP 350-350). Voltage and current were adjusted and recorded in 250 ms intervals using an in-house developed LabVIEW program. After treatment, the sample was rinsed in deionized water and dried in air. The weight of the sample was measured before and after the process with an analytical balance (ABT 120-5DM, Kern und Sohn GmbH, Germany) with a repeatability of 0.02 mg.

The microstructure of the oxide layer was investigated by field emission scanning electron microscopy (SEM; JSM-7500F, JEOL Ltd., Tokyo, Japan). Surface images of secondary electrons were captured with 5 kV excitation. Cross sections were prepared by argon ion milling (Cross Section

Polisher IB-09010CP, JEOL Ltd., Tokyo, Japan). For energy-dispersive X-ray spectroscopy (EDX), images were created with 15 kV excitation energy and detected with an XFlash Detector 5030 (Bruker AXS GmbH, Karlsruhe, Germany). Quantitative results of elemental composition were obtained by averaging over at least three comparable sections to minimize local fluctuations.

The phase composition was determined by X-ray diffraction (XRD). Diffraction data were collected on a Bruker D2 Phaser diffractometer with Cu-Kα radiation (λ = 1.54184 Å, 30 kV, 10 mA) in Bragg–Brentano geometry and a LYNXEYE 1D detector. XRD patterns were measured with a flat silicon, low-background rotating sample holder (5.0 min^{-1}) with $24.5° < 2\theta < 29.5°$, a scan speed of 2 s/step, and a step size of approximately 0.024°.

Raman measurements were performed with a confocal Raman microscope alpha300 R (WITec GmbH, Ulm, Germany). A fiber-coupled single-mode DPSS laser with an excitation wavelength of 532 nm was used. The laser power applied to the sample was set to 20 mW. A Zeiss EC Epiplan-Neofluar DIC 100x/0.9 NA was selected as the microscope objective, and the samples were scanned with a step size of 200 nm. In this way, a spatial resolution of about 300 nm could be achieved. The system also featured real-time laser profilometry, so the sample surface remained in the focal plane during the entire measurement period. The spectrometer used was a WITec UHTS 300 combined with an Andor iDus Deep Depletion CCD detector, which was cooled to −60 °C. The Raman scattered light was spectrally dispersed by a reflection grating with 1200 mm^{-1}. The average spectral resolution was about 2 cm^{-2}/pixel. The software WITec FIVE version 5.2.4.81 was used to evaluate the measurement data and create Raman images, including cosmic ray removal and background subtraction by the implemented shape function.

3. Results

3.1. Voltage Response and Mass Change

The voltage response of the PEO process in 12.9 M H_2SO_4, as shown in Figure 1a, reveals information about the current character. The ratio between electronic and ionic currents varies during the PEO process. In the beginning, the electric field was insufficient to cause electric breakdowns, and conventional anodic oxidation occurs. The ionic current predominated and promoted the formation of a dielectric oxide layer. Consequently, the cell resistance increased. The constant current was sustained by the rapid increase in applied voltage. Above a critical voltage, electrical breakdowns become visible by electroluminescence. The charge transfer by breakdowns represents an electronic current and is energetically favored compared with ion migration. The electronic current increasingly contributes to the total current. Eventually, a linear voltage region is reached, which indicates a mainly electronic current character. This linear stage is also known as the microarc stage [9,12].

The impact of breakdowns on oxide formation was further investigated by terminating the process at different charge densities and determining the mass change, presumably due to oxide formation, with an analytical balance. Figure 1b presents the mass change with varying charge densities. The slope of the polynomial fit represents the mass change per transferred charge, i.e., the oxide formation efficiency [13]. The efficiency for 0% H_3PO_4 was positive until 8.4 C/cm^2, after which it was negative. This turning point corresponded to the beginning of the linear microarc stage. This indicates that breakdowns during the microarc stage in concentrated sulfuric acid cause mass loss of the oxide. The initial passivation by breakdowns transforms into a destructive reforming with combined mass loss.

The progress drastically changed by adding small amounts of H_3PO_4 to concentrated sulfuric acid. The voltage response for $n(H_3PO_4)/n(H_2SO_4)$ = 1% in Figure 1a already differed from the voltage response in pure H_2SO_4. The transition from ionic to electronic current was also observable by the subsequent decreasing voltage rate. However, it was less pronounced. The interruption of the steep increase between 1.5 and 7 C/cm^2 is due to the previously reported transition from a grooved morphology to a porous morphology [13,14]. The mass loss in Figure 1b was suppressed compared with samples prepared in pure H_2SO_4. The efficiency was positive until 19.4 C/cm^2. Shortly after the efficiency changes to negative values, the microarc region started, and no noticeable voltage gain occurred. Hence, the applied voltage was sufficient to sustain the defined current density, even though the oxide formation efficiency in this region (Figure 1b) was negative. Therefore, a steady state between repassivation of the dielectric layer and its destruction by breakdowns can be assumed.

With 3% phosphoric acid, the trend continued more drastically. Higher voltages, even above 200 V, were necessary to sustain the given current density. The transition from ionic to electronic currents was completed even later, while the mass change was always positive. At approximately 55.8 C/cm^2, the efficiency changed from positive to negative values, and the microarc region started. However, above approximately 70 C/cm^2, inhomogeneities were visible on the oxide surface and restricted the process in 3% H_3PO_4 at higher charge densities.

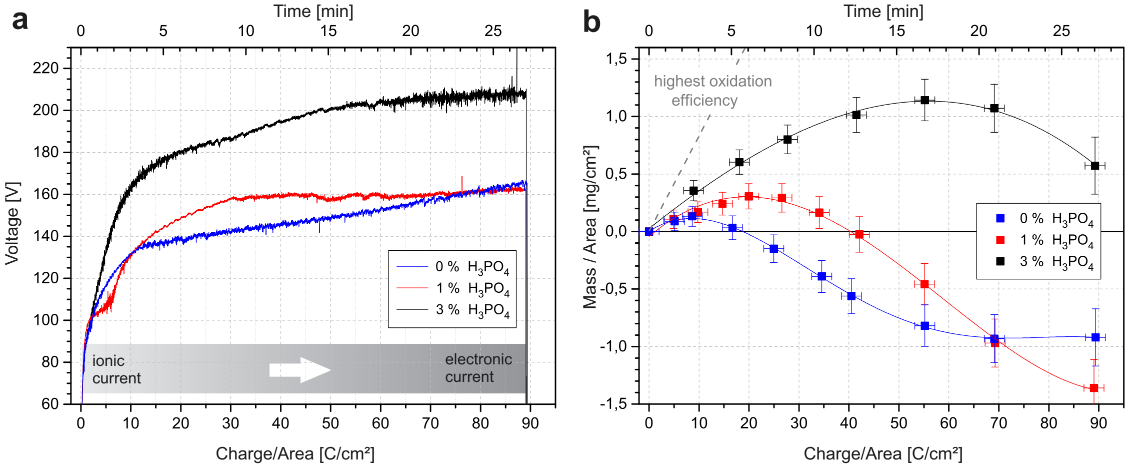

Figure 1. Process information at different charge densities for 0%, 1%, and 3% additional H_3PO_4 in 12.9 M H_2SO_4: (**a**) voltage response and (**b**) mass change with interpolation and marked highest oxidation efficiency.

3.2. XRD Investigation

The crystallographic structure of the oxide was investigated by X-ray diffraction (XRD). The weight fraction of rutile can be estimated for each sample by using the (101) reflection of anatase and the (110) reflection of rutile [7,15]. Figure 2 presents the calculated rutile fraction for different charge densities. The rutile fraction in the sample prepared with 0% H_3PO_4 increased continuously with the charge density until the sample was almost exclusively rutile. The titanium reflections of the titanium substrate decreased continuously as a result of the growing oxide layer [7]. The transition was similar in 1% H_3PO_4, but it was less pronounced. At a low charge density, mainly anatase was present, and the rutile fraction increased with increasing charge density. However, the maximum value and the slope of the fitted curve are smaller. For 3% H_3PO_4, our findings were remarkably different, and the typical increase in the rutile to anatase fraction was no longer identified. The fraction was below 11% for any charge density.

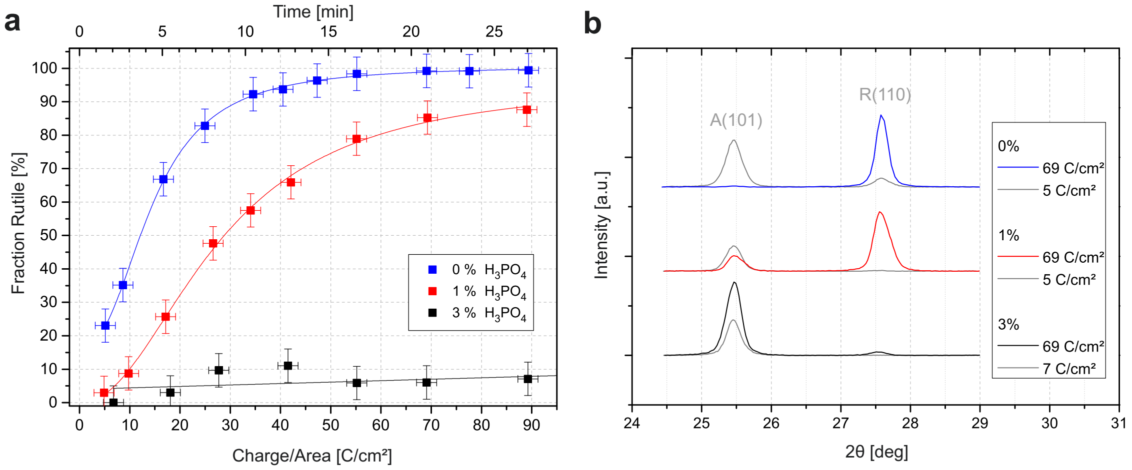

Figure 2. (**a**) Rutile to anatase fractions (with interpolation) versus the charge density for samples prepared with 0%, 1%, and 3% additional H_3PO_4 in 12.9 M H_2SO_4. The fractions are derived from XRD intensities. (**b**) Representative diffractograms of chosen samples with high and low current densities.

3.3. SEM Surface Images

The scanning electron microscope (SEM) images of surfaces in Figure 3 demonstrate the modification of surfaces resulting from variations in the transferred charge and the amount of H_3PO_4. In the left column, the surfaces of samples prepared with 0% H_3PO_4 are shown. Since the breakdown voltage was already exceeded for 9 $\mathrm{C/cm^2}$, circular sinkholes of former discharge channels, i.e., micropores, were clearly visible. However, the even distribution caused the surface to appear regular and flat. With increasing charge transfer, the surface became rougher. At 41 $\mathrm{C/cm^2}$, some minor plateaus and some cracks were noticeable. For 69 $\mathrm{C/cm^2}$, plateaus and cracks were clearly visible and impaired the circular shape of pores.

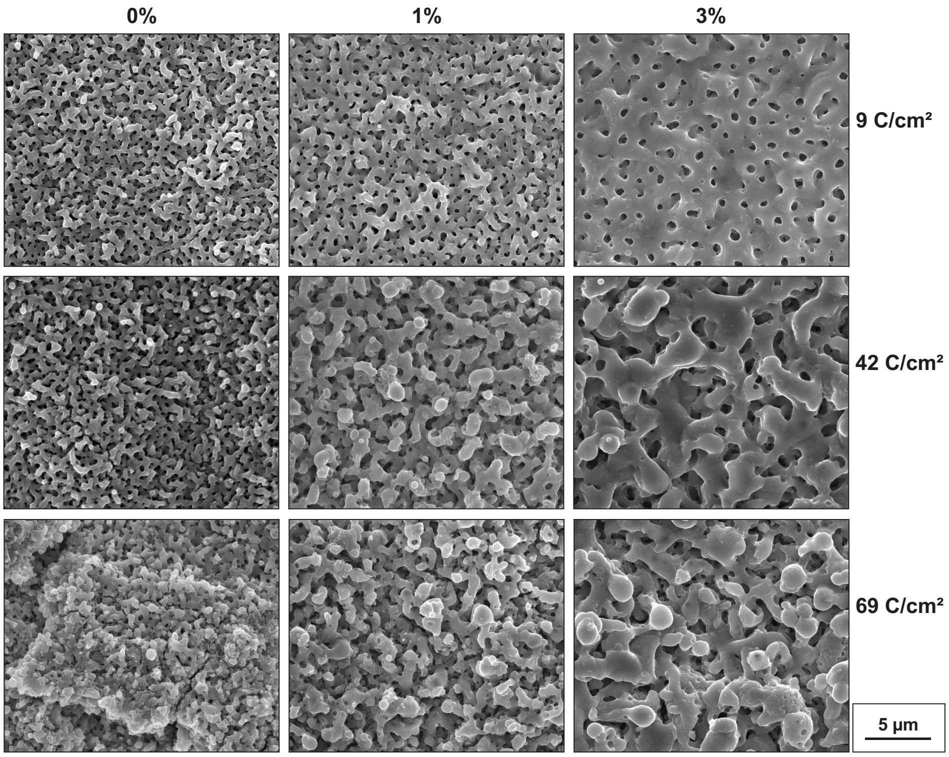

Figure 3. SEM images of sample surfaces produced in H_2SO_4 with the addition of 0%, 1%, or 3% H_3PO_4. Samples produced with similar charge densities (±1.0 $\mathrm{C/cm^2}$) are presented in the same row.

In the second column, the surfaces of the samples prepared in 1% H_3PO_4 are shown. The porous structure remained apparent. However, the pore size increased, and the pore density decreased. As observed previously, the pore network dissolved at a higher charge density, and different levels of depth evolved. In the right column, the surfaces of samples prepared in 3% H_3PO_4 are presented. The pore size further increased, and the density further decreased. The destructive character of the breakdowns can be observed, although it was less pronounced compared with the samples prepared in 0% or 1% H_3PO_4.

3.4. SEM Cross Sections

The result of our SEM cross section investigation in Figure 4 shows the depth profile of the oxides. The total thickness distinctly increased with the fraction of phosphoric acid in the electrolyte. Values were approximately 5.0 μm for 0%, 7.3 μm for 1%, and 10.9 μm for 3% (±0.5 μm). Different layers could be distinguished in the oxide layer because they abruptly changed in morphology or elemental composition. Two layers were as described for PEO in sulfuric acid: a compact layer beside the titanium substrate with a relatively small thickness and a porous layer with a major contribution to the total thickness [7,16]. Furthermore, in Figure 4c, a smooth area in the near the surface was clearly distinguishable from the porous layer below.

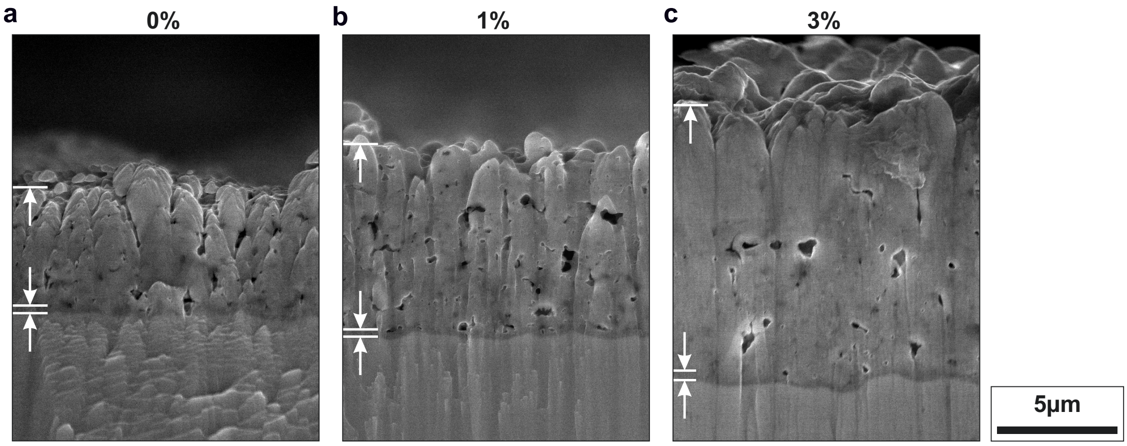

Figure 4. SEM images of oxide cross sections produced in H_2SO_4 with the addition of 0% (**a**), 1% (**b**), and 3% (**c**) H_3PO_4. The charge density in all plasma electrolyte oxidation (PEO) processes is $41.3 \pm 1.0\ \mathrm{C/cm^{-2}}$.

3.5. EDX Images

While the compact layer is rather difficult to resolve in the SEM cross section image, it is clearly identifiable by its elemental composition. This is shown in Figure 5 by the energy-dispersive X-ray spectroscopy (EDX) images. Remarkably, the compact layer in all samples exhibited an increased sulfur concentration of approximately 1.1 ± 0.3 at % (while it was below 0.3 ± 0.3 at % in the remaining oxide). In samples prepared with H_3PO_4, an increased phosphor concentration throughout the oxide could be detected. For 3% H_3PO_4, the value is approximately 1.9 ± 0.3 at %. In comparison, the phosphor concentration in a sample produced in 1% H_3PO_4 amounted to 0.6 ± 0.3 at %. Another feature was detectable in the sample produced in 3% H_3PO_4 and less pronounced in the sample produced in 0% H_3PO_4: a smooth area near the surface was observed in several samples and independent of the electrolyte composition. The EDX analysis in Figures 5a,c reveals that the region exhibited an increased titanium concentration, while the oxygen and phosphor concentration decreased.

3.6. Confocal Raman Microscopy

Since a common drawback of XRD phase analysis is the low spatial resolution, we additionally performed confocal Raman microscopy. Figure 6 shows false-color images, which are derived from Raman microscopy of cross sections prepared with $41.3 \pm 1.0\ \mathrm{C/cm^{-2}}$ in mixtures with 0%, 1%, and 3% additional H_3PO_4. The surrounding background image is the result of light microscopy. The different colors in the false-color images indicate the types of Raman spectra, which are presented below. The anatase phase is recognized by an intense E_g mode around 147 cm^{-1} [17]. Additionally, Raman-active modes derived from anatase around 395 cm^{-1} (B_{1g}), 515 cm^{-1} (B_{1g} and A_{1g}), and 637 cm^{-1} (E_g) are used for classification [7]. The rutile phase can be identified by two Raman modes around 442 cm^{-1} (E_g) and 605 cm^{-1} (A_{1g}) [7].

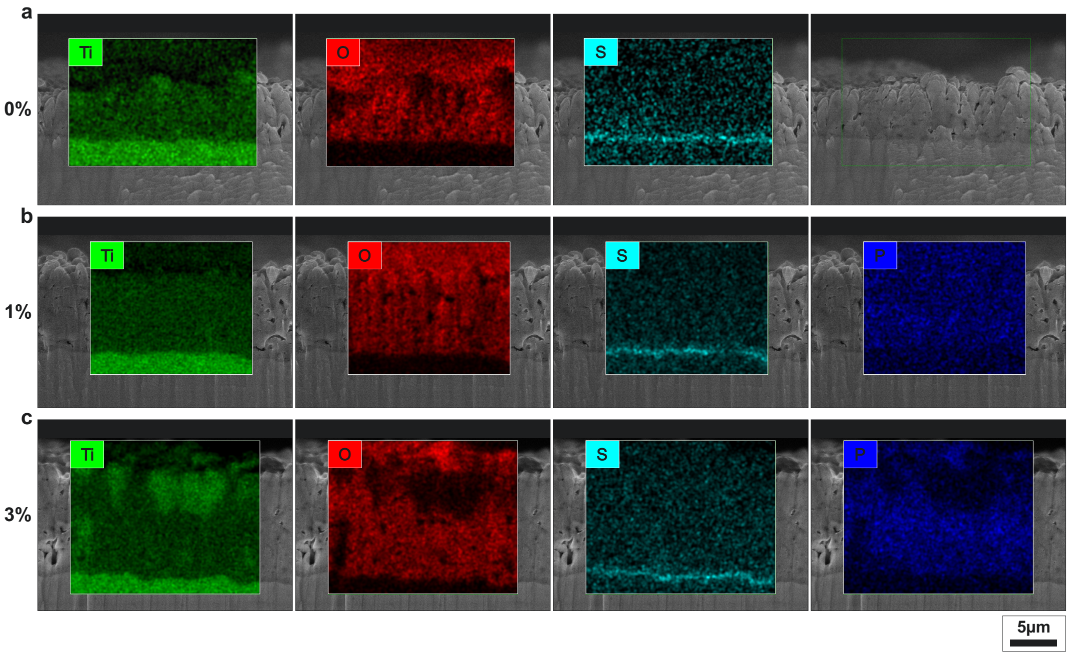

Figure 5. Energy-dispersive X-ray spectroscopy (EDX) images of oxide cross sections produced in 12.9 M H_2SO_4 with 0% (**a**), 1% (**b**), and 3% (**c**) H_3PO_4. The transferred charge density is around 41.3 ± 1.0 C/cm^{-2} for each sample. The color intensity in the analyzed segment is only comparable to other elemental maps for the same cross section.

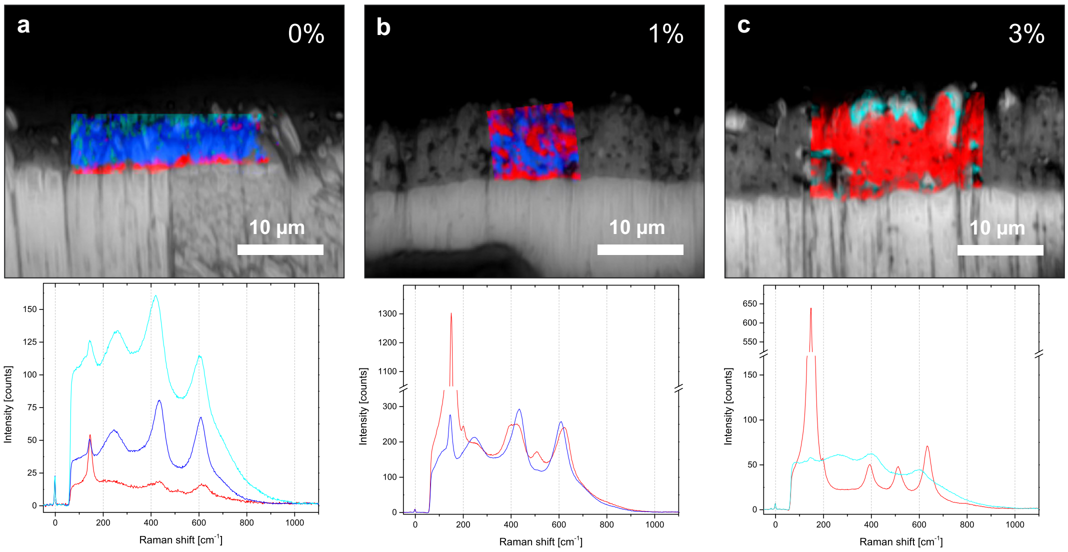

Figure 6. False-color images derived from confocal Raman microscopy with underlying light microscopy images of three cross sections. The transferred charge density is around 41.3 ± 1.0 C/cm^{-2} for all cross sections, while the fraction of H_3PO_4 in the electrolyte changes, i.e., 0% (**a**), 1% (**b**), and 3% (**c**). Red represents anatase, blue represents rutile, and cyan corresponds to a signal with large background. The integration time of each single spectrum varies, with 0.2 s in 0%, 0.1 s in 1%, and 0.05 s in 3%. Averaged spectra from the corresponding color-marked area are shown below each cross section.

Without H_3PO_4, the porous layer mainly exhibited rutile, while a distinct anatase fraction could be identified from the spectra of the compact layer. For 1% H_3PO_4, the colored areas, which indicate anatase and rutile, were similar in size and homogeneously distributed. For 3%, the intensities of the rutile modes in the spectra vanished. The entire oxide mainly exhibited anatase. For 0% and 3%, small areas near the surface were marked with cyan and fitted the previously mentioned smooth area in our SEM and EDX images. The corresponding cyan spectra resembled the spectra from rutile. However, it clearly differed by a frequency shift and an increased background signal, which may have originated from near-surface groups.

4. Discussion

Our results demonstrate that adding phosphoric acid to concentrated sulfuric acid as an electrolyte has a drastic influence on oxide formation in PEO. With 1% or 3% additional phosphoric acid, higher potentials are necessary to sustain the constant current density. This indicates an enhanced dielectric layer in terms of electrical resistance, with either increased thickness or higher electrical resistivity. The SEM cross sections confirm an increasing thickness. The promoted oxidation is associated with the mass gain in Figure 1b, which is mainly negative in 12.9 M H_2SO_4, partly positive with 1% H_3PO_4, and positive for all investigated charge densities with 3% H_3PO_4.

While oxide formation is promoted, breakdown effects are inhibited by adding H_3PO_4, which results in diminished breakdowns [10,14]. One indicator is the suppressed surface destruction, as shown in Figure 3. Breakdowns may cause plasma oxidation; however, almost all electric energy is used for ionization, water vaporization, joule heating, and gas evolution, especially in the microarc region [18]. As a consequence, plateaus and cracks evolve on the surface. After adding H_3PO_4 to the electrolyte, these effects decrease. Closely related is the mentioned mass loss in Figure 1b. It is assumed that the mass loss is promoted by breakdowns. Since the mass change becomes positive with additional H_3PO_4, lower breakdown intensity is expected.

Furthermore, reduced breakdown intensity can be identified from the phase composition. Rutile is a high-temperature modification and formed from anatase in an irreversible, time-dependent transformation [6]. In PEO, the energy for transformation is brought into the system by electrical breakdowns. When breakdowns diminish in the process, transformation is reduced or even disabled [7]. Results derived from the XRD analysis in Figure 2 show that the rutile fraction decreases with an increasing amount of H_3PO_4. Confocal Raman microscopy data, as presented in Figure 6, confirm this observation. Our results suggest that the energy liberated by breakdowns decreases with an increasing amount of H_3PO_4. With even higher concentrations of H_3PO_4, it is assumed that the crystallization is further inhibited and that even the anatase fraction is reduced [19].

In our discussion of the impact of additional H_3PO_4, we must consider that the concentrations of both acids decrease if one mixes appropriate amounts of H_2SO_4 (75 wt%) and H_3PO_4 (25 wt%). For example, when adjusting a fraction of $n(H_3PO_4)/n(H_2SO_4) = 3\%$, the resulting concentration of H_2SO_4 is 11.4 M, while the concentration of H_3PO_4 is 0.3 M. To understand the dilution influence of H_2SO_4, we conceived a PEO experiment with 11.4 M H_2SO_4. As a result, no significant change in the breakdown character was observed. In conclusion, the additional H_3PO_4 causes the drastic change observed in the PEO process.

To rationalize our findings, we correlated the impact of additional H_3PO_4 in 12.9 M H_2SO_4 to the corrosion of titanium in the electrolyte. In pure H_2SO_4 and the absence of an applied potential, the maximum corrosion rate is between 12.5 [20] and 13.7 M [21]. With an applied concentration of 12.9 M, a strong chemical etching can therefore be expected. In contrast, a simple corrosion experiment without applied potential in 12.9 M H_2SO_4 with 3% H_3PO_4 clearly demonstrates that the corrosion rate drastically decreases. A possible explanation is that solvated H_3PO_4 anions preferentially adsorb onto the anodic area. A similar effect is known to occur for corrosion inhibitors in H_2SO_4 [20]. As a consequence of the preferential adsorption, the active area is blocked for the more reactive H_2SO_4 anions.

The concept of the described corrosion behavior can be applied to our PEO experiment. In 12.9 M, the breakdowns are exceptionally strong, whereas the breakdowns are suppressed in a mixture with 3% H_3PO_4. We assume that, during PEO, the preferential adsorption of H_3PO_4 anions blocks the anodic surface for H_2SO_4 anions, which tend to favor breakdowns instead of ion migration. Hence, destructive breakdowns and the related corrosion are suppressed, which directly reduces the mass loss in the process, as confirmed by our mass investigation in Figure 1b. Leach and Sidgwick proposed that the different behaviors of SO_4^{2-} and PO_4^{3-} are the result of their different molecular charges [22], which is plausible since the electrical field in PEO is exceptionally high.

Furthermore, the high H_3PO_4 anion adsorption to the anodic surface leads to the preferred incorporation of H_3PO_4 anions. This is in accordance with our EDX investigation, which reveals an increased concentration of phosphor species compared with the low sulfur concentration in the oxide. Similarly, earlier studies have confirmed that phosphorous or phosphate ions penetrate more easily through the titanium oxide layer during anodization compared with sulfur or sulfate ions [19]. Certainly, these phosphorous species contribute to the high mass gain in Figure 1b for electrolytes with additional H_3PO_4.

With the favored incorporation of H_3PO_4 anions, enhanced ion migration can be assumed, which increases the fraction of the ionic current. Because of the constant current mode in our process, the total current density always remains constant. When ionic migration is promoted, the total current in the process comprises less electronic current, i.e., breakdowns. Therefore, the additional H_3PO_4 reinforces the inhibition of breakdowns.

The reduced electronic current has a major impact on the oxide layer. According to the literature, two effects limit the lifetime of a discharge. On the one hand, the expansion of gases in the channel lead to cooling, and the plasma collapses [23]. On the other hand, the gas forms a bubble on top of the channel; thus, it increases the electrical resistivity of the channel and terminates the plasma [4,18]. The formation of a new plasma is prevented while the gas is inside and above the channel. When the gas escapes, the electrolyte fills the void [3]. As a consequence, the next discharge is created in the same channel. This hypothesis predicts that the current per channel per discharge is limited by the lifetime of the plasma channel.

According to our results, more charge compensation in the form of breakdowns occurs in pure H_2SO_4 compared with mixtures containing 1% or 3% H_3PO_4. As a consequence of the limited charge transfer per discharge in a single channel, more channels are necessary for higher charge compensation. Hence, the pore density increases compared with surfaces prepared in mixtures with 1% or 3% H_3PO_4, as shown in the SEM images in Figure 3. On the other hand, fewer channels for charge compensation by breakdowns are necessary in mixtures with H_3PO_4. Hence, the pore density decreases. However, the pore size increases in mixtures with H_3PO_4 because of recurring breakdowns in identical channels.

It should be noted that anatase is the predominant phase in the compact layer for all investigated samples. Previous studies confirm our conclusion that the thin compact layer is composed of nanocrystalline anatase [8,24]. The dense compact layer likely evolves from a temperature gradient [9]. The thermal mass of the titanium substrate enables the rapid cooling of the plasma. Hence, the time is too short and the temperature is too low for the phase transformation to rutile for an anatase-to-rutile transformation, and therefore, only a nanocrystalline anatase structure evolves. Also remarkable is the increased sulfur concentration in the compact layer, as seen in Figure 5. This may result from the electrolyte becoming trapped in interfacial nanopores during the fast cooling [14].

Another notable feature is apparent in the cross sections of several samples, which can be identified in our study in three ways. First, SEM cross section images, especially in Figure 4c, reveal a rather smooth morphology between the porous layer and the surface. Second, the EDX cross sections in Figures 5a,c show a different elemental composition compared with the porous layer in the previously mentioned region. Third, the Raman investigations in Figures 6a,c reveal a distinct change in the phase composition near the surface. We assume that this region originates from molten titanium, which is ejected from the channels and rapidly cools down in the vicinity of the electrolyte [25].

Because of quenching, oxide formation is suppressed, and consequently, oxide stoichiometry is not achieved. For this reason, we expect a predominant amorphous structure with small contributions of titanium dioxide phases.

5. Conclusions

Oxide coatings on titanium were produced in a galvanostatically controlled PEO process with a constant current density. With a concentrated 12.9 M H_2SO_4 electrolyte as the starting material, small amounts of H_3PO_4 were added to investigate the impact on oxide formation. Pure 12.9 M H_2SO_4 is highly suitable for promoting breakdowns. With a higher charge density, breakdowns cause a destructive reforming and induce the phase transition from predominantly anatase to almost entirely rutile. Upon reaching 35 C/cm^2, the rutile to anatase fraction is over 90%.

By adding small amounts of H_3PO_4, i.e., 1% or 3%, breakdown effects are drastically reduced. The rutile fraction in the process does not exceed 11%, even for charge transfers as high as 89 C/cm^2. The drastic change is explained by the preferential adsorption of H_3PO_4 anions to the anodic area. Therefore, the H_3PO_4 anions block the surface for more reactive H_2SO_4 anions and suppress breakdowns. The enhanced concentration of H_3PO_4 anions at the surface reinforces their incorporation and, consequently, migration in the oxide layer. Therefore, the ionic current in the process increases, and the electronic current fraction, including breakdowns, decreases. With fewer breakdowns, the destructive reforming diminishes. Moreover, the increase in ion migration promotes oxide formation with increased thickness and mass gain of the oxide layers, which are produced in mixtures with H_3PO_4.

Author Contributions: B.F. designed, conceived, and performed the confocal Raman microscopy; B.E. designed, conceived, and performed the other experiments; B.E. validated and analyzed the results; K.S. supervised the project; B.E. wrote the paper. All authors have read and agreed to the published version of the manuscript.

Funding: We acknowledge support by the Heinrich Heine University Duesseldorf. This research was also supported by Bundesministerium für Wirtschaft und Energie (BMWi) under project no. ZF4185502ZG6.

Acknowledgments: We gratefully thank Denis Netschitailo for supplementary PEO experiments and related discussions.

Conflicts of Interest: The authors declare no conflict of interest.

References

1. Diamanti, M.V.; Del Curto, B.; Pedeferri, M. Anodic oxidation of titanium: From technical aspects to biomedical applications. *J. Appl. Biomater. Biomech.* **2011**, *9*, 55–69. [CrossRef] [PubMed]
2. El Achhab, M.; Schierbaum, K. Gas sensors based on plasma-electrochemically oxidized titanium foils. *J. Sens. Syst.* **2016**, *5*, 273–281. [CrossRef]
3. Clyne, T.W.; Troughton, S.C. A review of recent work on discharge characteristics during plasma electrolytic oxidation of various metals. *Int. Mater. Rev.* **2018**, *64*, 1–36. [CrossRef]
4. Rakoch, A.G.; Khokhlov, V.V.; Bautin, V.A.; Lebedeva, N.A.; Magurova, Y.V.; Bardin, I.V. Model concepts on the mechanism of microarc oxidation of metal materials and the control over this process. *Prot. Met.* **2006**, *42*, 158–169. [CrossRef]
5. Yerokhin, A.; Nie, X.; Leyland, A.; Matthews, A.; Dowey, S. Plasma electrolysis for surface engineering. *Surf. Coat. Technol.* **1999**, *122*, 73–93. [CrossRef]
6. Hanaor, D.A.H.; Sorrell, C.C. Review of the anatase to rutile phase transformation. *J. Mater. Sci.* **2011**, *46*, 855–874. [CrossRef]
7. Engelkamp, B.; El Achhab, M.; Fischer, B.; Kökçam-Demir, I.; Schierbaum, K. Combined Galvanostatic and Potentiostatic Plasma Electrolytic Oxidation of Titanium in Different Concentrations of H_2SO_4. *Metals* **2018**, *8*, 386. [CrossRef]
8. Mortazavi, G.; Jiang, J.; Meletis, E.I. Investigation of the plasma electrolytic oxidation mechanism of titanium. *Appl. Surf. Sci.* **2019**, *488*, 370–382. [CrossRef]

9. Quintero, D.; Galvis, O.; Calderón, J.; Castaño, J.; Echeverría, F. Effect of electrochemical parameters on the formation of anodic films on commercially pure titanium by plasma electrolytic oxidation. *Surf. Coat. Technol.* **2014**, *258*, 1223–1231. [CrossRef]
10. Friedemann, A.; Gesing, T.; Plagemann, P. Electrochemical rutile and anatase formation on {PEO} surfaces. *Surf. Coat. Technol.* **2017**, *315*, 139–149. [CrossRef]
11. Schultze, J.; Lohrengel, M. Stability, reactivity and breakdown of passive films. Problems of recent and future research. *Electrochim. Acta* **2000**, *45*, 2499–2513. [CrossRef]
12. Barati Darband, G.; Aliofkhazraei, M.; Hamghalam, P.; Valizade, N. Plasma electrolytic oxidation of magnesium and its alloys: Mechanism, properties and applications. *J. Magnes. Alloy.* **2017**, *5*, 74–132. [CrossRef]
13. Galvis, O.; Quintero, D.; Castaño, J.; Liu, H.; Thompson, G.; Skeldon, P.; Echeverría, F. Formation of grooved and porous coatings on titanium by plasma electrolytic oxidation in H_2SO_4/H_3PO_4 electrolytes and effects of coating morphology on adhesive bonding. *Surf. Coat. Technol.* **2015**, *269*, 238–249. [CrossRef]
14. Kern, P.; Zinger, O. Purified titanium oxide with novel morphologies upon spark anodization of Ti alloys in mixed H_2SO_4/H_3PO_4 electrolytes. *J. Biomed. Mater. Res.* **2007**, *80A*, 283–296. [CrossRef]
15. Spurr, R.A.; Myers, H. Quantitative analysis of anatase-rutile mixtures with an X-ray diffractometer. *Anal. Chem.* **1957**, *29*, 760–762. [CrossRef]
16. Fadl-Allah, S.A.; El-Sherief, R.M.; Badawy, W.A. Electrochemical formation and characterization of porous titania (TiO2) films on Ti. *J. Appl. Electrochem.* **2008**, *38*, 1459–1466. [CrossRef]
17. Balachandran, U.; Eror, N.G. Raman spectra of titanium dioxide. *J. Solid State Chem.* **1982**, *42*, 276–282. [CrossRef]
18. Troughton, S.C.; Nominé, A.; Nominé, A.V.; Henrion, G.; Clyne, T.W. Synchronised electrical monitoring and high speed video of bubble growth associated with individual discharges during plasma electrolytic oxidation. *Appl. Surf. Sci.* **2015**, *359*, 405–411. [CrossRef]
19. Lee, J.H.; Kim, S.E.; Kim, Y.J.; Chi, C.S.; Oh, H.J. Effects of microstructure of anodic titania on the formation of bioactive compounds. *Mater. Chem. Phys.* **2006**, *98*, 39–43. [CrossRef]
20. Abdel Hady, Z.; Pagetti, J. Anodic behaviour of titanium in concentrated sulphuric acid solutions. Influence of some oxidizing inhibitors. *J. Appl. Electrochem.* **1976**, *6*, 333–338. [CrossRef]
21. Prando, D.; Brenna, A.; Diamanti, M.V.; Beretta, S.; Bolzoni, F.; Ormellese, M.; Pedeferri, M. Corrosion of titanium: Part 2: Effects of surface treatments. *J. Appl. Biomater. Funct. Mater.* **2018**, *16*, 3–13. [CrossRef]
22. Leach, J.S.L.; Sidgwick, D.H. Anodix oxidation of Titanium. *Metall. Corrosion Proc.* **1981**, *1*, 82–85.
23. Klapkiv, M.D. Simulation of synthesis of oxide-ceramic coatings in discharge channels of a metal-electrolyte system. *Mater. Sci.* **1999**, *35*, 279–283. [CrossRef]
24. El Achhab, M.; Erbe, A.; Koschek, G.; Hamouich, R.; Schierbaum, K. A microstructural study of the structure of plasma electrolytically oxidized titanium foils. *Appl. Phys. A* **2014**, *116*, 2039–2044. [CrossRef]
25. Mohedano, M.; Lu, X.; Matykina, E.; Blawert, C.; Arrabal, R.; Zheludkevich, M. Plasma electrolytic oxidation (PEO) of metals and alloys. *Encycl. Interfacial Chem.* **2018**, *6*, 423–438.

3 Oxygen Sensing

In the following section, the general oxygen adsorption on TiO_2 is addressed, followed by a discussion of the oxygen adsorption on Pt/TiO_2 structures. Finally, the relevance of electroforming for the subsequent study is considered.

3.1 Oxygen Adsorption

In ambient atmosphere, the adsorption of gases strongly affect the electronic properties of semiconducting n-type TiO_2. Most prominent is the impact of molecular oxygen and will be briefly described in the following.

In the first step of adsorption, molecular oxygen adsorbs physically on the surface. The physisorption is considered to be too weak to have a significant effect on the electronic structure of the adsorbent, therefore, the molecule is usually highly mobile in the plane parallel to the surface. On the defect-free rutile TiO_2 (110)-surface, the adsorption occurs preferentially at undercoordinated Ti_{5c} atoms and the mobility is enhanced along the [001] direction in between the protruding O rows [127]. At these sites, a strong adsorbate bonding occur, which is known as chemisorption. The term indicates the close relation to a chemical reaction. Indeed, the bonding resembles the formation of covalent or ionic bonds in molecular physics [128].

Herein, a decisive electron transfer from the conduction band (CB) of TiO_2 to the oxygen molecule can take place. As a result, a molecular ion O_2^- forms. In a further step, the molecular ion may accept another electron from the oxide, forming the peroxide ion O_2^{2-}. It commonly acts as intermediate and dissociate to form two atomic ions, i.e. O^-. In general, the ions can be regarded as free oxygen ions without local chemical bond, which are electrostatically stabilized in the vicinity of the surface. Due to the strong ionic character, the adsorption of the oxygen is commonly referred to as ionosorption. However, the exclusive ionic nature of the adsorbates is controversial [129], which will be discussed in the end of this section.
In addition to the oxygen species outlined above, a doubly charged atomic oxygen ion, O^{2-}, can be formed. It is identical to the lattice oxygen ions and, therefore, preferentially incorporate and diffuse into the TiO_2 lattice. Table 3.1 summarizes the possible equilibrium states of adsorbed oxygen on TiO_2.

$O_2\,(gas) \longleftrightarrow O_2\,(ads)$	Physisorption
$O_2\,(ads) + e^-\,(CB) \longleftrightarrow {O_2}^-\,(ads)$	Ionosorption
${O_2}^-\,(ads) + e^-\,(CB) \longleftrightarrow {O_2}^{2-}\,(ads) \longleftrightarrow 2\,O^-\,(ads)$	Ionosorption
$O^-\,(ads) + e^-\,(CB) \longleftrightarrow O^{2-}\,(ads)$	Ionosorption
$O^{2-}\,(ads) \longleftrightarrow O^{2-}\,(bulk)$	Incorporation & Diffusion

Table 3.1: Possible equilibrium states of adsorbed oxygen with nomenclature. Adapted with permission from [130]. © Springer.

The prevailing oxygen species on the TiO_2 surface depends on the temperature and the structure of the surface, including point defects. Henderson et. al reported that O_2^-, formed on the rutile TiO_2(110)-surface below 150 K, is stable until 410 K [82]. Above, it desorbs as molecular oxygen. Furthermore, the formation of O_2^- has been shown to be strongly promoted by oxygen vacancy sites at the surface. In fact, the authors report that each surface oxygen vacancy is responsible for binding up to three oxygen molecules at 150 K [82]. These findings experimentally support that donated electrons from oxygen vacancies are not localized at the defect site. At temperatures above 150 K, the dissociation of oxygen molecules start to prevail [82]. The dissociation is further promoted by surface defects. On bridging oxygen vacancy sites, V_{br}, molecular oxygen readily dissociates, filling a vacancy site and forming an oxygen adatom. Without considering the charge, the equilibrium is

$$O_2\,(gas) + V_{br} \rightleftharpoons O_{br} + O\,(ads) \quad . \tag{3.1}$$

At room temperature, the oxygen dissociation is not limited to oxygen vacancy sites: A STM study from Wendt et al. indicate that oxygen dissociation also occurs at non-vacancy sites [71]

$$O_2\,(gas) \rightleftharpoons 2\,O\,(ads) \quad . \tag{3.2}$$

Furthermore, these authors propose that subsurface titanium interstitials promote the oxygen dissociaton at non-vacancy sites. It is argued that these subsurface donor-sites largely affect the surface chemistry, for instance by providing the electronic charge required for oxygen adsorption and dissociation. However, other authors attribute the oxygen dissociation on non-vacancy sites to the delocalized charge of ionized surface vacancies [73].

In general, charged oxygen adsorbates represent a negative charge on the surface, which is compensated by a positive charge in the semiconductor. The positive charge origins from the donating core atoms in the electron depleted layer. Thus, the local electrical conductivity, which is controlled by the density of electrons, is decreased near the surface with respect to its bulk value. Furthermore, the charge distribution leads to a band bending eV in the electronic band structure with a maximum value of eV_S at the surface. In case of a strong band bending, i.e., $|eV_S| \gg kT$, the charge distribution can be approximated by a step function with the charge density en_D (Schottky approximation). By solving Poisson's equation, the potential

$$\phi(z) = \phi_b - \frac{en_D}{2\epsilon\epsilon_0}(z + z_0)^2 \qquad 0 \le z \le z_0 \tag{3.3}$$

is concluded, where $z = 0$ indicates the surface and $z = z_0$ is the width of the depleted layer. ϕ_b represents a potential in the bulk. The maximum band bending relative to the bulk level is determined from

$$V_S = \phi(0) - \phi_b = -\frac{e n_D {z_0}^2}{2\epsilon\epsilon_0} \quad . \tag{3.4}$$

With the assumption that n_D is controlled by the density of ionosorbed oxygen, the band bending depends on the oxygen adsorption.

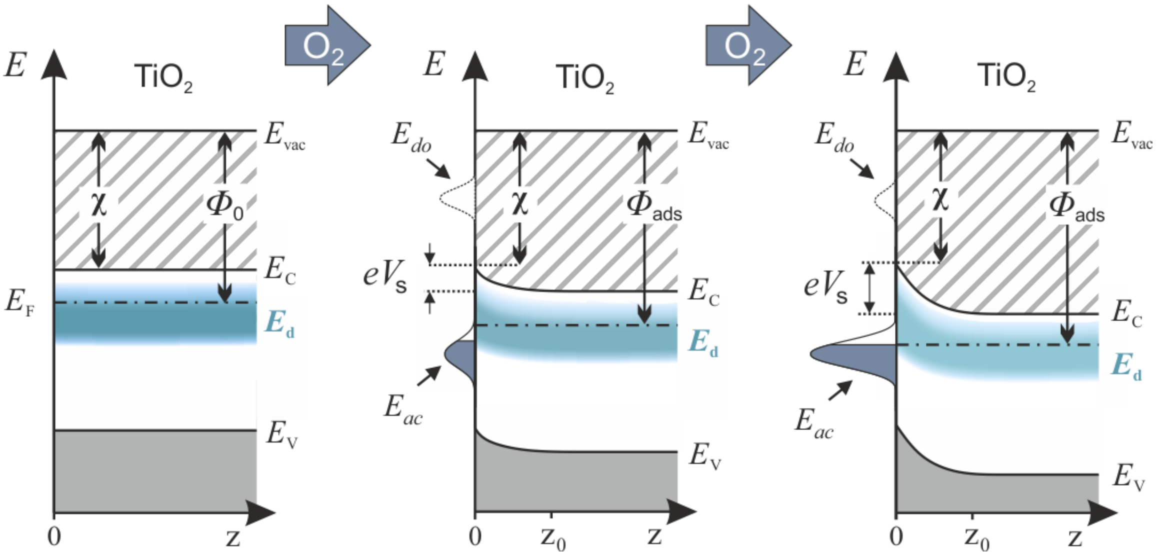

Figure 3.1: The effect of oxygen ionosorption on the electronic band structure of n-type TiO_2. On the left, the band structure corresponds to a situation without (oxygen) acceptor adsorbates. When oxygen is provided the band bending on the surface, eV_S, progressively increases with the surface density of acceptor adsorbates. Further explanation of the reaction and quantities can be found in the text.

In Fig. 3.1 the impact of oxygen adsorption on the band structure is illustrated. Herein, E_{do} and E_{ac} indicate donator and acceptor surface states, respectively, while E_{d} marks the defect band. E_{Vac} denotes the vacuum energy, E_{C} the minimum of the conduction band and E_{V} the maximum of the valence band. Φ_0 and Φ_{ads} are the work functions before and after oxygen adsorption. To be precise, the work function of a semiconductor is the sum of the internal work function (bulk $E_C - E_F$), a component for the band bending (eV_S) and the electron affinity (χ) as external work function:

$$\Phi_{\mathrm{ads}} = \Phi_0 + eV_S = \chi + eV_S + (E_C - E_F)_B \quad . \tag{3.5}$$

The Fermi energy E_F for the bulk does not change relative to E_C, unless bulk incorporation and diffusion occur. Changes in the electron affinity χ are based on the formation or degradation of dipoles and are not expected for the ideal oxygen ionosorption [130]. Thus, for ideal oxygen ionosorption, the work function follows only the change in the band bending ($\Delta\Phi = \Delta eV_S$).

In practice, changes in the electron affinity on oxygen exposure occur. Sahm et al. carried out simultaneous resistance and work function measurements on undoped

SnO_2 at 200 °C and 400 °C [131]. According to the results, χ does not change significantly at 400 °C, but a distinctive decrease was observed at 200 °C. The authors concluded that at higher temperatures mainly ionic oxygen species occur, however, neutral oxygen molecules undergo a dipolar interaction with the SnO_2 surface at 200 °C [131]. Transferred to TiO_2, it has to be assumed that oxygen adsorption below 200 °C is not limited to pure ionosorption and that neutral oxygen molecules affect surface properties to an unknown extent.

3.2 Pt/TiO_2 Junction

First, the ideal Pt/TiO_2 junction will be briefly described, followed by the surface-state controlled Pt/TiO_2 junction.

When the semiconducting n-type TiO_2 is in contact with metallic Pt, conduction band electrons from titanium will be transferred to the platinum conduction band until an equilibrium is reached. The electron transfer can be traced experimentally with XPS by the decrease of Ti^{3+}-derived intensities during deposition of platinum [33]. Energetically, it is an alignment of the Fermi energies, which is due to the different work functions. Nowotny et al. averaged TiO_2 and Pt work functions of several reports and crystallographic planes to provide the energy range

$$2.9\,\mathrm{eV} < \Phi_{\mathrm{TiO_2}} < 3.2\,\mathrm{eV} \quad , \tag{3.6}$$

$$5.12\,\mathrm{eV} < \Phi_{\mathrm{Pt}} < 5.93\,\mathrm{eV} \quad , \tag{3.7}$$

respectively [132]. Due to the electron transfer, a depletion of charge carriers in TiO_2 occur near the metal. The stationary ionized donors form a positive space charge, while the electron accumulation in Pt represents a negative space charge. The width of the space charge layer in Pt is negligible, due to the high charge carrier density. In the n-type semiconductor, the width of the depletion layer d_{n} depends on the defect donor concentration n_{D} according to

$$d_{\mathrm{n}} = \sqrt{\frac{2\epsilon\epsilon_0}{e n_{\mathrm{D}}} \left(\Phi_{\mathrm{Pt}} - \Phi_{\mathrm{TiO_2}}\right)} \quad , \tag{3.8}$$

where ϵ is the relative permittivity in TiO_2 and ϵ_0 is the permittivity in vacuum, respectively. Similar to the before mentioned oxygen adsorption, the charge distribution leads to a band bending eV. The band structure at equilibrium conditions is sketched in Fig. 3.2. The energetic difference between E_{F} and the maximum band bending value is

$$\Phi_{\mathrm{SB}} = eV_{\mathrm{S}} + E_C - E_F = \Phi_{\mathrm{Pt}} - \chi \quad , \tag{3.9}$$

where Φ_{SB} is known as Schottky barrier.

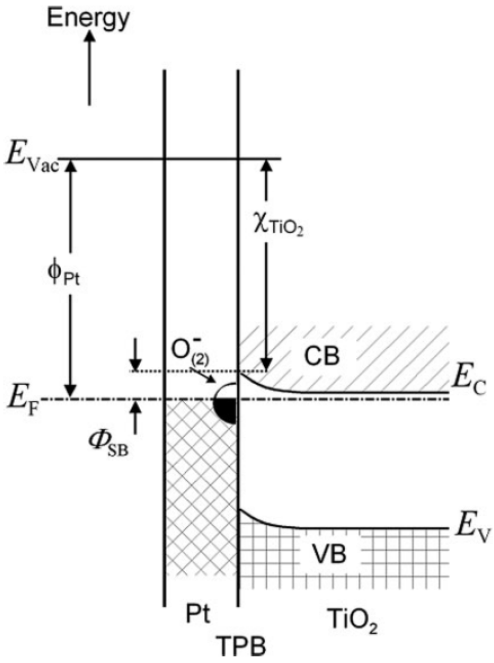

Figure 3.2: Simplified electronic band structure of the Pt/TiO_2 junction with oxygen acceptor adsorbates. Further explanation of the quantities can be found in the text. Reprinted with permission from [62]. © (2011) John Wiley and Sons.

In general, the electron transport from Pt to TiO_2 requires that the electron have to overcome Φ_{SB}. Due to the high energetic barrier, the electron transport from Pt to TiO_2 is largely suppressed. In the forward direction, electrons can penetrate the metal from the semiconductor side by overcoming eV_S. Due to the different ratios, the Pt/TiO_2 exhibit rectifying properties. By applying an external voltage U, eV_S can be changed. Due to the low charge carrier density in the depleted TiO_2, it can be assumed in a good approximation that an applied voltage drops completely across the depletion layer. Thus, the band structure in Fig. 3.2 changes only within the space charge layer. With an uplift in the potential on the TiO_2 site (relative to Pt), the potential energy of the electrons decreases and consequently the band bending increases ($eV_S + U$). In contrast, lowering the potential on the TiO_2 site leads to a decrease in band bending ($eV_S - U$). For the latter case (forward direction), the current I as a function of the applied voltage V is

$$I(V) = \left\{A\,A^*\,T^2 \exp\left(-\frac{e\Phi_{SB}}{kT}\right)\right\}\left\{\exp\left(\frac{e(V-IR)}{kT}\right)-1\right\} \quad , \tag{3.10}$$

$$I(V) = I_S\left\{\exp\left(\frac{e(V-IR)}{kT}\right)-1\right\} \quad . \tag{3.11}$$

Hereby, A is the Schottky contact area, A^* is the Richardson constant, T is the temperature, e is the elementary charge, k is the Boltzmann constant, R is the internal resistance, n is the ideality factor, and I_S is the saturation current.

It should be pointed out, that the fundamental charge transfer, due to oxygen ionosorption or platinum coverage, applies only for semiconducting n-type TiO_2. In the defect-free TiO_2, mobile charge carriers are missing. UPS measurements for small coverages of Pt on defect-free $TiO_2(110)$ indicated no change in band bending, so the formation of a space charge layer was excluded [33]. Instead, a decrease in electron affinity χ was found, which can be attributed to dipoles with their positive pole pointing away from the surface [33].

Surface-state Controlled Pt/TiO_2 Junction

In practice, the metal/semiconductor junction often deviates from the theoretical considerations in the last section. In contrast to equation (3.9), it is often found that Φ_{SB} is almost independent of the work function of the metal [133]. In general, this is due to the dominant influence of atmospheric oxygen. As mentioned before, the essential charge transfer for band bending can be induced by oxygen or platinum adsorption. For an atom area density at the interface of 10^{12}–$10^{14}\,\mathrm{cm}^{-2}$, the charge transfer from gas adsorption can reach a similar order of magnitude compared to metal adsorption [133, 134]. For comparison, one adsorbed oxygen species per titanium surface atom on the rutile $TiO_2(110)$ surface corresponds to a density of $1.48 \times 10^{15}\,\mathrm{cm}^{-2}$ [135]. Therefore, it is assumed that a low coverage is sufficient to induce a similar or even greater acceptor effect by oxygen adsorbates compared to metallic adsorbates. When the density of oxygen induced interface states is high, e.g. $10^{15}\,\mathrm{eV}^{-1}\,\mathrm{cm}^{-2}$, it will practically pin E_F at the high density of states (Fermi level pinning) [134]. As a consequence, additional surface charge, e.g., due to the contact with platinum, is compensated by surface states charge and has barely an impact on the space charge layer. In the band structure in Fig. 3.2, the pinning is indicated by the alignment of the occupied level of adsorbate induced surface states with E_F. Such a contact, which is mainly determined by the energy and the spatial distribution of extrinsic interface states at the semiconductor surface, is described as *surface-state controlled Schottky junction* [62]. Prerequisite is that the oxygen-induced surface states remain stable during metal deposition. An easily accessible concept assumes that Pt/O_2/TiO_2 three-phase boundaries (TPB) exist at which charge transfer occur.

In the ideal metal/semiconductor junction, an applied voltage directly affect the band bending ($eV_S \pm U$). The oxygen-induced interface states attenuate this effect and only $1/n$ of the applied voltage affect the band bending [33]. n is called the ideality factor, which can be considered as parameter for the density of acceptor states. At high oxygen partial pressure, i.e. 10^4 Pa, n becomes very large and eV_S barely change with the applied voltage. The current function in equation (3.11) slightly changes for an surface-state controlled Schottky junction to

$$I(V) = I_S \left\{ \exp\left(\frac{e(V - IR)}{nkT} \right) - 1 \right\} \quad . \tag{3.12}$$

Schierbaum et al. investigated Pt/TiO_2 contacts for different oxygen partial pressures at 500 K and determined the ideality factor n and Schottky barrier Φ_{SB}. Characteristic I–V data is shown in Fig. 3.3. Additional functions were fitted to the data, which either take n into account or not. It is evident that the consideration of n is already necessary at low oxygen partial pressures for an adequate description of the data.

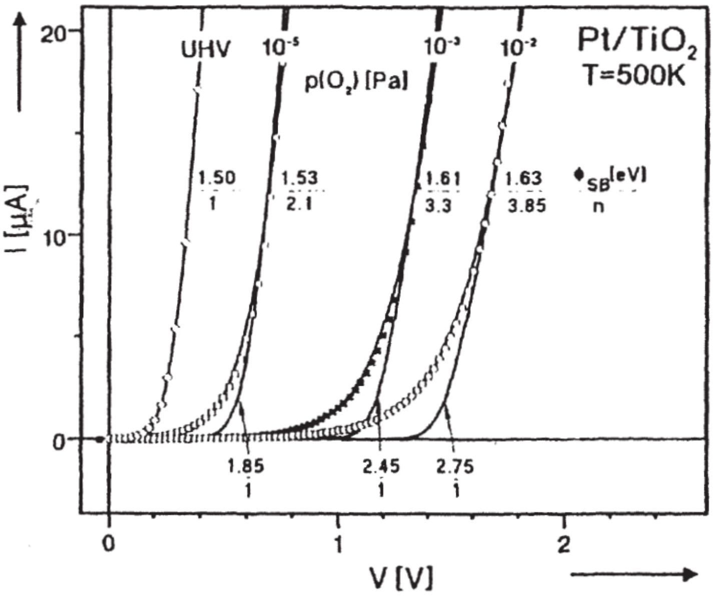

Figure 3.3: I–V curves of polycristalline Pt/TiO$_2$ in UHV and for different oxygen partial pressures at 500 K. The data were fitted and the Schottky barrier Φ_{SB} and the ideality factor n were determined. When n=1 is used, the calculated curves differ significantly from the data recorded in oxygen atmospheres. Figure reprinted with permission from [32]. © (1993) Springer Nature.

3.3 Electroforming in PEO-TiO$_2$

On the one hand, a change in the ambient atmosphere composition may lead to a change in the defect concentration in TiO$_2$. On the other hand, the defect concentration can also be influenced by a sufficiently high electric field. The field-induced structural change is often referred to as electroforming (EF). While EF is commonly exploited for switching in memory-resistors, it can also create an undesired baseline drift in gas sensing.

In oxides, the effect mainly applies to positively charged oxygen vacancies, $\mathrm{V_O}$. The location, distribution, and the concentration of $\mathrm{V_O}$ determines the electrical properties of the bulk and at the interface. It is widely believed that the current in the bulk TiO$_2$ is carried along conducting channels, also referred to as filaments. These channels form in the presence of an electric field by the alignment of vacancies to extended defects (e.g. grain boundaries) [45]. A continuous electric field can redistribute vacancies and may modify, create, or annihilate conducting channels in the bulk. When these channel are situated at interfaces, they may control the current transport across the interfaces. In a Pt/TiO$_2$/Ti sandwich structure, both interfaces may be affected. When a positive potential is applied to Pt (forward direction), positively charged

V_O are pushed away from the Pt/TiO_2 interface. Therefore, the rectifying Schottky barrier remains stable [136]. When a corresponding negative potential is applied to the titanium substrate, vacancies accumulate at the Ti/TiO_2 interface, causing an ohmic contact [136].

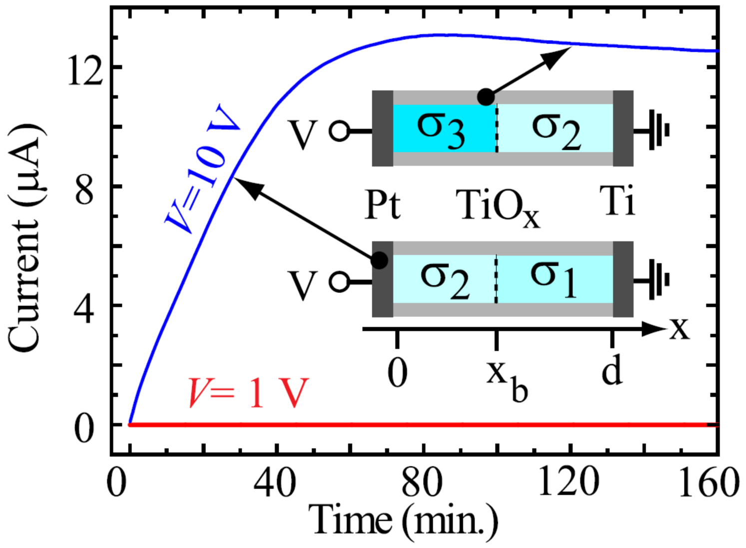

Figure 3.4: Time dependent current in a Ti/PEO-TiO_2/Pt structure at 1 V and 10 V forward voltages. Prior to the voltage application at t=0 min, oxygen vacancies were accumulated at the Pt/PEO-TiO_2 interface. The inset shows a single channel model with $\sigma_3 < \sigma_1 < \sigma_2$. In the early stage, the phase 2 expanse at the expense of phase 1. Later on, phase 3 starts to grow from the Pt/TiO_2 interface, leading to a decrease in net conductivity from t=80 min onward. Figure reprinted with permission from [137]. © (2015) AIP Publishing.

The dynamics in PEO-TiO_2 structures has been investigated by Strungaru et al., who showed that under certain conditions PEO-TiO_2 structures are highly affine to EF [137]. Figure 3.4 shows results from DC-measurements on Pt/TiO_2/Ti sandwich structures. Before each measurement, the Pt/TiO_2 interface was enriched with oxygen vacancies. When applying a voltage below 2 V, the current does not significantly changes with time and, consequently, no EF was assumed. When repeating the measurement with 10 V (blue curve), a distinct increase, followed by a slight decrease could be detected. A high current is not unexpected, since the current growth exponentially with the applied forward voltage, according to equation 3.12. Remarkable is the duration in which the current reaches a maximum value. The authors attribute it to the field-supported migration of vacancies from the Pt/TiO_2 interface into the bulk TiO_2. In the concept of a single conducting channel in the inset of Fig. 3.4, the initial conductivity in the channel is σ_1 and with the enrichment of vacancies the conductivity changes to the higher value σ_2. The subsequent decrease in the current after 80 min is attributed to the continuous migration of vacancies and progressive depletion near the Pt/TiO_2 interface. This progress is represented by the growth of the σ_3 phase with $\sigma_3 < \sigma_2$.

As an additional result, Strungaru et al. found that the progression of EF occurs faster when the interface is exposed to H_2 compared to an exposure to pure N_2.

In general, EF may also affect the following investigation on oxygen sensing with Pt/PEO-TiO_2. The applied voltage in the following investigation was about 3 V with a comparable oxide thickness to the samples in the aforementioned study. The voltage is slightly above the proposed threshold value of 2 V for electroforming. Therefore, a slight long-term drift in the signal due to EF could occur. However, in contrast to the presented study, no pre-arranged vacancy distribution was created before the measurement. In addition, the time before oxygen exposure was chosen sufficiently large so that a nearly constant signal was obtained, which indicates quasi-equilibrium conditions within the given time scale. Therefore, significant effects of EF on the oxygen sensing performance in the following investigation is not expected.

P.III Oxygen Sensing of Pt/PEO-TiO_2 in Humid Atmospheres at Moderate Temperatures

Publication Reference

[43]:

B. Engelkamp, and K. Schierbaum, *Oxygen Sensing of Pt/PEO-TiO_2 in Humid Atmospheres at Moderate Temperatures* Sensors **2021**, 21(7), 2558.
doi:10.3390/s21072558

Copyright statement

Author Contributions

Conceptualization, B.E. and K.S.; formal analysis, B.E.; investigation, B.E.; data curation, B.E.; writing—original draft preparation, B.E.; writing—review and editing, B.E. and K.S.; visualization, B.E.; supervision, K.S.

sensors

Article

Oxygen Sensing of Pt/PEO-TiO_2 in Humid Atmospheres at Moderate Temperatures

Bernd Engelkamp * and **Klaus Schierbaum**

Abteilung für Materialwissenschaft, Institut für Experimentelle Physik der Kondensierten Materie, Heinrich-Heine-Universität Düsseldorf, Universitätsstraße 1, 40225 Düsseldorf, Germany; klaus.schierbaum@hhu.de
* Correspondence: bernd.engelkamp@hhu.de; Tel.: +49-211-81-15256

Abstract: Here, we show that the presence of adsorbed water improves the oxygen-sensing properties of Pt/TiO_2 at moderate temperatures. The studied interface is based on porous plasma electrolytic oxidized titanium (PEO-TiO_2) covered with platinum clusters. The electrical resistance across Pt/PEO-TiO_2 is explained by an electronic depletion layer. Oxygen adsorbates further increase the depletion by inducing extrinsic interface states, which are occupied by TiO_2 conduction band electrons. The high oxygen partial pressure in ambient air substantially limits the electron transport across the interface. Our DC measurements at defined levels of humidity at 30 °C show that adsorbed water counteracts this shortcoming, allowing oxygen sensing at room conditions. In addition, response and recovery times from temporal oxygen exposure decrease with humidity. We attribute the effects to competing adsorption processes and reactions of water with adsorbed oxygen species and/or lattice oxygen, which involve electron re-injection to the TiO_2 conduction band. Elevated temperatures up to 170 °C attenuate the effects, presumably due to the lower binding strength to the surface of molecular water compared with oxygen adsorbates.

Keywords: plasma electrolytic oxidation; titanium dioxide; Pt/TiO_2; ionosorption; oxygen gas sensor

check for updates

Citation: Engelkamp, B.; Schierbaum, K. Oxygen Sensing of Pt/PEO-TiO_2 in Humid Atmospheres at Moderate Temperatures. *Sensors* **2021**, *21*, 2558. https://doi.org/10.3390/s21072558

Academic Editor: Mikhael Bechelany

Received: 12 March 2021
Accepted: 3 April 2021
Published: 6 April 2021

1. Introduction

Titanium dioxide is commonly investigated as gas sensing material [1]. For this purpose, TiO_2 is mainly used in chemoresistive gas sensors, where electrical properties are determined as functions of the ambient gas [2]. The performance highly depends on the morphology of the gas sensing material. In general, porous TiO_2 with a large surface-to-volume ratio provides many active sites for adsorption, which is essential for high sensitivity [3,4]. In this respect, plasma electrolytic oxidized titanium (PEO-TiO_2) with high porosity was already proved to be suitable for the detection of H_2, H_2O and CO [5].

The conceptual setup follows a sandwich structure with a permeable top electrode, PEO-TiO_2 and titanium substrate as the bottom electrode. The top electrode often contains platinum as a catalytically active metal. Due to work function differences between Pt and the n-type TiO_2, an electronic depletion within the TiO_2 is formed. The charge distribution induces band bending, which represents a rectifying resistance for electronic charge transport across the interface. Analogously, chemisorbed gases at three phase boundaries (TPBs), i.e., gas/Pt/TiO_2, affect the depleted layer [6]. In case of oxidzing adsorbates, conduction band electrons from TiO_2 are localized in extrinsic surface states. Therefore, the depletion in TiO_2 increases and ultimately controls the interface resistance. The fundamental mechanism is often referred to as acceptor-type chemisorption or ionosorption [6,7]. Herein, the most prominent acceptor gas in ambient air is oxygen. The net reaction

$$O_2 + V_{ads} + e^- \rightleftharpoons O^-_{2\ ads} \tag{1}$$

indicates the ionosorption of molecular oxygen with $O^{-}_{2\ ads}$ as the ionosorbed molecule; V_{ads} represents a free adsorption site at an undercoordinated surface titanium atom. By dissociation and further electron acceptance, an atomic species forms according to the reaction

$$O^{-}_{2\ ads} + V_{ads} + e^{-} \rightleftharpoons 2O^{-}_{ads}. \tag{2}$$

The nature of the ionosorbed species is assumed to depend on the adsorption temperature and the substrate [7]. A dissociative adsorption of molecular oxygen at catalytically active platinum and the subsequent spill-over effect to TiO_2 promote the accumulation of atomic ionosorbed oxygen [6]. In sum, the surface density of ionosorbed oxygen controls the major contribution to the band bending. One approach to exploit this effect for oxygen sensing is to apply a forward voltage, which decreases the band bending and promotes an electronic current across the Pt/TiO_2 interface. Due to the exponential I–V relation, a highly sensitive current signal in dependence of the oxygen adsorbates is expected.

In general, the effect is conceivable for the operation of a sensor at room temperature. This is in contrast with many conventional chemoresistive sensors based on semiconducting metal oxides, where the change in resistance is mainly caused by the alteration in lattice point-defect concentrations. Therefore, high operating temperatures are essential to attain defect equilibriums at appropriate time scales [8]. At low temperatures (e.g., below 200 °C), the dynamics of lattice point defects can be neglected and the change in resistance is mainly attributed to the effect of reactive adsorbates. For instance, an early study at low pressures showed that the Pt/TiO_2(110) interface is sensitive to low partial pressures of oxygen (e.g., $\Delta p = 10^{-3}$ Pa) at 130 °C [9].

However, there are two major problems to overcome to use the effect for oxygen gas sensors. First, high oxygen partial pressures are problematic. At room atmosphere, the surface is almost saturated with adsorbed oxygen. Thus, the high surface density of ionosorbed oxygen prevents almost any current across the Pt/TiO_2 interface. In addition, small deviations in the relatively high oxygen partial pressure have a rather small impact on the band bending. Second, the cross-selectivity to other reactive gases must be respected. Water vapor has presumably the most prominent role in ambient air. Even in vacuum experiments, water adsorption from residual water on defective TiO_2 is inevitable. Contrary to the effect of oxygen adsorbates, adsorbed water showed an electron donor effect on semiconducting metal oxides [10]. Although it is frequently used for humidity sensors, a non-constant concentration of adsorbed water interferes with oxygen detection [11,12]. In addition, the direct interaction of adsorbed oxygen species and water molecules or water derived species represents an additional step in complexity [13].

However, we show that oxygen detection with Pt/PEO-TiO_2 can also benefit from the presence of water. Therefore, we investigated the current across the Pt/PEO-TiO_2 interface as a function of the oxygen concentration and relative humidity. From the results, the reactions of oxygen and water on the surface are considered.

2. Materials and Methods

PEO preparation is extensively described and analyzed in previous studies [14,15] and is only briefly explained here. Titanium samples with 125 µm thickness were plasma electrolytic oxidized in 75 wt % sulphuric acid. The galvanostatic operation mode is limited to 55 mA/cm^2 and is stopped at a charge density of approximately 42 C/cm^2, which roughly corresponds to 145 V. After treatment, the sample was rinsed in deionized water and dried in air.

X-ray photoelectron spectra were recorded with Al Kα radiation with a beam diameter around 100 µm and energy resolution of 0.5 eV (PHI 5000 VersaProbe II, Physical Electronics Inc., Chanhassen, MN, USA). The residual pressure was about 10^{-8} mbar. Binding energies refer to the C 1s peak at 284.8 eV. For the deconvolution of the O 1s core level peak a multi peak fit with "Voigt" profiles and a "Tougaard" background was used. Water adsorption/desorption isotherms of PEO-TiO_2 were recorded with a humidity-controlled thermobalance (Q5000 SA, TA instruments Inc., New Castle, DE, USA) with time intervals of 40 min and 5% steps in relative humidity (r.h.) Before the measuring, the PEO-TiO_2 was mechanically separated from the titanium substrate.

A single sample for the present study had an area of $3 \times 3\,mm^2$. Two platinum areas of $1.4\,mm^2$ and approximately 100 nm thickness were sputtered onto PEO-TiO_2 at room temperature. The spacing between the two areas was 0.6 mm. Underneath one of them, the TiO_2 surface was scratched before sputtering to obtain an ohmic contact to the titanium. Electrical contacts were realized by gold-wire bonding to the platinum areas. The operating temperature was regulated by means of a platinum microheater directly below the sensor material and an RTD Pt1000. The electrical current was measured with a PXI-4071 DMM (National Instruments Corp., Austin, TX, USA). The resolution in DC current operation was below 10 nA in the measurement range of 10 mA.

The gas sensing experiments were performed in a gas-flow apparatus. Nitrogen 5.0 and oxygen 6.0 functioned as the inert carrier gas and test gas, respectively. Nitrogen was additionally purified by oxygen and humidity gas filters (CP17970 and CP17971, Varian Inc., Palo Alto, CA, USA). Two mass flow controllers (MFCs, F-201CV, Bronkhorst Deutschland Nord GmbH, Kamen, Germany) regulated the ratio between O_2 and N_2. An equivalent MFC was used to adjust the flow of water vapor saturated N_2, corresponding to 100% r.h. The total flow was kept constant at 100 ml/min. The investigation of different levels of r.h. started in a dry nitrogen flow. Initially, the sample was heated for one hour to approximately 120 °C to decrease the amount of adsorbed water. Before each measurement, a minimum time interval of 10 h at a constant level of humidity was applied to ensure a quasi-equilibrium with the water vapor. The microstructure of the platinum covered oxide layer was investigated by field emission scanning electron microscopy (SEM; JSM-7500F, JEOL Ltd., Tokio, Japan).

3. Results and Discussion

Figure 1a shows an electron microscope image of the porous PEO-titanium covered by platinum. The porosity with distinct fissures and unevenly distributed, inhomogeneous pores is apparent. The rough surface texture of the structure originates from the platinum coverage and indicates the formation of platinum clusters. Previous XRD investigations revealed a dominant rutile fraction of 93.7%, with the (110) surface showing the highest intensity contribution [15]. This dominance is presumably explained by the thermodynamically lowest surface energy compared to other rutile surfaces [16]. For this reason, we refer in the following discussion to some concepts from the well-researched TiO_2 rutile (110) surface.

3.1. Water Adsorption on PEO-TiO_2

Due to the relevance of humidity effects on metal oxide-based gas sensors, we first focus on the water adsorption on PEO-TiO_2 at constant levels of relative humidity (r.h.) Although a weak external electrical field is generated by the applied voltage in our experimental setup, we did not expect any noticeable effect on the water adsorption behavior, since at the given magnitude, the intrinsic field largely controls the adsorption [17]. It is generally accepted that the water adsorption on TiO_2 can be described within the concept of multilayer adsorption [11,18,19]. Basic requisite for multilayer adsorption is the formation of an innermost layer. This layer strongly depends on the molecular structure of the TiO_2 surface and defines whether a hydrophobic or hydrophilic surface is formed [20]. Typically, the innermost layer consists of hydroxyl groups formed by water dissociation, although molecular water with rigid mobility may occur [11,19]. Previous studies showed that dissociative adsorption is highly promoted by surface defects and steps [21]. Given the PEO-TiO_2 surface, with its large density of defects and steps, we assumed an initial dissociative water adsorption to occur even at room temperature. Figure 1b shows a spectra including the O 1s binding energies determined with X-ray photoelectron spectroscopy on PEO-TiO_2 at room temperature. The deconvolution of the data reveals two peaks. The first peak is assigned to O^{2-}, i.e., mainly lattice oxygen, while the second peak origins from OH groups [22]. A third peak due to H_2O adsorbates would be expected around 532.5–532.7 eV and can not be determined in our spectra [22]. This qualitatively confirms that OH groups predominate over H_2O adsorbates at around 10^{-8} mbar.

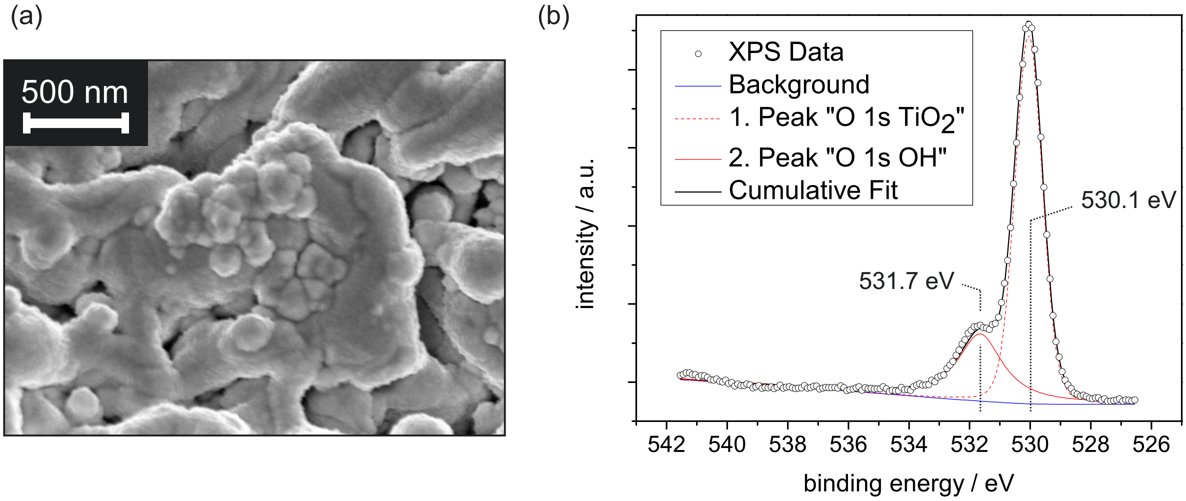

Figure 1. (**a**) SEM image of the Pt/PEO-TiO_2 surface. (**b**) XPS spectra of the O 1s binding energy range for the PEO-TiO_2 sample at room temperature. The first peak is centered around 530.1 eV and is assigned to O^{2-}, while the second peak is centered around 531.7 eV and is assumed to originate from OH groups.

After formation of the hydroxyle monolayer on PEO-TiO_2, water molecules adsorb physically via hydrogen bonds at surface hydroxyl groups and form the first physisorbed water layer [11,18,19,23]. The bond between surface hydroxyl groups and physisorbed water molecules is stronger compared with the water–water interaction in the following layers of water, especially when single water molecules bind to two surface hydroxyl groups [23,24]. When the first water layer is completed, further water molecules bind via hydrogen bonds (physisorbed water). The bond strength between water molecules decreases with increasing distance from the surface and the structure progressively resembles liquid water [11].

To confirm the formation of multilayers on PEO-TiO_2, water adsorption/desorption isotherms at 30 °C were recorded with a humidity-controlled thermobalance. Prior to the experiment, the oxide was heated to 120 °C for 1 h to reduce the surface concentration of water adsorption species. The adsorption isotherm in Figure 2 shows first an increase in slope around 0–20% r.h. In the concept of BET-multilayer adsorption (BET: Brunauer–Emmett–Teller), the subsequent inflection point often indicates the transition from monolayer adsorption to multilayer adsorption [25]. By fitting the BET equation to the experimental data, we determined the inflection point at approximately 24% r.h. Thus we assumed that multilayer adsorption roughly evolves above 24% r.h. When the amount of water further increases, capillary condensation in the pores is likely to occur [24]. Such capillary condensation may be determined from the steep rise in the adsorption isothermal in the range of 85–100% r.h. The subsequent desorption isotherm deviates at 0% r.h. from the adsorption isotherm, presumably because the measurement time of 40 min per step is not long enough to achieve equilibrium at 30 °C.

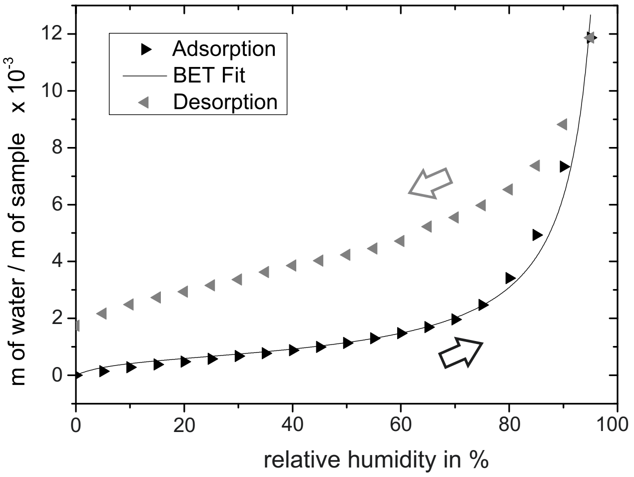

Figure 2. Water adsorption/desorption isotherm recorded at 30 °C reveals insights into the water adsorption process on PEO-TiO$_2$. The adsorption isotherm is additionally fitted by the BET equation.

3.2. Characteristics at Different Levels of Humidity

The sample setup is shown in Figure 3a. The Pt/Ti junction provides low ohmic resistance, while the dominant nonlinear resistance is associated with the Pt/PEO-TiO$_2$ interface. *I*–*V* curves were recorded at defined levels of humidity in regular time intervals. Initially, when the dry nitrogen flow started, the *I*–*V* curves began to flatten. After more than 10 h, the current vanished within the resolution of the digital multimeter for applied voltages up to 4 V. As shown in Figure 3b, the intensity of the curve increased again with increasing humidity in the nitrogen flow.

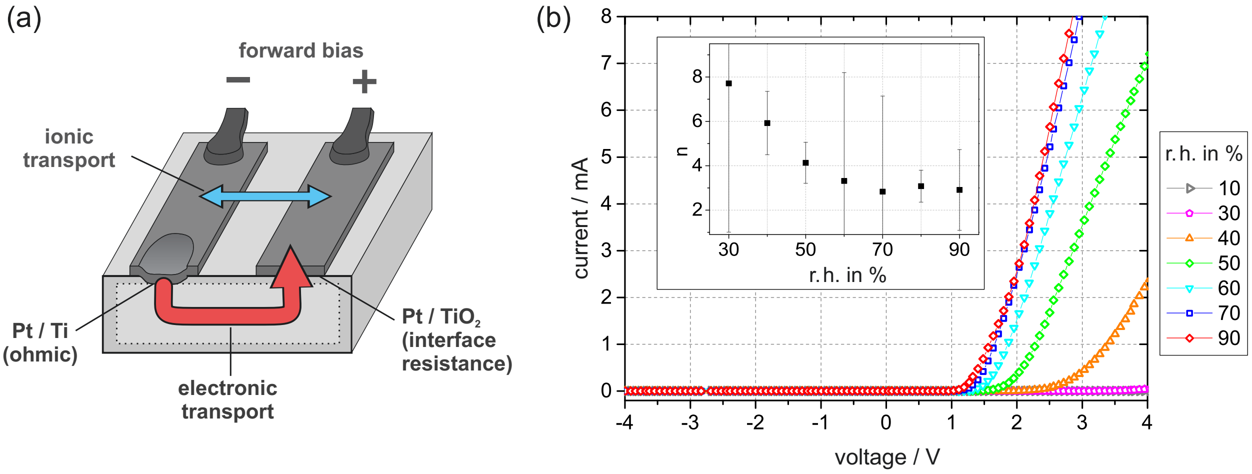

Figure 3. (**a**) The sample setup under the forward bias condition. Schematically shown are the relevant junctions, the electronic transport, and the possible contribution of ionic transport. (**b**) *I*–*V* curves were recorded at 30 °C and constant levels of humidity. The inner graph shows the ideality factor *n*, which was obtained by fitting the *I*–*V* curves according to the concept of an interface-controlled Schottky contact. The error bars are deduced from the fitting standard error.

The shape of the *I*–*V* curves follows the equation for an interface-controlled Schottky junction,

$$I(V) = \left\{ A\,A^{*}\,T^{2}\,\exp\left(-\frac{e\Phi_{\mathrm{SB}}}{kT}\right)\right\}\left\{\exp\left(\frac{e(V-IR)}{nkT}\right)-1\right\} \quad (3a)$$

$$I(V) = I_{\mathrm{S}}\left\{\exp\left(\frac{e(V-IR)}{nkT}\right)-1\right\}, \quad (3b)$$

where A is the Schottky contact area, A^* is the "Richardson constant", T is the temperature, e is the elementary charge, k is the Boltzmann constant, Φ_{SB} is the Schottky barrier height, R is the internal resistance, n is the ideality factor, and I_S is the saturation current.

By fitting the I–V curves according to reference [26], we obtain the ideality factor n, which can be used to estimate the density of occupied interface states. According to the values of n in Figure 3b, the density of interface states drastically decreases with humidity. This tendency is inverse to the effect of oxygen exposure [6]. To explain our observation, we focus on the electronic charge transport across the Pt/PEO-TiO_2 interface.

3.2.1. Interaction of Adsorbed Oxygen and Water

Intrinsic point defects in TiO_2, as oxygen vacancies V_O and titanium interstitials Ti_{int}, induce excess electrons, which can be thermally excited into the conduction band [27]. Therefore, TiO_2 with oxygen deficit behaves as a n-type semiconductor. The corresponding electronic states are often summarized in a defect band E_d, situated approximately 0.1 eV below E_C with a maximum density of states appearing 0.9 eV below E_F [28]. When a Pt/TiO_2 junction is formed, an electron depleted layer within TiO_2 evolves due to work function differences between Pt and TiO_2. The depletion layer induces a band bending eV_S, which represents a significant resistance for the electronic transport across the Pt/TiO_2 interface. Oxygen ionosorption at three-phase-boundaries (TPBs), i.e., $O^-{}_{(2)\ ads}$/Pt/TiO_2, described in Reactions (1) and (2), additionally enhances the depletion layer and increases the band bending by localizing electrons from the occupied conduction band of TiO_2 [6]. The left scheme in Figure 4 shows the band bending in an oxygen-containing atmosphere with low humidity, including the defect band E_d and oxygen induced acceptor states.

At dry nitrogen or low humidity, e.g., 10% r.h., the current of the I–V curve in Figure 3 barely shows any response to the applied voltage, which we attribute to the high interface resistance. The origin of the high resistance is assumed to be oxygen ionosorption from the residual oxygen in the nitrogen, which corresponds to less than 5×10^{-2} Pa. Previous studies on single crystalline TiO_2 (rutile phase) showed that oxygen partial pressures in this range already enhance the resistance noticeably [6,9]. The high impact of oxygen, already at low partial pressures, prevents the Pt/PEO-TiO_2 material for oxygen sensing in dry atmospheres.

However, in humid atmospheres, the I–V curves drastically increase. We attribute the effect to a reaction of H_2O with ionosorbed atomic oxygen, $O^-{}_{ads}$. When water vapor is provided, water molecules may adsorb associative at a free adsorption site V_{ads}, summarized in the equilibrium reaction

$$H_2O + V_{ads} \rightleftharpoons H_2O_{ads}\ \cdot \tag{4}$$

At TiO_2(110), V_{ads} is typically a free site at an undercoordinated titanium atom, where water molecules bond with their O end [21]. Atomic ionosorbed oxygen is also situated at these sites. When water is in the immediate vicinity of $O^-{}_{ads}$, water may dissociate by transferring a hydrogen atom to the adjacent ionosorbed oxygen. The formed hydroxyl groups are bound to lattice titanium and are referred to as terminal groups, OH_{ads}. The electron in the reaction

$$H_2O + V_{ads} + O^-{}_{ads} \rightleftharpoons 2OH_{ads} + e^- \tag{5}$$

originates from $O^-{}_{ads}$ and is released to the conduction band of TiO_2. An analogue reaction for SnO_2 is generally accepted, supported by several experiments [29–31]. As a consequence of electron injection, the depletion and band bending are reduced. Thus, the resistance decreases and higher current values occur. The change in the band structure is illustrated in Figure 4 by the transition from left to right.

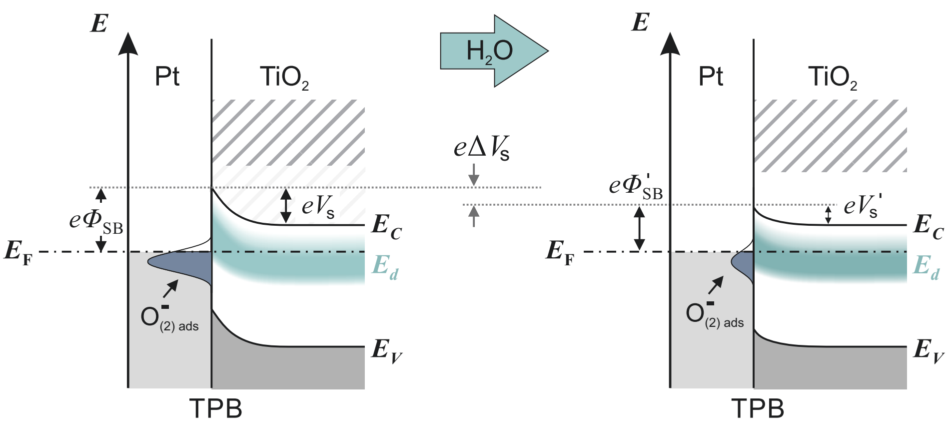

Figure 4. Illustration of the band structure of Pt/TiO$_2$ at three phase boundaries (TPBs). In the left scheme, the depletion and band bending is strongly promoted by the high surface density of ionosorbed oxygen, e.g., O$^-{}_{ads}$. When the humidity increases, the density decreases. The impact on the band structure is shown in the right scheme. In comparison, the band bending is reduced by $e\Delta V_S$.

3.3. Current Transients at Different Levels of Humidity

In the following, the results of the time-resolved current measurements with an applied voltage of 3 V are presented. Before, the sample was exposed to a defined r.h. for several hours until the current reaches a constant value. The value can be taken from the first minutes of the transient in Figure 5a. We assume that the constant current corresponds to a quasi-equilibrium concentration of ionosorbed oxygen for the given timescale. With increasing level of humidity, the current value increases, which is therefore attributed to a decrease in the density of ionosorbed oxygen. In accordance to our considerations from Section 3.2.1, this is caused by the replacement of O$^-{}_{ads}$ in Reaction (5). The density of free adsorption sites decreases with increasing humidity because more and more adsorption sites V$_{ads}$ are occupied by H$_2$O and OH groups. Thus, less sites are accessible for oxygen ionosorption and the equilibrium concentration decreases. As a beneficial side effect for sensing applications, the signal-to-noise ratio increases directly with the current.

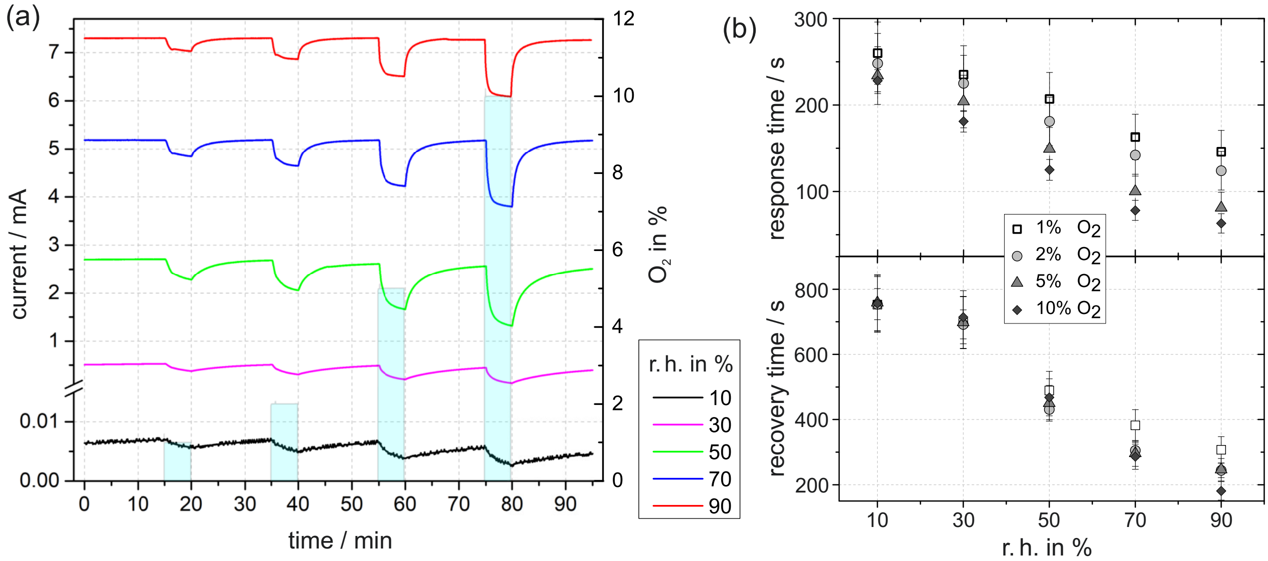

Figure 5. (**a**) Time dependent current at 3 V in constant levels of r.h. at 30 °C with exposure to different concentrations of oxygen. (**b**) The response time was determined by the time until the signal has fallen to 10% of the initial value relative to the minimum after five minutes of oxygen exposure. In analogous way, the subsequent recovery time was determined by the time until the signal has reached 90% of the following maximum (in nitrogen).

3.3.1. Response to Oxygen Exposure

To obtain insights into the kinetics, oxygen at different concentrations is temporally provided. First, the common features of the transients are discussed.

Upon oxygen exposure, each current transient in Figure 5 shows a rapid decrease. The decrease is attributed to the accumulation of ionosorbed oxygen via Reactions (1) and (2).

The absolute current difference of the initial current and the final current after five minutes of oxygen exposure depends on the oxygen concentration (i.e., 1%, 2%, 5%, or 10% O_2). The difference increases with higher oxygen levels, which reflects the increased surface density of ionosorbed oxygen species, which rises with the oxygen concentration in the gas flow.

The ambient humidity largely affects the current decay in the transients. The absolute difference between initial value and final value tends to increase with r.h. As before, the difference is mainly reflected by the variable density of ionosorbed oxygen. In nitrogen with low humidity, the density is already relatively high due to free adsorption sites in combination with residual oxygen. When a defined oxygen concentration is added to the nitrogen, the electronic depletion further increases, but the absolute change is small. This is due to the inhibited release of electrons at a high depletion. In contrast to low humidity, the depletion at higher humidity is less pronounced. Therefore, more electrons are accessible and can be transferred to oxygen interface states, which is ultimately reflected in the higher current difference on oxygen exposure.

3.3.2. Oxygen-Induced Changes in Kinetics

An important result from the time-resolved current measurement is that the response and recovery times, shown in Figure 5b, decrease more rapidly with increasing humidity. In case of 5% oxygen exposure, the difference between 10% and 90% r.h. amounts to 153 ± 38 s for the response time and 513 ± 93 s for the recovery time. Together with the improved signal-to-noise ratio in the current, this is a clear indication of the improvement in oxygen sensing with Pt/PEO-TiO_2 in the presence of water vapor.

To understand the accelerated kinetics at elevated humidity, we consider which reaction step is rate-determining for accumulation or depletion of ionosorbed oxygen. At high humidity, water layers resemble bulk water, and diffusion of oxygen species through water to the interface occurs, where they adsorb and form acceptor states. If the diffusion process is rate-determining, the response and recovery times at high humidity should be higher compared with low humidity, which was not found. Therefore, we exclude the diffusion process as rate-determining. Instead, we presume that the electron transfer reactions (ETRs) between TiO_2 and oxygen adsorbates dominate the overall reaction rate. The rate of ETR is controlled by the band bending at the interface. Figure 4 shows a schematic band model of the TPB at high and low humidity. The band bending eV_S at high humidity is significantly less in comparison with the band bending at low humidity. With the reasonable assumption that the ETR rate depends on the band bending, we conclude that the overall kinetic increases with humidity.

In general, the recovery times in the lower half of Figure 5b are significantly larger compared with the response times, which is common for oxygen detection with TiO_2 [8,32]. We conclude that the accumulation of ionosorbed oxygen is kinetically faster than the subsequent depletion.

3.4. Current Transients at Elevated Temperature

We repeated the time-dependent measurements at 90% r.h. and adjusted the temperature of the sample gradually from 30 to 170 °C. When considering the impact of the temperature, the current expression (3a) for the I–V curve predicts an increasing current with increasing temperature. However, the results in Figure 6a reveal a decreasing current with increasing temperature. The temperature dependence can only be adequately addressed if a more detailed picture about the interaction is considered.

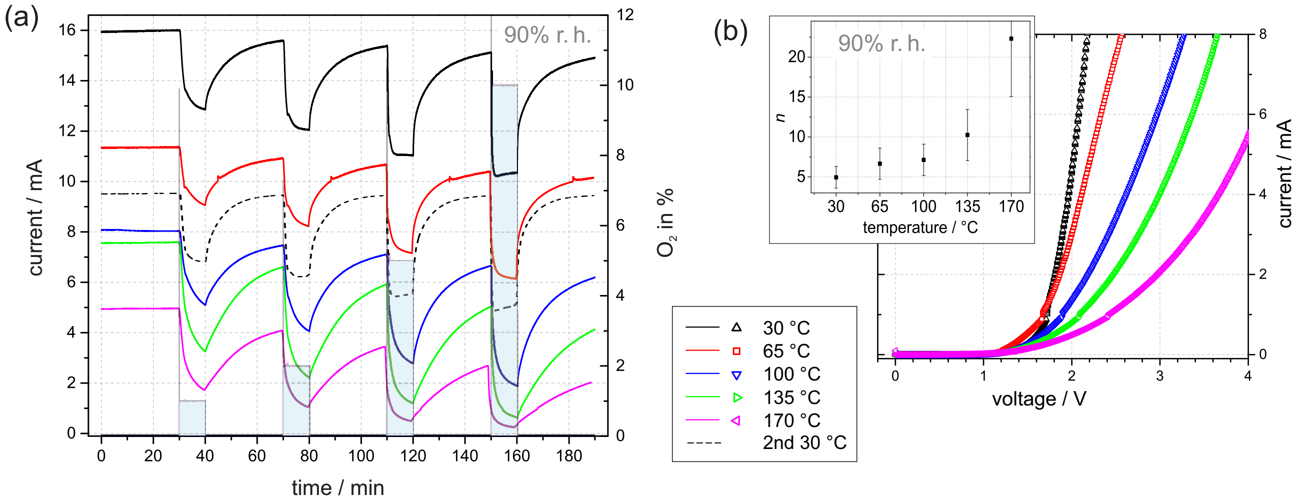

Figure 6. (**a**) Current transients at 3 V in 90% r.h. at temperatures between 30 and 170 °C. The time with oxygen addition was 10 min and the time between oxygen exposure was 30 min. (**b**) The corresponding *I–V* curves were recorded immediately after the transients. The inner graph shows the dependence of the corresponding ideality factor *n* on temperature. The error bars are estimated based on fitting the standard error.

In general, an elevated temperature promotes desorption. Hereby, it is generally accepted that water molecules start to desorb at distinctly lower temperatures than adsorbed oxygen species, e.g., temperature-programmed desorption studies on TiO_2 rutile suggested that oxygen species, such as $O^-{}_{ads}$ and $O_2^-{}_{ads}$, desorb above 600 °C, whereas physically and chemically adsorbed water molecules desorb below 300 °C [33]. Thus, it is plausible to assume that at room atmosphere, mainly water molecules desorb from Pt/PEO-TiO_2 at temperatures up to 170 °C. Hence, water molecules as reaction partners for ionosorbed oxygen in Reaction (5) are missing and the increased density of new adsorption sites facilitates the accumulation of ionosorbed oxygen (from residual oxygen). In conclusion, the absolute current value decreases with increasing temperature. This assumption is supported by the corresponding *I–V* curves in Figure 6b. The embedded graph exhibits a noticeable increase in the corresponding ideality factor *n* with the temperature. This reflects the increasing surface density of ionosorbed oxygen.

After the measurement at 170 °C, the experiment was repeated at 30 °C. Figure 6a shows that the corresponding current at 30 °C approaches a constant value of around 9.5 mA, and the response to oxygen exposure is repeatable. We conclude from the similarities of the current transients the validity of the proposed model with reversible adsorption and desorption of water. The observed deviation of the absolute value of the current and the drift of the baseline may indicate a change in the oxygen vacancy concentration at elevated temperatures. We suppose that oxygen diffusion into the lattice is promoted with increasing temperature and diminishes the density of oxygen vacancies, which function as electron donators in PEO-TiO_2. Lower oxygen vacancy concentration results in decreased conductivity and oxygen lattice diffusion, which explains the baseline drift over time [8].

3.5. Donor Effect of Adsorbed Water

Our considerations so far are based on the assumption that the variable density of ionosorbed oxygen species predominantly determines the electronic behavior at the interface. Thereby, we focused on the main mechanism, but we are aware that the oxygen and water interaction on the Pt/PEO-TiO_2 surface can be significantly more complex. One of the major contributions stems from a possible donor effect of adsorbed water on Pt/TiO_2:

The basic prerequisite is the reaction of water with lattice oxygen. In certain surface configurations on TiO_2, water molecules orientate themselves so that one H atom per H_2O molecule interacts with a surface oxygen atom [21]. Subsequently, the hydrogen atom is transferred to the adjacent oxygen site, which formally corresponds to the homolytic dissociation of water [34]. As a result, two different hydroxyl groups evolve [33]:

$$H_2O + Ti_{Ti} + O_O \rightleftharpoons (Ti_{Ti} - OH) + (OH)_O \quad . \tag{6}$$

One group is the before-mentioned terminal group, which is bonded at titanium. The other group includes lattice oxygen and is referred to as the rooted group, OH_O. At this stage, no ETRs are yet involved. Heiland and Kohl suggested two reactions for SnO_2, which extend Reaction (6) by involving an electron donation [35]. In the following, we adapt the reactions for the TiO_2 surface. The first reaction respects that the rooted hydroxyl group has a lower electron affinity and can be ionized, expressed in the complete reaction

$$(OH)_O \rightleftharpoons (OH)_O^+ + e^- \quad . \tag{7a}$$

In the second reaction, a rooted hydroxyl group bonds to a second titanium atom, leaving a vacancy, V_O, in place. In the reaction

$$Ti_{Ti} + (OH)_O \rightleftharpoons (Ti_{Ti} - OH) + {V_O}^{2+} + 2e^- \tag{7b}$$

the vacancy is already doubly ionized. The corresponding donor states contribute to the intensity of the defect band E_d. At this point, it should be noted that several studies indicate that rooted OH_O groups also contribute to the defect band E_d in the band gap of TiO_2(110) [27,36]. Overall, both reactions induce defect states from which electrons can be thermally excited to the conduction band. As a consequence, the depletion and band bending is reduced.

In our current measurement, the reactions with the lattice oxygen, i.e., Reactions (7a) and (7b), could not be distinguished from the replacement Reaction (5). We suppose that Equation (5) prevails when the surface density of ionosorbed oxygen is high. However, when the concentration of ionosorbed oxygen diminishes, Reactions (7a) and (7b) contribute progressively. Findings on SnO_2 suggest that the reaction with lattice oxygen is further promoted by platinum additives [31]. We assume that the kinetics of the reactions with lattice oxygen is relatively low at 30 °C. This would explain the waiting time of several hours until a constant current is reached before each measurement.

3.6. Ionic Transport along the Surface

So far, we only covered electronic transport through the Pt/PEO-TiO_2/Ti structure. For the sake of completeness, we also discuss an ionic contribution. The schematically illustrated sample setup in Figure 5a indicates ionic charge transport along the TiO_2 surface between both Pt pads. This is especially conceivable if the specimen is exposed to higher humidity. Hereby, physisorbed water layers on TiO_2 occur, which gradually resemble bulk liquid water. Autoprotolysis and charge transport by a Grotthus chain reaction increase the surface conductivity [11]. With additional charge transfer at both platinum electrodes, this would correspond to an electrolytic cell for water splitting. Assuming that the applied voltage exceeds the required decomposition voltage of H_2O (including the overvoltages at the Pt electrodes), a nonlinear *I*–*V* curve is expected (Butler–Volmer equation).

However, two findings contradict such an ionic charge transfer as a predominant origin for the observed *I*–*V* curves: First, the *I*–*V* curves should be symmetrical with respect to 0 V. Thus, a non-vanishing current is expected in the positive and negative voltage regions, which could not be confirmed by the *I*–*V* curves in Figure 3. Second, during electrolysis, hydrogen generation at platinum can be expected. At a current of approximately 7 mA, we would be able to detect traces of molecular hydrogen. This was tested with a thermal conductivity sensor (TCS208F, Gerhard R. Wagner Sensors, Systems & Services, Friedberg, HE, Germany). We found no signal above the TCS baseline for voltages up to 5 V or at any humidity level. We therefore assume that an ionic current contribution was neglectable in our investigation.

4. Conclusions

In our study, we demonstrated that adsorbed water improves the oxygen sensing properties of Pt/PEO-TiO_2/Ti at moderate temperatures.

Fundamental to our sample design was porous plasma electrolytically oxidized titanium (PEO-TiO_2), which was shown to tend toward water multilayer adsorption at elevated humidity. Platinum clusters on PEO-TiO_2 function as a catalytically active material and an electrode. The Pt/PEO-TiO_2 junction evidently forms a depletion layer, which is additionally controlled by oxygen adsorbates that localize/capture electrons from the TiO_2 conduction band. The strong oxygen dependency qualifies for a sensor mechanism, but in room atmosphere, the oxygen partial pressure and thus the interface resistance are so high that hardly any current can be detected for applied voltages up to 4 V. With increasing relative humidity (r.h.) at 30 °C, the current and, ultimately, the signal-to-noise ratio slowly increase. We attribute the effect mainly to the replacement of oxygen adsorbates: A direct reaction with water is proposed, which decreases the surface density of ionized oxygen adsorbates and injects electrons into the depletion zone. In addition, the increasing humidity promotes the occupancy of adsorption sites by H_2O or OH groups, resulting in fewer adsorption sites for oxygen adsorbates. In sum, the depletion and ultimately the interface resistance at Pt/PEO-TiO_2 decrease. Notably, a further reinforcement by a donor effect of water adsorbates is considered.

Furthermore, our results showed that the response and recovery of the current value on temporary oxygen exposure strongly depends on the ambient humidity. With increasing humidity, the change in the current is accelerated. In the frame of the previous argumentation, we assume that the reduced band bending at higher humidity facilitates electron transfer reactions, which presumably determine the overall reaction rate. Our considerations are further supported by current measurements at elevated temperatures up to 170 °C. The results suggest a predominant effect of oxygen adsorbates with increasing temperature, due to the progressive desorption of water molecules. Thus, the beneficial effects for oxygen sensing in humid atmospheres is limited to low temperatures.

In summary, the study highlights the importance of ambient humidity on the effects of oxygen adsorption on Pt/TiO_2. It was shown that elevated humidity can be exploited to counteract the shortcomings of oxygen sensing at low temperatures and high oxygen partial pressures. Our findings expand the current understanding of the complex interplay of water and oxygen on semiconducting metal oxides and suggest ways to benefit from it.

Author Contributions: Conceptualization, B.E. and K.S.; formal analysis, B.E.; investigation, B.E.; data curation, B.E.; writing—original draft preparation, B.E.; writing—review and editing, B.E. and K.S.; visualization, B.E.; supervision, K.S. All authors have read and agreed to the published version of the manuscript.

Funding: We acknowledge support by the Heinrich-Heine-University Duesseldorf.

Institutional Review Board Statement: Not applicable.

Informed Consent Statement: Not applicable.

Data Availability Statement: Not applicable.

Acknowledgments: We gratefully thank Mhamed El Achhab for fruitful discussions and Andreas Schreiber from Microtrac Retsch GmbH for the recording of the water adsorption/desorption isotherms.

Conflicts of Interest: The authors declare no conflict of interest.

References

1. Bai, J.; Zhou, B. Titanium Dioxide Nanomaterials for Sensor Applications. *Chem. Rev.* **2014**, *114*, 10131–10176. [CrossRef]
2. Neri, G. First Fifty Years of Chemoresistive Gas Sensors. *Chemosensors* **2015**, *3*, 1–20. [CrossRef]
3. Elser, M.J.; Diwald, O. Facilitated Lattice Oxygen Depletion in Consolidated TiO_2 Nanocrystal Ensembles: A Quantitative Spectroscopic O_2 Adsorption Study. *J. Phys. Chem. C* **2012**, *116*, 2896–2903. [CrossRef]
4. Cerchez, M.; Langer, H.; Achhab, M.E.; Heinzel, T.; Ostermann, D.; Lüder, H.; Degenhardt, J. Dynamics of hydrogen sensing with Pt/TiO_2 Schottky diodes. *Appl. Phys. Lett.* **2013**, *103*, 033522. [CrossRef]
5. El Achhab, M.; Schierbaum, K. Gas sensors based on plasma-electrochemically oxidized titanium foils. *J. Sens. Sens. Syst.* **2016**, *5*, 273–281. [CrossRef]
6. Schierbaum, K.D.; Kirner, U.K.; Geiger, J.F.; Göpel, W. Schottky-barrier and conductivity gas sensors based upon Pd/SnO_2 and Pt/TiO_2. *Sens. Actuators B Chem.* **1991**, *4*, 87–94. [CrossRef]
7. Gurlo, A. Insights into the Mechanism of Gas Sensor Operation. In *Metal Oxide Nanomaterials for Chemical Sensors*; Carpenter, M.A., Mathur, S., Kolmakov, A., Eds.; Springer: New York, NY, USA, 2013; pp. 3–34. ISBN 978-1-4614-5394-9.
8. Rothschild, A.; Edelman, F.; Komem, Y.; Cosandey, F. Sensing behavior of TiO_2 thin films exposed to air at low temperatures. *Sens. Actuators B Chem.* **2000**, *67*, 282–289. [CrossRef]
9. Kirner, U.; Schierbaum, K.D.; Göpel, W.; Leibold, B.; Nicoloso, N.; Weppner, W.; Fischer, D.; Chu, W.F. Low and high temperature TiO_2 oxygen sensors. *Sens. Actuators B Chem.* **1990**, *1*, 103–107. [CrossRef]
10. Morrison, S.R. Semiconductor gas sensors. *Sens. Actuators* **1981**, *2*, 329–341. [CrossRef]
11. Wang, Z.; Shi, L.; Wu, F.; Yuan, S.; Zhao, Y.; Zhang, M. The sol-gel template synthesis of porous TiO_2 for a high performance humidity sensor. *Nanotechnology* **2011**, *22*, 275502. [CrossRef] [PubMed]
12. Gong, M.; Li, Y.; Guo, Y.; Lv, X.; Dou, X. 2D TiO_2 nanosheets for ultrasensitive humidity sensing application benefited by abundant surface oxygen vacancy defects. *Sens. Actuators B Chem.* **2018**, *262*, 350–358. [CrossRef]
13. Zhang, Z.; Du, Y.; Petrik, N.G.; Kimmel, G.A.; Lyubinetsky, I.; Dohnálek, Z. Water as a Catalyst: Imaging Reactions of O_2 with Partially and Fully Hydroxylated TiO_2(110) Surfaces. *J. Phys. Chem. C* **2009**, *113*, 1908–1916. [CrossRef]
14. Engelkamp, B.; El Achhab, M.; Fischer, B.; Kökçam-Demir, l.; Schierbaum, K. Combined Galvanostatic and Potentiostatic Plasma Electrolytic Oxidation of Titanium in Different Concentrations of H_2SO_4. *Metals* **2018**, *8*. [CrossRef]
15. Engelkamp, B.; Fischer, B.; Schierbaum, K. Plasma Electrolytic Oxidation of Titanium in H_2SO_4-H_3PO_4 Mixtures. *Coatings* **2020**, *10*. [CrossRef]
16. Ramamoorthy, M.; Vanderbilt, D.; King-Smith, R.D. First-principles calculations of the energetics of stoichiometric TiO_2 surfaces. *Phys. Rev. B* **1994**, *49*, 16721–16727. [CrossRef]
17. Futera, Z.; English, N.J. Electric-Field Effects on Adsorbed-Water Structural and Dynamical Properties at Rutile- and Anatase-TiO_2 Surfaces. *J. Phys. Chem. C* **2016**, *120*, 19603–19612. [CrossRef]
18. Traversa, E. Ceramic sensors for humidity detection: The state-of-the-art and future developments. *Sens. Actuators B Chem.* **1995**, *23*, 135–156. [CrossRef]
19. Nosaka, A.Y.; Fujiwara, T.; Yagi, H.; Akutsu, H.; Nosaka, Y. Characteristics of Water Adsorbed on TiO_2 Photocatalytic Systems with Increasing Temperature as Studied by Solid-State 1H NMR Spectroscopy. *J. Phys. Chem. B* **2004**, *108*, 9121–9125. [CrossRef]
20. Wang, R.; Hashimoto, K.; Fujishima, A.; Chikuni, M.; Kojima, E.; Kitamura, A.; Shimohigoshi, M.; Watanabe, T. Photogeneration of Highly Amphiphilic TiO_2 Surfaces. *Adv. Mater.* **1998**, *10*, 135–138. [CrossRef]
21. Diebold, U. Perspective: A controversial benchmark system for water-oxide interfaces: H2O/TiO_2(110). *J. Chem. Phys.* **2017**, *147*, 040901. [CrossRef]
22. Wang, L.; Yu, H.; Wang, K.; Xu, H.; Wang, S.; Sun, D. Local Fine Structural Insight into Mechanism of Electrochemical Passivation of Titanium. *ACS Appl. Mater. Interfaces* **2016**, *8*, 18608–18619. [CrossRef] [PubMed]
23. Takahashi, K.; Yui, H. Analysis of Surface OH Groups on TiO_2 Single Crystal with Polarization Modulation Infrared External Reflection Spectroscopy. *J. Phys. Chem. C* **2009**, *113*, 20322–20327. [CrossRef]
24. Nahar, R.K.; Khanna, V.K.; Khokle, W.S. On the origin of the humidity-sensitive electrical properties of porous aluminium oxide (sensor application). *J. Phys. D Appl. Phys.* **1984**, *17*, 2087–2095. [CrossRef]
25. Reschetilowski, W. *Einführung in Die Heterogene Katalyse*; Springer Spektrum: Berlin/Heidelberg, Germany, 2015; ISBN 978-3-662-46983-5.
26. Schierbaum, K.; El Achhab, M. Generation of an electromotive force by hydrogen-to-water oxidation with Pt-coated oxidized titanium foils. *Phys. Status Solidi A* **2011**, *208*, 2796–2802. [CrossRef]
27. Yin, W.J.; Wen, B.; Zhou, C.; Selloni, A.; Liu, L.M. Excess electrons in reduced rutile and anatase TiO_2. *Surf. Sci. Rep.* **2018**, *73*, 58–82. [CrossRef]
28. Zhao, J.; Li, B.; Onda, K.; Feng, M.; Petek, H. Solvated Electrons on Metal Oxide Surfaces. *Chem. Rev.* **2006**, *106*, 4402–4427. [CrossRef]
29. Schierbaum, K.D.; Weimar, U.; Göpel, W.; Kowalkowski, R. Conductance, work function and catalytic activity of SnO_2-based gas sensors. *Sens. Actuators B Chem.* **1991**, *3*, 205–214. [CrossRef]
30. Koziej, D.; Bârsan, N.; Weimar, U.; Szuber, J.; Shimanoe, K.; Yamazoe, N. Water-oxygen interplay on tin dioxide surface: Implication on gas sensing. *Chem. Phys. Lett.* **2005**, *410*, 321–323. [CrossRef]
31. Großmann, K.; Wicker, S.; Weimar, U.; Barsan, N. Impact of Pt additives on the surface reactions between SnO_2, water vapour, CO and H_2; an operando investigation. *Phys. Chem. Chem. Phys.* **2013**, *15*, 19151–19158. [CrossRef]

32. Mokrushin, A.S.; Simonenko, E.P.; Simonenko, N.P.; Akkuleva, K.T.; Antipov, V.V.; Zaharova, N.V.; Malygin, A.A.; Bukunov, K.A.; Sevastyanov, V.G.; Kuznetsov, N.T. Oxygen detection using nanostructured TiO_2 thin films obtained by the molecular layering method. *Appl. Surf. Sci.* **2019**, *463*, 197–202. [CrossRef]
33. Egashira, M.; Kawasumi, S.; Kagawa, S.; Seiyama, T. Temperature Programmed Desorption Study of Water Adsorbed on Metal Oxides. I. Anatase and Rutile. *Bull. Chem. Soc. Jpn.* **1978**, *51*, 3144–3149. [CrossRef]
34. Barsan, N.; Weimar, U. Understanding the fundamental principles of metal oxide based gas sensors; the example of CO sensing with SnO_2 sensors in the presence of humidity. *J. Phys. Condens. Matter* **2003**, *15*, R813–R839. [CrossRef]
35. Heiland, G.; Kohl, D. Physical and Chemical Aspects of Oxidic Semiconductor Gas Sensors. In *Chemical Sensor Technology*; Seiyama, T., Ed.; Elsevier Science Pub. Co.: New York, NY, USA, 1988; Volume 1, pp. 15–38. ISBN 0-444-98901-3.
36. Mao, X.; Lang, X.; Wang, Z.; Hao, Q.; Wen, B.; Ren, Z.; Dai, D.; Zhou, C.; Liu, L.M.; Yang, X. Band-Gap States of TiO_2(110): Major Contribution from Surface Defects. *J. Phys. Chem. Lett.* **2013**, *4*, 3839–3844. [CrossRef]

4 Summary

This thesis has addressed several topics, which arise on the way to exploit electrochemical produced TiO_2 for oxygen sensing. Starting from the general electrochemical preparation of titanium oxide, modifications in the preparation technique were discussed and, ultimately, the material was tested for oxygen sensing. Fundamental for all topics is the tailored oxide layer on titanium, which is formed in the process of Plasma Electrolytic Oxidation (PEO).

The first chapter briefly reviews the main materials used in this research. Due to its central role, titanium dioxide is of particular interest here. The presented aspects form the foundation for chapters two and three, which include the findings of the experimental work.

In the second chapter the formation of titanium oxide is described in detail. Starting from the natural passivation of titanium in air or neutral liquids, the technical passivation in electrochemical cells is discussed. Hereby, the conventional anodic oxidation serves as the starting point for the extensive description of PEO. In the course of PEO, characteristic dielectric discharges continuously restructure an initially formed oxide layer, resulting in an usually porous coating with good adhesion to the substrate. The strength, density and frequency of discharges depend largely on the progressed time and parameters in the process. A particularly strong impact is related to the electrical parameters and the electrolyte composition.
The first peer-reviewed study in this thesis [108] addresses the effect of the electrolyte concentration on the oxide formation on a titanium foil. Herein, concentrated sulphuric acid (H_2SO_4) was used and a combination of galvanostatic and potentiostatic control was selected as the electrical operation mode. The maximum applied voltage and current density were $145\,\mathrm{V}$ and $10\,\mathrm{mA/cm^2}$, respectively. It was shown that especially the change in concentration between $0.5\,\mathrm{mol/l}$ and $7\,\mathrm{mol/l}$ leads to a noticeable change of the oxide layer. In contrast, the highest investigated concentration was $12.9\,\mathrm{mol/l}$ and the corresponding oxide layer showed only minor deviations to the one prepared in $7\,\mathrm{mol/l}$. With increasing concentration, the porosity and the thickness of the oxide layer increase. Furthermore, the ratio of the two prevailing TiO_2 polymorphs changes with increasing concentration from anatase to the high-temperature rutile modification. The observations were qualitatively traced back to an increase in the intensity and number of discharges in the process. The results provide an empirical overview of the concentration dependent PEO of titanium in sulfuric acid, which shows a convenient way to tailor the oxide layer to the specifications required for a given application.

While rutile is often chosen for its stability, anatase is generally favored for photocatalytic applications, since its performance is usually superior to the more stable rutile. However, mixtures of both polymorphic phases may outperform the individual phases, as recent studies in the field of photocatalyis demonstrate [138]. Not only from this perspective, the customization of the ratio is desirable. However, one shortcoming by using concentrated H_2SO_4 in PEO of titanium, is the correlated change in thickness and porosity when trying to adjust the ratio. It was also found that the layer thickness of a stable oxide is naturally limited in the process. In this context, a second peer-reviewed study [99] on galvanostatic PEO of titanium is presented. It outlines a feasible way to increase the anatase ratio without neglecting the film thickness. For this purpose, small additions of phosphoric acid (H_3PO_4) were added to 12.9 mol/l H_2SO_4 for an PEO process with $55\,\mathrm{mA/cm^2}$. The results demonstrate, that even small molar fractions of H_3PO_4, despite its molecular similarity, significantly alter the oxide formation. The appropriate addition of H_3PO_4, suppress the transformation of anatase to rutile. The suppressed rutile formation can be linked to the low number and intensity of discharges. Instead of discharges, the charge compensation in the presence of H_3PO_4 is assumed to proceed preferentially via ion migration. The effect could be attributed to a favored H_3PO_4 anion adsorption at the anodic surface, which is rationalized by the difference in the anion charge in the exceptionally high electric field in PEO. Another promising finding in both studies was the identification of a compact oxide layer between the substrate and the porous oxide in the thickness of 100–300 nm. It exhibits nanocrystalline anatase structures and low levels of electrolyte species, which were presumably trapped in the process. Both observations could be attributed to the large thermal mass of the substrate.

The objective in the third chapter was to study the PEO-produced titanium dioxide layer in respect to its oxygen sensing performance. For the basic sensor setup, the titanium oxide layer was formed by PEO in 12.9 mol/l H_2SO_4 and subsequently sputter-deposited with platinum. A brief introduction explains the basic reaction with adsorbed oxygen and platinum, followed by the third study [43], in which the experimental results are presented and discussed.
PEO-TiO_2 shows n-type semiconductor properties in contact with Pt by forming an electron depletion layer at the interface. Consequently, a band bending with a Schottky barrier in the electronic band structure occur. A similar effect is generated by oxygen adsorption. In fact, the influence of oxygen adsorbtion can be so large that the energetic barrier is referred to as surface-state controlled Schottky barrier [62]. It was experimentally shown that a high oxygen partial pressure, e.g., the concentration in ambient air, dominates the junction and substantially limits the electron transport across the interface. However, the investigation revealed that at moderate temperatures adsorbed water on Pt/PEO-TiO_2 attenuate this effect. It is supposed that adsorbed oxygen species react with water molecules, forming hydroxyl groups and, therefore, releasing an electron to the oxide conduction band and decreasing the band bending. In addition, a general donor effect by water adsorption on TiO_2 was considered as contribution. Notably, the kinetic in oxygen sensing increased with water adsorption as well, which could be rationalized by the reduced band bending. Overall, the findings expand the current understanding of the complex interplay of water and oxygen on TiO_2 and suggest ways to benefit from it.

Bibliography

[1] J. Schultze and M. Lohrengel, “Stability, reactivity and breakdown of passive films. Problems of recent and future research,” *Electrochimica Acta*, vol. 45, no. 15, pp. 2499 – 2513, 2000. URL: https://doi.org/10.1016/S0013-4686(00)00347-9

[2] D. Devilliers, M. T. Dinh, E. Mahé, D. Krulic, N. Larabi, and N. Fatouros, “Behaviour of titanium in sulphuric acid-application to DSAs,” *Journal of New Materials for Electrochemical Systems*, vol. 9, no. 3, p. 221, 2006. URL: https://hal.sorbonne-universite.fr/hal-00163175/

[3] J.-F. Vanhumbeeck and J. Proost, “Current understanding of Ti anodisation: functional, morphological, chemical and mechanical aspects,” *Corrosion Reviews*, vol. 27, no. 3, pp. 117–204, 2009. URL: https://doi.org/10.1515/CORRREV.2009.27.3.117

[4] M. V. Diamanti, M. Ormellese, and M. Pedeferri, “Application-wise nanostructuring of anodic films on titanium: a review,” *Journal of Experimental Nanoscience*, vol. 10, no. 17, pp. 1285–1308, 2015. URL: https://doi.org/10.1080/17458080.2014.999261https://doi.org/10.1080/17458080.2014.999261

[5] A. Fujishima and K. Honda, “Electrochemical photolysis of water at a semiconductor electrode,” *nature*, vol. 238, no. 5358, pp. 37–38, 1972. URL: https://doi.org/10.1038/238037a0

[6] A. Yerokhin, X. Nie, A. Leyland, A. Matthews, and S. Dowey, “Plasma electrolysis for surface engineering,” *Surface and Coatings Technology*, vol. 122, no. 2, pp. 73 – 93, 1999. URL: https://doi.org/10.1016/S0257-8972(99)00441-7

[7] N. P. Slugniov, *J. Russ. Phys. Chem. Soc.*, vol. 12, p. 193, 1880.

[8] D.-S. Tsai and C.-C. Chou, “Review of the Soft Sparking Issues in Plasma Electrolytic Oxidation,” *Metals*, vol. 8, no. 2, 2018. URL: https://doi.org/10.3390/met8020105

[9] A. Güntherschulze and H. Betz, “Die Bewegung der Ionengitter von Isolatoren bei extremen elektrischen Feldstärken,” *Zeitschrift für Physik*, vol. 92, no. 5, pp. 367–374, 1934. URL: https://doi.org/10.1007/BF01340820

[10] W. McNeill and G. F. Nordblom, “Method of Making Cadmium Niobate,” US Patent 2 854 390, 1958. URL: https://worldwide.espacenet.com/patent/search/family/024934518/publication/US2854390A?q=us2854390

[11] W. McNeill and L. Gruss, “Anodic Spark Reaction Processes and Articles,” US Patent 3 293 158, 1966. URL: https://worldwide.espacenet.com/patent/search/family/023198795/publication/US3293158A?q=US3293158

[12] S. D. Brown, K. J. Kuna, and T. B. Van, “Anodic Spark Deposition from Aqueous Solutions of NaAlO2 and Na2SiO3,” *Journal of the American Ceramic Society*, vol. 54, no. 8, pp. 384–390, 1971. URL: https://doi.org/10.1111/j.1151-2916.1971.tb12328.x

[13] G. A. Markov and G. V. Markova, “A method of forming anodes of electrolytic condensers,” Inventor’s Certificate No. 526961 (USSR), Byull. Izobret., No. 32, 1976.

[14] F. Simchen, M. Sieber, A. Kopp, and T. Lampke, “Introduction to Plasma Electrolytic Oxidation–An Overview of the Process and Applications,” 2020. URL: https://doi.org/10.3390/coatings10070628

[15] F. C. Walsh, C. T. J. Low, R. J. K. Wood, K. T. Stevens, J. Archer, A. R. Poeton, and A. Ryder, “Plasma electrolytic oxidation (PEO) for production of anodised coatings on lightweight metal (Al, Mg, Ti) alloys,” *Transactions of the IMF*, vol. 87, no. 3, pp. 122–135, 2009. URL: https://doi.org/10.1179/174591908X372482

[16] T. W. Clyne and S. C. Troughton, “A review of recent work on discharge characteristics during plasma electrolytic oxidation of various metals,” *International Materials Reviews*, vol. 0, no. 0, pp. 1–36, 2018. URL: https://doi.org/10.1080/09506608.2018.1466492

[17] K. Grossmann, U. Weimar, and N. Barsan, “Chapter Eight - Semiconducting Metal Oxides Based Gas Sensors,” in *Semiconductors and Semimetals*, B. G. Svensson, S. J. Pearton, and C. Jagadish, Eds. Elsevier, 2013, vol. 88, pp. 261–282. URL: https://doi.org/10.1016/B978-0-12-396489-2.00008-4

[18] J. Bai and B. Zhou, “Titanium Dioxide Nanomaterials for Sensor Applications,” *Chem. Rev.*, vol. 114, no. 19, pp. 10 131–10 176, 2014. URL: https://doi.org/10.1021/cr400625j

[19] N. Yamamoto, S. Tonomura, T. Matsuoka, and H. Tsubomura, “A study on a palladium-titanium oxide Schottky diode as a detector for gaseous components,” *Surface Science*, vol. 92, no. 2, pp. 400–406, 1980. URL: https://doi.org/10.1016/0039-6028(80)90212-5

[20] L. A. Harris, “A Titanium Dioxide Hydrogen Detector,” *Journal of The Electrochemical Society*, vol. 127, no. 12, pp. 2657–2662, 1980. URL: https://doi.org/10.1149/1.2129567

[21] Y. Shimizu, T. Hyodo, and M. Egashira, “H2 sensing performance of anodically oxidized TiO2 thin films equipped with Pd electrode,” *Sensors and Actuators B: Chemical*, vol. 121, no. 1, pp. 219–230, 2007. URL: https://doi.org/10.1016/j.snb.2006.09.039

[22] M. E. Achhab and K. Schierbaum, “Structure and Hydrogen Sensing Properties of Plasma Electrochemically Oxidized Titanium Foils,” *Procedia Engineering*, vol. 47, pp. 566 – 569, 2012, 26th European Conference on Solid-State Transducers, EUROSENSOR 2012. URL: https://doi.org/10.1016/j.proeng.2012.09.210

[23] M. Cerchez, H. Langer, M. E. Achhab, T. Heinzel, D. Ostermann, H. Lüder, and J. Degenhardt, “Dynamics of hydrogen sensing with Pt/TiO2 Schottky diodes,” *Applied Physics Letters*, vol. 103, no. 3, p. 033522, 2013. URL: https://doi.org/10.1063/1.4816265

[24] A. A. Haidry, A. Ebach-Stahl, and B. Saruhan, “Effect of Pt/TiO2 interface on room temperature hydrogen sensing performance of memristor type Pt/TiO2/Pt structure,” *Sensors and Actuators B: Chemical*, vol. 253, pp. 1043–1054, 2017. URL: https://doi.org/10.1016/j.snb.2017.06.159

[25] H. Kwon, Y. Lee, S. Hwang, and J. K. Kim, “Highly-sensitive H2 sensor operating at room temperature using Pt/TiO2 nanoscale Schottky contacts,” *Sensors and Actuators B: Chemical*, vol. 241, pp. 985–992, 2017. URL: https://doi.org/10.1016/j.snb.2016.11.022

[26] Z. Li, Z. Yao, A. A. Haidry, T. Plecenik, L. Xie, L. Sun, and Q. Fatima, “Resistive-type hydrogen gas sensor based on TiO2: A review,” *International Journal of Hydrogen Energy*, vol. 43, no. 45, pp. 21 114–21 132, 2018. URL: https://doi.org/10.1016/j.ijhydene.2018.09.051

[27] D. Ostermann, K. Schierbaum, and M. El Achhab, “Dioden-Dünnschichtanordnung zur Detektion von Wasserstoff und Verfahren zu ihrer Herstellung sowie Wasserstoffsensor,” EU Patent PCT/EP2012/055 189, 22. Dec. 2011. URL: https://worldwide.espacenet.com/patent/search/family/046929506/publication/WO2012130751A1?q=pn%3DWO2012130751A1

[28] K. D. Schierbaum, C. Schüle and M. El Achhab, “Sensoranordnung und Verfahren zum Herstellen einer Sensoranordnung,” German Patent DE102 012 108 997A1, 24. Sep. 2012. URL: https://worldwide.espacenet.com/patent/search/family/049261509/publication/DE102012108997A1?q=pn%3DDE102012108997A1

[29] K. D. Schierbaum, C. Schüle, and M. El Achhab, “Sensor and Method for manufacturing a sensor,” US Patent US2014/0 291 160A1, 2. Oct. 2014. URL: https://worldwide.espacenet.com/patent/search/family/047080477/publication/US2014291160A1?q=pn%3DUS2014291160A1

[30] U. Kirner, K. D. Schierbaum, W. Göpel, B. Leibold, N. Nicoloso, W. Weppner, D. Fischer, and W. F. Chu, “Low and high temperature TiO2 oxygen sensors,” *Sensors and Actuators B: Chemical*, vol. 1, no. 1, pp. 103–107, 1990. URL: https://doi.org/10.1016/0925-4005(90)80181-X

[31] K. D. Schierbaum, U. K. Kirner, J. F. Geiger, and W. Göpel, “Schottky-barrier and conductivity gas sensors based upon Pd/SnO2 and Pt/TiO2,” *Sensors and Actuators B: Chemical*, vol. 4, no. 1, pp. 87–94, 1991. URL: https://doi.org/10.1016/0925-4005(91)80181-I

[32] K. D. Schierbaum, X. Wei-Xing, S. Fischer, and W. Göpel, “Schottky Barriers and Ohmic Contacts with Pt/TiO2(110): Implications to Control Gas Sensor Properties,” in *Adsorption on Ordered Surfaces of Ionic Solids and Thin Films*. Berlin, Heidelberg: Springer, 1993, pp. 268–278, ISBN 978-3-540-57416-3. URL: https://doi.org/10.1007/978-3-642-78632-7

[33] K. D. Schierbaum, “Edelmetall/Metalloxid-Grenzflächen von heterogenen Katalysatoren und elektronischen Bauelementen: Die Modellsysteme Pt/TiO2(110) und Pd/SnO2(110),” Habilitation thesis, 1994.

[34] D. R. Lide, *CRC Handbook of Chemistry and Physics*, 85th ed. CRC Press, 2003, "Section 4: properties of the elements and inorganic compounds; melting, boiling, and critical temperatures of the elements", ISBN 0-8493-0458-7.

[35] H. Sitzmann and J. Hartmann-Schreier, “Sauerstoff,” 2011, website retrieved on 1 Jun. 2021. URL: https://roempp.thieme.de/lexicon/RD-19-00520

[36] M. Setvin, J. Hulva, G. S. Parkinson, M. Schmid, and U. Diebold, “Electron transfer between anatase TiO2 and an O2 molecule directly observed by atomic force microscopy,” *Proceedings of the National Academy of Sciences*, vol. 114, no. 13, pp. E2556–E2562, 2017. URL: https://doi.org/10.1073/pnas.1618723114

[37] H. M. Weiss, “Appreciating Oxygen,” *J. Chem. Educ.*, vol. 85, no. 9, p. 1218, 2008. URL: https://doi.org/10.1021/ed085p1218

[38] C. Schweitzer and R. Schmidt, “Physical Mechanisms of Generation and Deactivation of Singlet Oxygen,” *Chem. Rev.*, vol. 103, no. 5, pp. 1685–1758, 2003. URL: https://doi.org/10.1021/cr010371d

[39] G. A. Somorjai, “Surface Science and Catalysis,” *Science*, vol. 227, no. 4689, p. 902, 1985. URL: https://doi.org/10.1126/science.227.4689.902

[40] L. M. Falicov and G. A. Somorjai, “Correlation between catalytic activity and bonding and coordination number of atoms and molecules on transition metal surfaces: Theory and experimental evidence,” *Proc Natl Acad Sci USA*, vol. 82, no. 8, p. 2207, 1985. URL: https://doi.org/10.1073/pnas.82.8.2207

[41] J. K. Nørskov, J. Rossmeisl, A. Logadottir, L. Lindqvist, J. R. Kitchin, T. Bligaard, and H. Jónsson, “Origin of the Overpotential for Oxygen Reduction at a Fuel-Cell Cathode,” *J. Phys. Chem. B*, vol. 108, no. 46, pp. 17 886–17 892, 2004. URL: https://doi.org/10.1021/jp047349j

[42] J. L. Gland and V. N. Korchak, “The adsorption of oxygen on a stepped platinum single crystal surface,” *Surface Science*, vol. 75, no. 4, pp. 733–750, 1978. URL: https://doi.org/10.1016/0039-6028(78)90190-5

[43] B. Engelkamp and K. Schierbaum, “Oxygen Sensing of Pt/PEO-TiO2 in Humid Atmospheres at Moderate Temperatures,” *Sensors*, vol. 21, no. 7, 2021. URL: https://doi.org/10.3390/s21072558

[44] M. Alvisi, G. Galtieri, L. Giorgi, R. Giorgi, E. Serra, and M. A. Signore, “Sputter deposition of Pt nanoclusters and thin films on PEM fuel cell electrodes,” *Surface and Coatings Technology*, vol. 200, no. 5, pp. 1325–1329, 2005. URL: https://doi.org/10.1016/j.surfcoat.2005.07.093

[45] S. Herbertz, “Electroforming in titanium dioxide microdevices,” Ph.D. dissertation, Heinrich-Heine-Universität Düsseldorf, 2018.

[46] N. Wiberg, *Lehrbuch der anorganischen Chemie*, 102nd ed. De Gruyter, 2008. URL: https://www.degruyter.com/document/doi/10.1515/9783110206845/html

[47] T. Keller, “Verhalten von Wasserstoff in Titanlegierungen: Absorption, Diffusion und Phasenumwandlungen,” Ph.D. dissertation, Technische Universität Darmstadt, 2005.

[48] H. Okamoto, “O-Ti (Oxygen-Titanium),” *Journal of Phase Equilibria and Diffusion*, vol. 32, no. 5, p. 473, 2011. URL: https://doi.org/10.1007/s11669-011-9935-5

[49] M. T. Whittaker, “Titanium Alloys 2017,” *Metals*, vol. 8, no. 5, 2018. URL: https://doi.org/10.3390/met8050319

[50] D. A. H. Hanaor and C. C. Sorrell, “Review of the anatase to rutile phase transformation,” *Journal of Materials Science*, vol. 46, no. 4, pp. 855–874, 2011. URL: https://doi.org/10.1007/s10853-010-5113-0

[51] U. Diebold, “The surface science of titanium dioxide,” *Surface Science Reports*, vol. 48, no. 5, pp. 53 – 229, 2003. URL: https://doi.org/10.1016/S0167-5729(02)00100-0

[52] J. Zhang, P. Zhou, J. Liu, and J. Yu, “New understanding of the difference of photocatalytic activity among anatase, rutile and brookite TiO2,” *Physical Chemistry Chemical Physics*, vol. 16, no. 38, pp. 20 382–20 386, 2014. URL: https://doi.org/10.1039/C4CP02201G

[53] M. R. Ranade, A. Navrotsky, H. Z. Zhang, J. F. Banfield, S. H. Elder, A. Zaban, P. H. Borse, S. K. Kulkarni, G. S. Doran, and H. J. Whitfield, “Energetics of nanocrystalline TiO2,” *Proc Natl Acad Sci USA*, vol. 99, no. suppl 2, p. 6476, 2002. URL: https://doi.org/10.1073/pnas.251534898

[54] H. Zhang and J. F. Banfield, “Thermodynamic analysis of phase stability of nanocrystalline titania,” *J. Mater. Chem.*, vol. 8, pp. 2073–2076, 1998. URL: https://doi.org/10.1039/A802619J

[55] M. Landmann, E. Rauls, and W. G. Schmidt, "The electronic structure and optical response of rutile, anatase and brookite TiO2," *Journal of Physics: Condensed Matter*, vol. 24, no. 19, p. 195503, 2012. URL: https://doi.org/10.1088/0953-8984/24/19/195503

[56] K. Liu, A. I. Rykov, J. Wang, and T. Zhang, "Chapter One - Recent Advances in the Application of Mößbauer Spectroscopy in Heterogeneous Catalysis," in *Advances in Catalysis*, F. C. Jentoft, Ed. Academic Press, 2015, vol. 58, pp. 1–142. URL: https://doi.org/10.1016/bs.acat.2015.09.001

[57] R. A. Parker, "Static Dielectric Constant of Rutile (TiO_2), 1.6-1060°K," *Phys. Rev.*, vol. 124, no. 6, pp. 1719–1722, 1961. URL: https://doi.org/10.1103/PhysRev.124.1719

[58] J. Y. Kim, H. S. Jung, J. H. No, J.-R. Kim, and K. S. Hong, "Influence of anatase-rutile phase transformation on dielectric properties of sol-gel derived TiO2 thin films," *Journal of Electroceramics*, vol. 16, no. 4, pp. 447–451, 2006. URL: https://doi.org/10.1007/s10832-006-9895-z

[59] F. Millot, M. G. Blanchin, R. Tetot, J. F. Marucco, B. Poumellec, C. Picard, and B. Touzelin, "High temperature nonstoichiometric rutile TiO2 x," *Progress in solid state chemistry*, vol. 17, no. 4, pp. 263–293, 1987. URL: https://doi.org/10.1016/0079-6786(87)90004-5

[60] K. Zakrzewska, "Nonstoichiometry in TiO2-y Studied by Ion Beam Methods and Photoelectron Spectroscopy," *Advances in Materials Science and Engineering*, vol. 2012, p. 826873, 2011. URL: https://doi.org/10.1155/2012/826873

[61] T. Bak, J. Nowotny, N. J. Sucher, and E. Wachsman, "Effect of crystal imperfections on reactivity and photoreactivity of TiO2 (rutile) with oxygen, water, and bacteria," *The Journal of Physical Chemistry C*, vol. 115, no. 32, pp. 15 711–15 738, 2011. URL: https://doi.org/10.1021/jp2027862

[62] K. Schierbaum and M. El Achhab, "Generation of an electromotive force by hydrogen-to-water oxidation with Pt-coated oxidized titanium foils," *physica status solidi (a)*, vol. 208, no. 12, pp. 2796–2802, 2011. URL: https://doi.org/10.1002/pssa.201127400

[63] S. Kudelka, A. Michaelis, and J. W. Schultze, "Effect of texture and formation rate on ionic and electronic properties of passive layers on Ti single crystals," *Electrochimica Acta*, vol. 41, no. 6, pp. 863–870, 1996. URL: https://doi.org/10.1016/0013-4686(95)00375-4

[64] A. Weibel, R. Bouchet, and P. Knauth, "Electrical properties and defect chemistry of anatase (TiO2)," *Solid State Ionics*, vol. 177, no. 3, pp. 229–236, 2006. URL: https://doi.org/10.1016/j.ssi.2005.11.002

[65] J.-F. Marucco, J. Gautron, and P. Lemasson, “Thermogravimetric and electrical study of non-stoichiometric titanium dioxide TiO2x, between 800 and 1100°C,” *Journal of Physics and Chemistry of Solids*, vol. 42, no. 5, pp. 363–367, 1981. URL: https://doi.org/10.1016/0022-3697(81)90043-3

[66] J. Nowotny, M. A. Alim, T. Bak, M. A. Idris, M. Ionescu, K. Prince, M. Z. Sahdan, K. Sopian, M. A. Mat Teridi, and W. Sigmund, “Defect chemistry and defect engineering of TiO2-based semiconductors for solar energy conversion,” *Chem. Soc. Rev.*, vol. 44, no. 23, pp. 8424–8442, 2015. URL: https://doi.org/10.1039/C4CS00469H

[67] J. Zhao, B. Li, K. Onda, M. Feng, and H. Petek, “Solvated Electrons on Metal Oxide Surfaces,” *Chem. Rev.*, vol. 106, no. 10, pp. 4402–4427, 2006. URL: https://doi.org/10.1021/cr050173c

[68] V. E. Henrich, G. Dresselhaus, and H. J. Zeiger, “Observation of two-dimensional phases associated with defect states on the surface of TiO2,” *Physical Review Letters*, vol. 36, no. 22, pp. 1335–1339, 1976. URL: https://doi.org/10.1103/PhysRevLett.36.1335

[69] C. M. Yim, C. L. Pang, and G. Thornton, “Oxygen Vacancy Origin of the Surface Band-Gap State of TiO_2(110),” *PRL*, vol. 104, no. 3, p. 036806, 2010. URL: https://doi.org/10.1103/PhysRevLett.104.036806

[70] X. Mao, X. Lang, Z. Wang, Q. Hao, B. Wen, Z. Ren, D. Dai, C. Zhou, L.-M. Liu, and X. Yang, “Band-Gap States of TiO2(110): Major Contribution from Surface Defects,” *J. Phys. Chem. Lett.*, vol. 4, no. 22, pp. 3839–3844, 2013. URL: https://doi.org/10.1021/jz402053p

[71] S. Wendt, P. T. Sprunger, E. Lira, G. K. H. Madsen, Z. Li, J. . Hansen, J. Matthiesen, A. Blekinge-Rasmussen, E. Lægsgaard, B. Hammer, and F. Besenbacher, “The Role of Interstitial Sites in the Ti3d Defect State in the Band Gap of Titania,” *Science*, vol. 320, no. 5884, p. 1755, 2008. URL: https://doi.org/10.1126/science.1159846

[72] W.-J. Yin, B. Wen, C. Zhou, A. Selloni, and L.-M. Liu, “Excess electrons in reduced rutile and anatase TiO2,” *Surface Science Reports*, vol. 73, no. 2, pp. 58–82, 2018. URL: https://doi.org/10.1016/j.surfrep.2018.02.003

[73] M. A. Henderson, “A surface science perspective on TiO2 photocatalysis,” *Surface Science Reports*, vol. 66, no. 6, pp. 185–297, 2011. URL: https://doi.org/10.1016/j.surfrep.2011.01.001

[74] M. Ramamoorthy, D. Vanderbilt, and R. D. King-Smith, “First-principles calculations of the energetics of stoichiometric TiO_2 surfaces,” *PRB*, vol. 49, no. 23, pp. 16 721–16 727, 1994. URL: https://doi.org/10.1103/PhysRevB.49.16721

[75] U. Diebold, N. Ruzycki, G. S. Herman, and A. Selloni, "One step towards bridging the materials gap: surface studies of TiO2 anatase," *Catalysis Today*, vol. 85, no. 2, pp. 93–100, 2003. URL: https://doi.org/10.1016/S0920-5861(03)00378-X

[76] C. Dette, M. A. Pérez-Osorio, C. S. Kley, P. Punke, C. E. Patrick, P. Jacobson, F. Giustino, S. J. Jung, and K. Kern, "TiO2 Anatase with a Bandgap in the Visible Region," *Nano Lett.*, vol. 14, no. 11, pp. 6533–6538, 2014. URL: https://doi.org/10.1021/nl503131s

[77] A. Selloni, "Anatase shows its reactive side," *Nature Materials*, vol. 7, no. 8, pp. 613–615, 2008. URL: https://doi.org/10.1038/nmat2241

[78] V. E. Henrich and R. L. Kurtz, "Surface electronic structure of TiO_2: Atomic geometry, ligand coordination, and the effect of adsorbed hydrogen," *PRB*, vol. 23, no. 12, pp. 6280–6287, 1981. URL: https://doi.org/10.1103/PhysRevB.23.6280

[79] W. Hebenstreit, N. Ruzycki, G. S. Herman, Y. Gao, and U. Diebold, "Scanning tunneling microscopy investigation of the TiO_2 anatase (101) surface," *PRB*, vol. 62, no. 24, pp. R16 334–R16 336, 2000. URL: https://doi.org/10.1103/PhysRevB.62.R16334

[80] Z. Futera and N. J. English, "Exploring Rutile (110) and Anatase (101) TiO2 Water Interfaces by Reactive Force-Field Simulations," *J. Phys. Chem. C*, vol. 121, no. 12, pp. 6701–6711, 2017. URL: https://doi.org/10.1021/acs.jpcc.6b12803

[81] S. Wendt, R. Schaub, J. Matthiesen, E. K. Vestergaard, E. Wahlström, M. D. Rasmussen, P. Thostrup, L. M. Molina, E. Lægsgaard, I. Stensgaard, B. Hammer, and F. Besenbacher, "Oxygen vacancies on TiO2(110) and their interaction with H2O and O2: A combined high-resolution STM and DFT study," *Surface Science*, vol. 598, no. 1, pp. 226–245, 2005. URL: https://doi.org/10.1016/j.susc.2005.08.041

[82] M. A. Henderson, W. S. Epling, C. L. Perkins, C. H. F. Peden, and U. Diebold, "Interaction of Molecular Oxygen with the Vacuum-Annealed TiO2(110) Surface: Molecular and Dissociative Channels," *J. Phys. Chem. B*, vol. 103, no. 25, pp. 5328–5337, 1999. URL: https://doi.org/10.1021/jp990655q

[83] Y. He, O. Dulub, H. Cheng, A. Selloni, and U. Diebold, "Evidence for the Predominance of Subsurface Defects on Reduced Anatase TiO_2(101)," *PRL*, vol. 102, no. 10, p. 106105, 2009. URL: https://doi.org/10.1103/PhysRevLett.102.106105

[84] H. Kaesche, *Die Korrosion der Metalle - Physikalisch-chemische Prinzipien und aktuelle Probleme*, 3rd ed. Springer, 1990, ISBN 3-5405-1569-0.

[85] E. McCafferty, “Thermodynamics of Corrosion: Pourbaix Diagrams,” in *Introduction to Corrosion Science.* New York, NY: Springer, 2010, pp. 95–117. URL: https://doi.org/10.1007/978-1-4419-0455-3_6

[86] J. Barthel and R. Deiss, “The limits of the Pourbaix diagram in the interpretation of the kinetics of corrosion and cathodic protection of underground pipelines,” *Materials and Corrosion*, vol. 72, no. 3, pp. 434–445, 2021. URL: https://doi.org/10.1002/maco.202011977

[87] J. Macak, “Growth of anodic self-organized titanium dioxide nanotube layers,” Ph.D. dissertation, Friedrich-Alexander-Universität Erlangen-Nürnberg, 2008.

[88] E. J. W. Verwey, “Electrolytic conduction of a solid insulator at high fields The formation of the anodic oxide film on aluminium,” *Physica*, vol. 2, no. 1, pp. 1059–1063, 1935. URL: https://doi.org/10.1016/S0031-8914(35)90193-8

[89] M. M. Lohrengel, “Thin anodic oxide layers on aluminium and other valve metals: high field regime,” *Materials Science and Engineering: R: Reports*, vol. 11, no. 6, pp. 243–294, 1993. URL: https://doi.org/10.1016/0927-796X(93)90005-N

[90] N. Cabrera and N. F. Mott, “Theory of the oxidation of metals,” *Reports on Progress in Physics*, vol. 12, no. 1, p. 163, 1949. URL: https://doi.org/10.1088/0034-4885/12/1/308

[91] H. Habazaki, K. Shimizu, S. Nagata, P. Skeldon, G. E. Thompson, and G. C. Wood, “Ionic mobilities in amorphous anodic titania,” *Journal of The Electrochemical Society*, vol. 149, no. 3, pp. B70–B74, 2002. URL: https://doi.org/10.1149/1.1445171

[92] A. T. Fromhold, Jr., *Theory of metal oxidation*, ser. Defects in crystalline solids. North Holland Publishing Co., 1976, vol. 1: Fundamentals.

[93] M. V. Diamanti and M. P. Pedeferri, “Effect of anodic oxidation parameters on the titanium oxides formation,” *Corrosion Science*, vol. 49, no. 2, pp. 939–948, 2007. URL: https://doi.org/10.1016/j.corsci.2006.04.002

[94] S. Ikonopisov, “Theory of electrical breakdown during formation of barrier anodic films,” *Electrochimica Acta*, vol. 22, no. 10, pp. 1077–1082, 1977. URL: https://doi.org/10.1016/0013-4686(77)80042-X

[95] J. Albella, I. Montero, and J. Martinez-Duart, “A theory of avalanche breakdown during anodic oxidation,” *Electrochimica Acta*, vol. 32, no. 2, pp. 255 – 258, 1987. URL: https://doi.org/10.1016/0013-4686(87)85032-6

[96] M. D. Klapkiv, “Simulation of synthesis of oxide-ceramic coatings in discharge channels of a metal-electrolyte system,” *Materials Science*, vol. 35, no. 2, pp. 279–283, 1999. URL: https://doi.org/10.1007/BF02359992

[97] S. Stojadinović, R. Vasilić, and M. Perić, “Investigation of plasma electrolytic oxidation on valve metals by means of molecular spectroscopy - a review,” *RSC Adv.*, vol. 4, no. 49, pp. 25 759–25 789, 2014. URL: https://doi.org/10.1039/C4RA03873H

[98] S. C. Troughton, A. Nominé, A. V. Nominé, G. Henrion, and T. W. Clyne, “Synchronised electrical monitoring and high speed video of bubble growth associated with individual discharges during plasma electrolytic oxidation,” *Applied Surface Science*, vol. 359, pp. 405–411, 2015. URL: https://doi.org/10.1016/j.apsusc.2015.10.124

[99] B. Engelkamp, B. Fischer, and K. Schierbaum, “Plasma Electrolytic Oxidation of Titanium in H2SO4-H3PO4 Mixtures,” *Coatings*, vol. 10, no. 2, 2020. URL: https://doi.org/10.3390/coatings10020116

[100] A. G. Rakoch, V. V. Khokhlov, V. A. Bautin, N. A. Lebedeva, Y. V. Magurova, and I. V. Bardin, “Model concepts on the mechanism of microarc oxidation of metal materials and the control over this process,” *Protection of Metals*, vol. 42, no. 2, pp. 158–169, 2006. URL: https://doi.org/10.1134/S003317320602010X

[101] A. Nominé, S. Troughton, A. Nominé, G. Henrion, and T. W. Clyne, “High speed video evidence for localised discharge cascades during plasma electrolytic oxidation,” *Surface and Coatings Technology*, 2015, This is the final published version. It first appeared at http://www.sciencedirect.com/science/article/pii/S0257897215000778#. URL: https://doi.org/10.1016/j.surfcoat.2015.01.043

[102] S. Troughton, A. Nominé, J. Dean, and T. Clyne, “Effect of individual discharge cascades on the microstructure of plasma electrolytic oxidation coatings,” *Applied Surface Science*, vol. 389, pp. 260–269, 2016. URL: https://doi.org/10.1016/j.apsusc.2016.07.106

[103] D. Netschitailo, “Analyse optischer Aufnahmen bei der plasma-elektrolytischen Oxidation von Titanfolien in Säuren,” Master thesis, 2020.

[104] M. El Achhab, A. Erbe, G. Koschek, R. Hamouich, and K. Schierbaum, “A microstructural study of the structure of plasma electrolytically oxidized titanium foils,” *Applied Physics A*, vol. 116, no. 4, pp. 2039–2044, 2014. URL: https://doi.org/10.1007/s00339-014-8392-5

[105] E. Matykina, G. Doucet, F. Monfort, A. Berkani, P. Skeldon, and G. E. Thompson, “Destruction of coating material during spark anodizing of titanium,” *Electrochimica Acta*, vol. 51, no. 22, pp. 4709–4715, 2006. URL: https://doi.org/10.1016/j.electacta.2006.01.021

[106] J.-P. Gueneau de Mussy, G. Langelaan, J. Decerf, and J.-L. Delplancke, “TEM and X-ray diffraction investigation of the structural characteristics of the microporous oxide film formed on polycrystalline Ti,” *Scripta Materialia*, vol. 48, no. 1, pp. 23–29, 2003. URL: https://doi.org/10.1016/S1359-6462(02)00323-8

[107] C. Sun, R. Hui, W. Qu, S. Yick, C. Sun, and W. Qian, “Effects of processing parameters on microstructures of TiO2 coatings formed on titanium by plasma electrolytic oxidation,” *Journal of Materials Science*, vol. 45, no. 22, pp. 6235–6241, 2010. URL: https://doi.org/10.1007/s10853-010-4718-7

[108] B. Engelkamp, M. El Achhab, B. Fischer, l. Kökçam-Demir, and K. Schierbaum, “Combined Galvanostatic and Potentiostatic Plasma Electrolytic Oxidation of Titanium in Different Concentrations of H2SO4,” *Metals*, vol. 8, no. 6, 2018. URL: https://doi.org/10.3390/met8060386

[109] G. Mortazavi, J. Jiang, and E. I. Meletis, “Investigation of the plasma electrolytic oxidation mechanism of titanium,” *Applied Surface Science*, vol. 488, pp. 370–382, 2019. URL: https://doi.org/10.1016/j.apsusc.2019.05.250

[110] D. Quintero, O. Galvis, J. Calderón, J. Castaño, and F. Echeverría, “Effect of electrochemical parameters on the formation of anodic films on commercially pure titanium by plasma electrolytic oxidation,” *Surface and Coatings Technology*, vol. 258, pp. 1223 – 1231, 2014. URL: https://doi.org/10.1016/j.surfcoat.2014.06.058

[111] S. A. Fadl-Allah, R. M. El-Sherief, and W. A. Badawy, “Electrochemical formation and characterization of porous titania (TiO2) films on Ti,” *Journal of Applied Electrochemistry*, vol. 38, no. 10, p. 1459, 2008. URL: https://doi.org/10.1007/s10800-008-9590-7

[112] T. Shibata and Y.-C. Zhu, “The effect of film formation conditions on the structure and composition of anodic oxide films on titanium,” *Corrosion Science*, vol. 37, no. 2, pp. 253–270, 1995. URL: https://doi.org/10.1016/0010-938X(94)00133-Q

[113] A. Friedemann, T. Gesing, and P. Plagemann, “Electrochemical rutile and anatase formation on {PEO} surfaces,” *Surface and Coatings Technology*, vol. 315, pp. 139 – 149, 2017. URL: https://doi.org/10.1016/j.surfcoat.2017.01.042

[114] G. C. Wood and C. Pearson, “Dielectric breakdown of anodic oxide films on valve metals,” *Corros. Sci*, vol. 7, no. 2, pp. 119–125, 1967. URL: https://doi.org/10.1016/S0010-938X(67)80109-4

[115] F. Simchen, M. Sieber, and T. Lampke, “Electrolyte influence on ignition of plasma electrolytic oxidation processes on light metals,” *Surface and Coatings Technology*, vol. 315, pp. 205 – 213, 2017. URL: https://doi.org/10.1016/j.surfcoat.2017.02.041

[116] Y.-T. Sul, C. B. Johansson, Y. Jeong, and T. Albrektsson, “The electrochemical oxide growth behaviour on titanium in acid and alkaline electrolytes,” *Medical Engineering & Physics*, vol. 23, no. 5, pp. 329 – 346, 2001. URL: https://doi.org/10.1016/S1350-4533(01)00050-9

[117] R. O. Hussein, X. Nie, D. O. Northwood, A. Yerokhin, and A. Matthews, "Spectroscopic study of electrolytic plasma and discharging behaviour during the plasma electrolytic oxidation (PEO) process," *Journal of Physics D: Applied Physics*, vol. 43, no. 10, p. 105203, 2010. URL: https://doi.org/10.1088/0022-3727/43/10/105203

[118] V. Dehnavi, B. L. Luan, X. Y. Liu, D. W. Shoesmith, and S. Rohani, "Correlation between plasma electrolytic oxidation treatment stages and coating microstructure on aluminum under unipolar pulsed DC mode," *Surface and Coatings Technology*, vol. 269, pp. 91–99, 2015. URL: https://doi.org/10.1016/j.surfcoat.2014.11.007

[119] G. Barati Darband, M. Aliofkhazraei, P. Hamghalam, and N. Valizade, "Plasma electrolytic oxidation of magnesium and its alloys: Mechanism, properties and applications," *Journal of Magnesium and Alloys*, vol. 5, no. 1, pp. 74–132, 2017. URL: https://doi.org/10.1016/j.jma.2017.02.004

[120] E. Matykina, A. Berkani, P. Skeldon, and G. Thompson, "Real-time imaging of coating growth during plasma electrolytic oxidation of titanium," *Electrochimica Acta*, vol. 53, no. 4, pp. 1987 – 1994, 2007. URL: https://doi.org/10.1016/j.electacta.2007.08.074

[121] A. L. Yerokhin, L. O. Snizhko, N. L. Gurevina, A. Leyland, A. Pilkington, and A. Matthews, "Discharge characterization in plasma electrolytic oxidation of aluminium," *Journal of Physics D: Applied Physics*, vol. 36, no. 17, pp. 2110–2120, 2003. URL: http://dx.doi.org/10.1088/0022-3727/36/17/314

[122] S. Stojadinović, R. Vasilić, M. Petković, B. Kasalica, I. Belča, A. Žekić, and L. Zeković, "Characterization of the plasma electrolytic oxidation of titanium in sodium metasilicate," *Applied Surface Science*, vol. 265, pp. 226–233, 2013. URL: https://doi.org/10.1016/j.apsusc.2012.10.183

[123] A. Melhem, G. Henrion, T. Czerwiec, J. L. Briançon, T. Duchanoy, F. Brochard, and T. Belmonte, "Changes induced by process parameters in oxide layers grown by the PEO process on Al alloys," *Surface and Coatings Technology*, vol. 205, pp. S133–S136, 2011. URL: https://doi.org/10.1016/j.surfcoat.2011.01.046

[124] J. Martin, A. Melhem, I. Shchedrina, T. Duchanoy, A. Nominé, G. Henrion, T. Czerwiec, and T. Belmonte, "Effects of electrical parameters on plasma electrolytic oxidation of aluminium," *Surface and Coatings Technology*, vol. 221, pp. 70–76, 2013. URL: https://doi.org/10.1016/j.surfcoat.2013.01.029

[125] D.-D. Wang, X.-T. Liu, Y. Su, Y.-K. Wu, Z. Yang, H.-P. Han, X.-Z. Zhang, G.-R. Wu, and D.-J. Shen, "Influences of edge effect on microstructure and corrosion behaviour of PEO coating," *null*, vol. 36, no. 2, pp. 184–191, 2020. URL: https://doi.org/10.1080/02670844.2019.1644935

[126] C. Dunleavy, I. Golosnoy, J. Curran, and T. Clyne, "Characterisation of discharge events during plasma electrolytic oxidation," *Surface and*

Coatings Technology, vol. 203, no. 22, pp. 3410 – 3419, 2009. URL: https://doi.org/10.1016/j.surfcoat.2009.05.004

[127] E. Wahlström, E. K. Vestergaard, R. Schaub, A. Rønnau, M. Vestergaard, E. Lægsgaard, I. Stensgaard, and F. Besenbacher, "Electron Transfer-Induced Dynamics of Oxygen Molecules on the TiO<sub>2</sub>(110) Surface," *Science*, vol. 303, no. 5657, p. 511, 2004. URL: https://doi.org/10.1126/science.1093425

[128] H. Lüth, *Solid Surfaces, Interfaces and Thin Films*, 6th ed., R. Needs, W. Rhodes, S. Scott, E. Stanley, and M. Stutzmann, Eds. Springer International Publishing, 2015, ISBN 978-3-319-10756-1. URL: https://doi.org/10.1007/978-3-319-10756-1

[129] A. Gurlo, "Interplay between O2 and SnO2: Oxygen Ionosorption and Spectroscopic Evidence for Adsorbed Oxygen," *ChemPhysChem*, vol. 7, no. 10, pp. 2041–2052, 2006. URL: https://doi.org/10.1002/cphc.200600292

[130] A. Gurlo, "Insights into the Mechanism of Gas Sensor Operation," in *Metal Oxide Nanomaterials for Chemical Sensors*, M. A. Carpenter, S. Mathur, and A. Kolmakov, Eds. New York, USA: Springer New York, 2013, pp. 3–34, ISBN 978-1-4614-5395-6. URL: https://doi.org/10.1007/978-1-4614-5395-6_1

[131] T. Sahm, A. Gurlo, N. Bârsan, and U. Weimar, "Basics of oxygen and SnO2 interaction; work function change and conductivity measurements," *Sensors and Actuators B: Chemical*, vol. 118, no. 1, pp. 78–83, 2006. URL: https://doi.org/10.1016/j.snb.2006.04.004

[132] M. K. Nowotny, L. R. Sheppard, T. Bak, and J. Nowotny, "Defect Chemistry of Titanium Dioxide. Application of Defect Engineering in Processing of TiO2-Based Photocatalysts," *J. Phys. Chem. C*, vol. 112, no. 14, pp. 5275–5300, 2008. URL: https://doi.org/10.1021/jp077275m

[133] J. Bardeen, "Surface States and Rectification at a Metal Semi-Conductor Contact," *Phys. Rev.*, vol. 71, pp. 717–727, 1947. URL: https://doi.org/10.1103/PhysRev.71.717

[134] H. Ibach and H. Lüth, *Solid-State Physics - An Introduction to Principles of Materials Science*, 3rd ed. Springer-Verlag Berlin Heidelberg GmbH, 2003, ISBN 978-3-540-43870.

[135] W. Göpel, G. Rocker, and R. Feierabend, "Intrinsic defects of TiO_2(110): Interaction with chemisorbed O_2, H_2, CO, and CO_2," *PRB*, vol. 28, no. 6, pp. 3427–3438, 1983. URL: https://doi.org/10.1103/PhysRevB.28.3427

[136] J. J. Yang, M. D. Pickett, X. Li, D. A. A. Ohlberg, D. R. Stewart, and R. S. Williams, "Memristive switching mechanism for metal/oxide/metal nanodevices," *Nature Nanotechnology*, vol. 3, no. 7, pp. 429–433, 2008. URL: https://doi.org/10.1038/nnano.2008.160

[137] M. Strungaru, M. Cerchez, S. Herbertz, T. Heinzel, M. E. Achhab, and K. Schierbaum, “Interdependence of electroforming and hydrogen incorporation in nanoporous titanium dioxide,” *Applied Physics Letters*, vol. 106, no. 14, p. 143109, 2015. URL: https://doi.org/10.1063/1.4917034

[138] R. Su, R. Bechstein, L. Sø, R. T. Vang, M. Sillassen, B. Esbjörnsson, A. Palmqvist, and F. Besenbacher, “How the Anatase-to-Rutile Ratio Influences the Photoreactivity of TiO2,” *J. Phys. Chem. C*, vol. 115, no. 49, pp. 24 287–24 292, 2011. URL: https://doi.org/10.1021/jp2086768

Danksagung

An dieser Stelle möchte ich mich bei all denen bedanken, die mich auf dem langen Weg zur Promotion unterstützt haben.

In der Zeit meines Promotionsstudiums am Institut für Experimentelle Physik der kondensierten Materie war das vor allem mein Doktorvater Prof. Dr. Klaus Schierbaum. Ich danke Ihnen für die freundliche und unkomplizierte Aufnahme in die Arbeitsgruppe. Danke für die konstruktiven Gespräche und die stetige Unterstützung meiner Arbeit. Daneben möchte ich auch Mhamed El Achhab danken für die Einarbeitung und die fachlichen Diskussionen zum Thema PEO. Eine große Hilfe war mein Weggefährte Wolfram Gilbert. Ich danke dir für die gute Zusammenarbeit und den gegenseitigen Austausch. Auch Christiane Braun möchte ich besonderen Dank aussprechen für die schnelle Hilfe in jeglichen administrativen Angelegenheiten. Vielen Dank an Jörg van Ommen für die technische Unterstützung und Denis Netschitailo für die gemeinsame Arbeit an den optischen Untersuchungen.

Mein besonderer Dank gilt Prof. Dr. Mathias Getzlaff für die Rolle als Mentor während meines Promotionsstudiums und die bereitwillige Übernahme des Korreferats.

Ich danke auch Björn Fischer für die Raman-Spektroskopie und seiner freundlichen Beratung bei den optischen Untersuchungen. Mein Dank geht auch an Steffen Köhler vom CAI der Universität Düsseldorf, an Egbert Wessels vom Forschungszentrum Jülich für die hervorragenden SEM-Aufnahmen in der ersten Publikation [108], an Ülkü Kökçam Demir für die angenehme Betreuung bei den XRD-Messungen in der Arbeitsgruppe von Prof. Dr. Christoph Janiak, an das Team des ICAN der Universität Duisburg-Essen und an Andreas Schreiber (Microtrac Retsch GmbH, ehemals Porotec GmbH) für die Adsorptionsmessungen.

Ganz besonderen Dank gilt den Personen in meinem privaten Umfeld. Dazu zählen all meine tollen Freunde. Aber vor allem danke ich meinen Eltern, Anna und Franz, für den Rückhalt und die bedingungslose Unterstützung in jeglichen Situationen und meinen beiden Geschwistern, Miriam und Hendrik, für die ermutigenden Gespräche. Nicht zuletzt gebührt ein ganz spezieller Dank meiner Freundin, Kathrin Joppe. Vielen Dank für deine unermüdliche Geduld, Liebe und Zuspruch während meiner Promotionszeit.

Eidesstattliche Versicherung

Ich versichere an Eides Statt, dass die Dissertation von mir selbstständig und ohne unzulässige fremde Hilfe unter Beachtung der „Grundsätze zur Sicherung guter wissenschaftlicher Praxis an der Heinrich-Heine-Universität Düsseldorf“ erstellt worden ist.

Düsseldorf, den 08. Juni 2021

....
(Bernd Engelkamp)